NON-INERTIAL UNDULATORY LOCOMOTION ACROSS SCALES

A Dissertation
Presented to
The Academic Faculty

By

Kelimar Diaz Cruz

In Partial Fulfillment
of the Requirements for the Degree
Doctor of Philosophy in the
School of Physics
Quantitative Biosciences Ph.D. Program

Georgia Institute of Technology

December 2022

NON-INERTIAL UNDULATORY LOCOMOTION ACROSS SCALES

Thesis committee:

Dr. Daniel I. Goldman, Advisor
School of Physics
Georgia Institute of Technology

Dr. Hang Lu
School of Chemical and Biomolecular Engineering
Georgia Institute of Technology

Dr. Joseph R. Mendelson III
School of Biological Sciences
Georgia Institute of Technology

Dr. David Hu
School of Mechanical Engineering
Georgia Institute of Technology

Dr. Simon Sponberg
School of Physics
Georgia Institute of Technology

Date approved: November 30, 2022

For Gabriela, Kirianys, Kairi, Orlando Emmanuel,

and the soon-to-be new member of the family.

ACKNOWLEDGMENTS

Before presenting the work I have done over the last years, I would like to thank everyone who has contributed to my development as a scientist and my over all growth as an individual.

First, I would like to thank my family. I am truly grateful for my husband, Fabian E. Cintron Mojica, for always pushing me forward with a smile on his face, believing in me when I could not do that myself. My parents, Orlando Diaz Correa and Jackeline Cruz Baez, while for the most part they had no idea what I was doing, they never ceased to show their much needed love and support. My sister, Kelinet Diaz Cruz, from our silly conversations to her intensive care of our family when I was not able to, truly, I could not have asked for a better sister. My brother, Orlando Diaz Cruz, his million nicknames and checkups brightened even the simplest of days. My nieces, Kirianys and Kairi Diaz Diaz, they might not know it now but their auntie treasures all their love and innocence.

I would also like to thank the many people that my second family, my friends from many years, for their love and support: Yenuel Jones Alberty, Katheryn L. Malave Rodriguez, Jose J. Maldonado Mendez, Yaneris Y. Agosto Rodriguez, Diego Orro, Andrea Maldonado, Janelis Gonzalez Santiago, Natasha Gonzalez Santiago, Shakira Gonzalez Santiago.

My deepest gratitude go toward past and current members of the CRAB lab: Jennifer Rieser, Yasemin Ozkan-Aydin, Henry Astley, Enes Aydin, Perrin E. Schiebel, Christopher Pierce, Ram Avinery, Deniz Kerimoglu, Hosain Bagheri, Andras Karsai, Shengkai Li, Will Savoie, Christian Hubicki, Akash Vardhan, Baxi Chong, Steven W. Tarr, Tianyu Wang, Aradhya Rajanala, Madison Hales, Juntao He, Kehinde Aina, Margot Paez, Alexandra Carruthers-Ferrero, Jonathan Gosyne, Bahnisikha Dutta, Daniel Soto, Jeffrey Shen, Hussain Gynai, Ian Tomkinson, Alex Hubbard, Tommie L. Robinson, Eva Erickson, Amber Young, Marine Maissoneuve, Richard Newsome, Andrea Manning, Joseph Brunner, Noah Egan, Venny Kojouharov, Joonha Hwang, Karson Lewis, Esteban Flores, Adbul Kabba,

Grace Cassidy, Erin McCaskey, and Mason Murray-Cooper. I would like to give special thanks to Akash Vardhan and Margot Paez in particular, we make an odd trio but certainly a fun one. I would also like to give special thanks to Perrin Schiebel and Jennifer Rieser for serving a great mentors and helping me build a foundation to truly be an experimentalist. Special thanks to all of the undergraduates, Tommie L. Robinson, Eva Erickson, Amber Young, Richard Newsome, Andrea Manning, and Marine Maissoneuve, who helped me discover and hone my love for teaching and mentoring. I would like to thank Christopher Pierce who has not only provided research and career guidance but has also been incredibly supportive. Last but not least, I would like to thank each and every lab member who has been a research collaborator and/or contributor, without you this thesis would have not been possible: Yasemin Ozkan-Aydin, Enes Aydin, Christopher Pierce, Baxi Chong, Steven W. Tarr, Tommie L. Robinson, Eva Erickson, and Daniel Soto.

There are many professors and academic staff, that have helped me in one way or another that I would like to thank. Prof. Kirsty Y. Wan for the collaborative work done over the years that introduced me to the world of microswimmers. Prof. Joseph Mendelson III for his guidance, support, and opportunity to experience field work. Shaun Ashley for always rooting for me. Renee Simpkins and Gary Longstreet for their candid greetings and light conversations. Lisa Redding for her amazing support in many areas throughout the years, truly the QBioS program is lucky to have her.

Lastly, I would like to thank my advisor, Prof. Daniel I. Goldman. In the summer of 2016, the last thing I expected was to be recruited at the end of the REU program. Back then, I did not even imagine someone would want me to be a part of their research group. Truly, that was pivotal moment in my life, and I will never forget the kindness and heartfelt welcome. My sincerest gratitude for all the guidance and support throughout the years, for helping me grow as a scientist, communicator, mentor, and as a person.

TABLE OF CONTENTS

LIST OF FIGURES

SCIENTIFIC NAMES OF ORGANISMS

Agama agama *Ag. agama*

Brachymeles kadwa *B. kadwa*

Caenorhabditis elegans *Cae. elegans*

Carteria crucifera *Car. crucifera*

Chionactis occipitalis *Ch. occipitalis*

Crotalus cerastes *Cr. cerastes*

Euphausia superba *E. superba*

Gecko gecko *Ge. gecko*

Gymnothorax ocellatus *Gy. ocellatus*

Lepomis machrochirus *Le. machrochirus*

Lithobious forficatus *Li. forficatus*

Narcesus americanus *Na. americanus*

Nereis virens *Ne. virens*

Ochromonas malhamensis *Oc. malhamensis*

Odontodactylus scyllarus *Od. scyllarus*

Pyramimonas gelidicola *P. gelidicola*

Pyramimonas parkae *P. parkae*

Pyramimonas tetrahyncus *P. tetrahyncus*

Scolopendra polymorpha *Scd. polymorpha*

Scolopocryptops sexspinosus *Scc. sexspinosus*

Stenella coeruleoalba *St. coeruleoalba*

Synechococcaceae major *Sy. major*

Uma scoparia *U. scoparia*

SUMMARY

Locomotion is crucial to behaviors such as predator avoidance, foraging, and mating. In particular, undulatory locomotion is one of the most common forms of locomotion. From microscopic flagellates to swimming fish and slithering snakes, this form of locomotion is a remarkably robust self-propulsion strategy that allows a diversity of organisms to navigate myriad environments. While often thought of as exclusive to limbless organisms, a variety of locomotors possessing few to many appendages rely on waves of undulation for locomotion. In inertial regimes, organisms can leverage the forces generated by their body and the surrounding medium's inertia to enhance their locomotion (e.g., coast or glide). On the other hand, in non-inertial regimes self-propulsion is dominated by damping (viscous or frictional), and thus the ability for organisms to generate motion is dependent on the sequence of internal shape changes. In this thesis, we study a variety of undulating systems that locomote in highly damped regimes. We perform studies on systems ranging from zero to many appendages. Specifically, we focus on four distinct undulatory systems: 1) *Cae. elegans*, 2) quadriflagellate algae (bearing four flagella), 3) centipedes on terrestrial environments, and 4) centipedes on fluid environments. For each of these systems, we study how the coordination of their many degrees of freedom leads to specific locomotive behaviors. Further, we propose hypotheses for the observed behaviors in the context of each of these system's ecology.

Starting with limbless systems, we study how the nematode worm *Cae. elegans* generates and controls for turning behaviors in laboratory environments. Specifically, we use dimensionality reduction techniques and a geometric framework to rationalize the observed body dynamics. Our work suggests a neuromechanical control strategy for turning behaviors.

We adopt a robophysical modeling approach to study quadriflagellate propulsion in low Reynolds number fluids. We develop the first macroscopic autonomous self-propelling

robot and implemented gaits observed in biological quadriflagellate algae. Our results show that swimming performance is sensitive to swimming gait, and propose a hypothesis for single gaits in distinct algae species.

We study how two distinct centipede species, *Scd. polymorpha* and *Scc. sexspinosus*, coordinate their limbs and body to navigate laboratory rugose terrains. We demonstrate that both centipede species use presumed passive mechanics to negotiate limb-substrate collisions and traverse the terrains. We observe a change in the limb-dynamics in one of the centipede species, while not improving locomotor performance, that we posit reduces the uncertainty of finding secure footfalls.

Lastly, we study the swimming dynamics of *Li. forficatus*, a surface swimming centipede. We find that the environmental generalist centipede swims via continuous body-fluid contact and uses direct waves of body undulation for propulsion. We show that forward propulsion is achieved by modulation of the forces experienced in each segments, facilitated by the centipede morphology. Our work suggests that the centipede's swimming strategy reduces the neuromechanical complexity associated with a change in gait.

CHAPTER 1
INTRODUCTION AND BACKGROUND

1.1 Overview of thesis

Movement is essential for many organisms [1]. A diversity of organisms rely on locomotion for fundamental behaviors such as reproduction, migration, resource acquisition, among others. Particularly, undulatory locomotion is a common locomotive behavior in the natural world [2]. This form of locomotion is present in organisms of varying sizes and morphology that inhabit myriad environments, indicative of its robustness [2].

At the microscopic scale, cells such as spermatozoa undulate their flagella during propulsion [3]. Flagellated algae possessing from two to sixteen flagella undulate their appendages in a whip-like motion, coordinating them to generate rhythmic pattern [4]. The mm-scale nematode worm, *Caenorhabditis elegans*, relies on dorso-ventral undulation to locomote a variety of environments [5, 6, 7, 8, 9, 10]. These are a few examples of the rich diversity of microorganisms that use undulatory waves for locomotion.

Similarly, there are both aquatic and terrestrial macroscopic organisms that rely on undulatory locomotion. Eels and lamprey are common examples of undulators [11, 12], with waves reminiscent of those observed in snakes. Fish, dolphins, and whales swim via waves in concert with fin coordination [13, 14]. Snakes can exhibit various gaits, lateral undulation being the most common. Multi legged systems, such as lizards, can aid leg protraction/retraction with the use of body undulation, where the emergence of traveling body waves is coupled to locomotor speed [15, 16, 17, 18, 19]. Similarly, some centipede species exhibit body undulation that complements leg protraction/retraction when running at high speeds [20, 21].

many-legged systems (with five or more leg pairs) exhibit waves of limb flexion known

as metachronal waves. Limbs aggregate and are propagated sequentially toward and front or rear of the locomotor, depending on the organism. Metachronal waves are present in both fluid and terrestrial locomotors, such as krill [22], shrimp [23], millipedes [24, 25], and centipedes [20].

Progress has been made in understanding undulatory propulsion in both fluid [26, 28, 29, 11, 30, 12, 31, 32, 33, 27] and terrestrial environments [34, 35, 36, 37, 38, 39, 40, 15]. Broadly, these can be further classified depending on the locomotor regime, whether inertial or non-inertial. Organisms that locomote in inertial regimes leverage both the body/appendage and the surrounding media's inertia for propulsion. In contrast, organisms that locomote in non-inertial regimes rely on patterns of self-deformation to generate motion due to the highly damped nature of their surroundings.

Given the diversity of organisms and environments, this thesis seeks to further our understanding of undulators in non-inertial regimes. Specifically, we study locomotion ranging from limbless to many limbed organisms. This thesis focuses on locomotors and corresponding behaviors that are less studied, relative to previous studies within the field (e.g., rugose terrain traversal of centipedes). We aim to understand how a locomotor's pattern of self-deformation interacts with its surroundings to exhibit a desired behavior. Further, we seek to understand observed locomotor behaviors given an organism's natural habitat. This work provides insights that can aid the development of deployable robot models for locomotion in a variety of environments.

1.2 Propulsion via waves of undulation

Undulatory locomotion is ubiquitous; the ability to generate and propagate waves of curvature along some or all parts of the body is present in a diversity of organisms and scales [2] (Figure 1.1). Microscopic cells (e.g., spermatozoa [41, 42]) and flagellates (e.g., algae [26]) use their flagella for propulsion (Figure 1.1A-B). Waves of undulation in the flagella are propagated from the point of attachment to the end of the appendage (away from the body).

Certain flagellates (e.g., algae with two or more flagella [26, 4, 43, 44]), coordinate their appendages in rhythmic patterns (which we will denote as gaits) reminiscent of those observed in macroscopic systems, as we will show in Chapter 3. These are abundant in marine, terrestrial, and freshwater habitats [43]. On the other hand, unflagellated microorganisms (e.g., cyanobacteria [45]) resort to self-deformation of their body to propagate low-amplitude body waves (Figure 1.1C). At the mm-scale, the nematode worm *Cae. elegans* relies on the generation and propagation of dorsoventral waves to locomote [5] (Figure 1.1D). This worm encounters a wide range of environments in the wild, such as rotting fruit, damp soil, and the bodies of molluscs (e.g., slugs) [6]. In laboratory environments, *Cae. elegans* is capable of locomoting on fluids with viscosities spanning several orders of magnitude [7], non-Newtonian fluid [5], agar gel surfaces [8], and rigid-post arrays [9, 10]. In addition, as we will discuss in Chapter 2, this worm uses these body waves to generate turning maneuvers that potentially facilitate locomotion in a wide range of environments.

Larger scale organisms in fluids are commonly studied undulators. Distinct species of fish [29] laterally undulate their bodies to navigate waters of varying flow. Elongated animals, such as eels and lamprey [11, 12, 29], use anguilliform swimming that relies on head-to-tail lateral body bending, with posteriorly increasing amplitude (Figure 1.1E). Eels, in particular, can also burrow [48] and locomote on terrestrial substrates [49]. Large marine mammals (e.g., dolphins [50] and whales) undulate their bodies dorsoventrally to produce forward motion (Figure 1.1F).

Locomotion via waves of undulation is not limited to organisms primarily in fluids. A diversity of animals locomote via waves of undulation in terrestrial environments. Snakes, for examples, use a variety of gaits for propulsion, such as sidewinding and lateral undulation (Figure 1.3A-B). Sidewinders (i.e., *Crotalus cerastes*) propagate body waves in both the lateral and dorsoventral dimension to lift segments of the body and generate discrete substrate-body contact [51]. On the other hand, lateral undulation is the most common gait used by terrestrial snakes. This form of undulation consists of posteriorly propagated

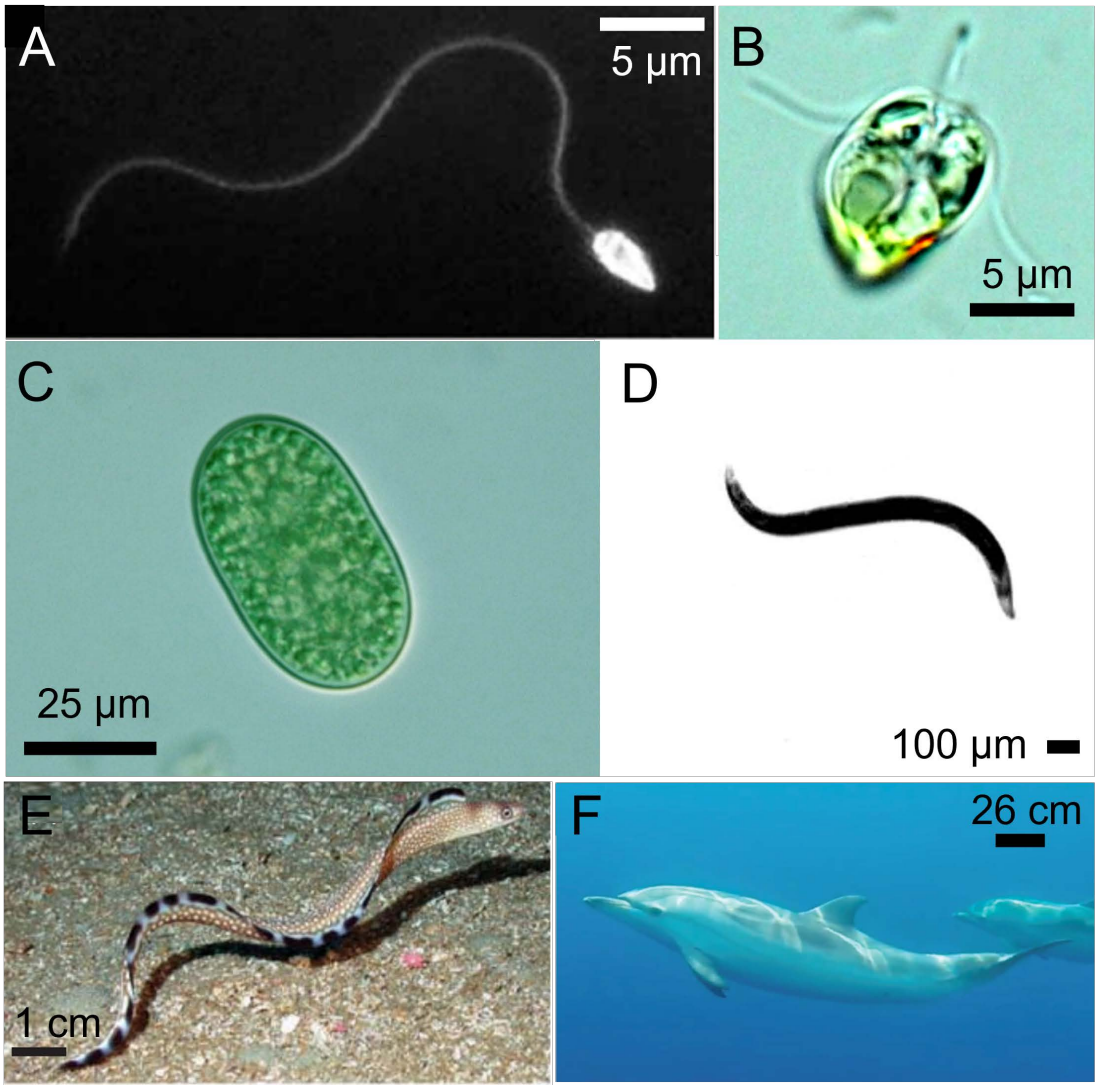

Figure 1.1: **Undulatory locomotion in fluids accross scales.** (A) Sea-urchin spermatozoa. Image adapted from [3]. (B) Quadriflagellate algae (*Car. crucifera*). Image credit: Kirsty Y. Wan. (C) Cyanobacteria (*Sy. major*). Image adapted from [46]. (D) Nematode worm *Cae. elegans*. (E) Ocellated moray (*Gy. ocellatus*). Image adapted from [47]. (F) Mediterranean striped dolphins (*St. coeruleoalba*). Image adapted from [14].

waves. Lateral undulations allows snakes to locomote in confined spaces [34], swim in water [52], locomote on and underneath sand [35, 36, 39], and traverse rigid-post arrays [53, 38]. Notably, this is the only form of undulation that is also present in all limbless reptiles [54].

Legged terrestrial systems can complement the use of their appendages with waves of undulation. Lizards can produce standing or traveling waves of undulation during locomo-

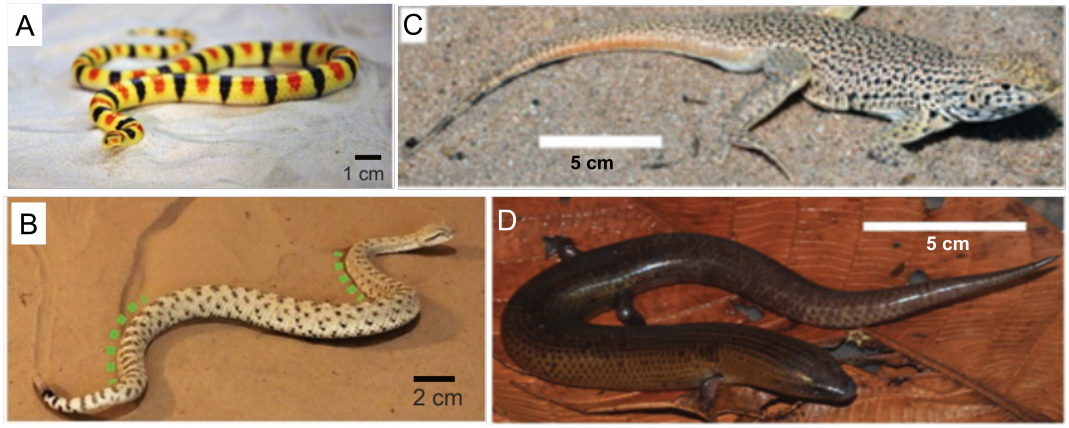

Figure 1.2: **Terrestrial undulators.** Example limbless locomotors: (A) the shovel-nosed snake (*Ch. occipitalis*) and (B) the sidewinder snake (*Cr. cerastes*). Figures adapted from [39]. (C) Example legged locotomors: the mojave fringe-toed lizard (*U. scoparia*) and (D) Jessie's slender skink (*B. kadwa*). Figures adapted from [24].

tion [16, 17, 18, 19, 15]. Whether a lizard uses a standing or traveling wave is dependent on the morphology as well as the speed [16, 18, 19]. Species of lizards with well-developed limbs use standing waves when locomoting at low speeds [16, 18, 19], replaced by traveling waves when locomoting at high speeds [16, 18, 17, 15]. Even many-legged systems such as centipedes can complement leg protraction/retraction with body waves. Certain centipede species exhibit characteristic body undulation, for which the body amplitude increases with increasing speed [20, 21].

Unlike animals with few limbs (two to four leg pairs), animals with many limbs can exhibit waves of limb-flexion, known as metachronal gaits/waves or metachrony in fluids and limb-stepping waves/patterns in terrestrial environments. During metachrony, each limb performs a sequential pattern that is repeated after a fixed phase lag between adjacent limbs [23, 55]. The frequency and wavelength of this wave is dictated not only by the phase lag but also by the relative spacing between adjacent limbs [23]. In fluids, metachrony has been found to produce steady and efficient flows [56], augment swimming speed [57, 58], and increase fluid transport (in cilia) [59, 60, 61], relative to fully synchronous appendages [23]. Although metachrony is present in myriapods (millipedes and centipedes), there are limited studies on myriapod locomotion in general. In millipedes, previous stud-

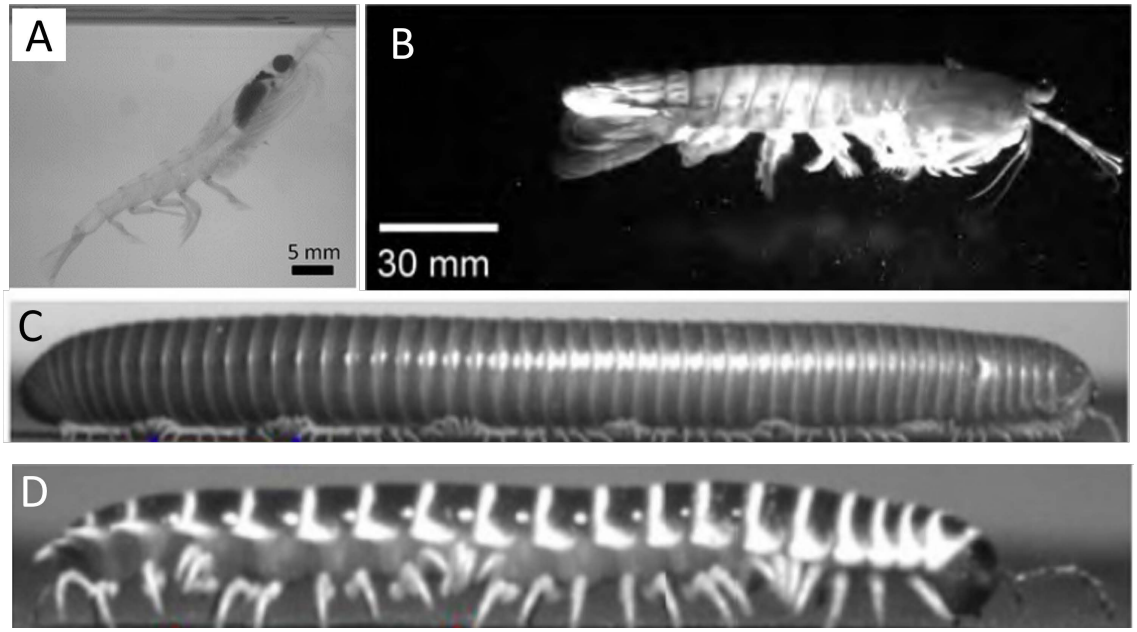

Figure 1.3: **Waves of limb flexion.** Example animals that rely on waves of limb flexion, metachronal waves, for locomotion in fluids: (A) the Antartic krill (*E. superba*) and (B) the peacock mantis shrimp (*Od. scyllarus*). (A) adapted from [22], (B) adapted from [23]. Example animals that rely on waves of limb flexion, metachronal waves, for locomotion in terrestrial environments: (A) the American giant millipede (*Na. americanus*) and (D) the Kentucky flat millipede (*Ap. virginiensis*). Figures adapted from [15].

ies have found that the metachronal wave is modulated to control the thrust force generated during burrowing, climbing, or walking [25, 24]. In centipedes, metachrony (i.e., the propagation direction of the wave) has been characterized as species specific [20, 62, 63], further discussed in Chapter 4 and 5.

1.3 Classification of traveling waves

Across the diversity of organisms and range of spatial and temporal scales, traveling waves can be characterized by the direction and plane of propagation.(Figure 1.4). Broadly, these can be classified as horizontal or vertical, and direct or retrograde [2]. A wave is classified as horizontal or vertical depending on the plane of propagation relative to the locomotor's body (or appendage, in the case of flagellates). If dorso-ventral waves are propagated, these are referred to as vertical plane waves. Conversely, laterally propagated waves are

referred to as horizontal plane waves. For example, eels, lamprey, and some terrestrial snakes [11, 12, 36, 37] use horizontal body waves (Figure 1.5A). As previously mentioned, sidewinders (i.e., *Cr. cerastes* [51]) rely on a combination of horizontal and vertical waves (Figure 1.5C). In *Cae. elegans*, the animal locomotes on its side. Thus, while the undulation is reminiscent of lateral undulation in snakes and eels, waves generated are vertical, not horizontal.

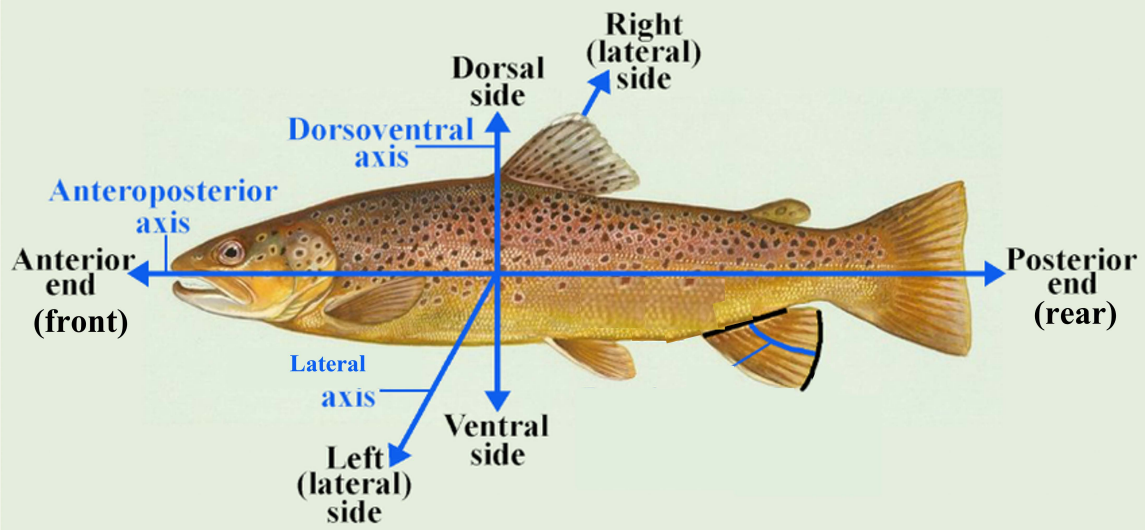

Figure 1.4: **Locomotor axes.** The left and right side of a locomotor correspond to the lateral (horizontal) axis. Dorsal and ventral side of the body makeup the dorso-ventral (vertical). If the locomotor is moving forward (from right to left in the page), waves are direct/retrograde is they are propagated to the anterior/posterior end. Figure adapted from [64].

Whether a wave is direct or retrograde depends on the propagation direction of the wave. While the propagation direction can be defined relative to the locomotor longitudinal (anteroposterior) axis, here we define it relative to the locomotor's direction of motion (Figure 1.4). When an organisms is generating forward propulsion and the body wave is propagated *opposite* to the direction of motion, these are known as retrograde waves. Contrarily, when forward motion is achieved with body waves that are propagated *with* the direction of motion, these are known as direct waves. Commonly studied undulators rely on the use of retrograde waves, to generate thrust away from the body and achieve forward propulsion. However, various swimmers such as polychaete worms (i.e., *Nereis*

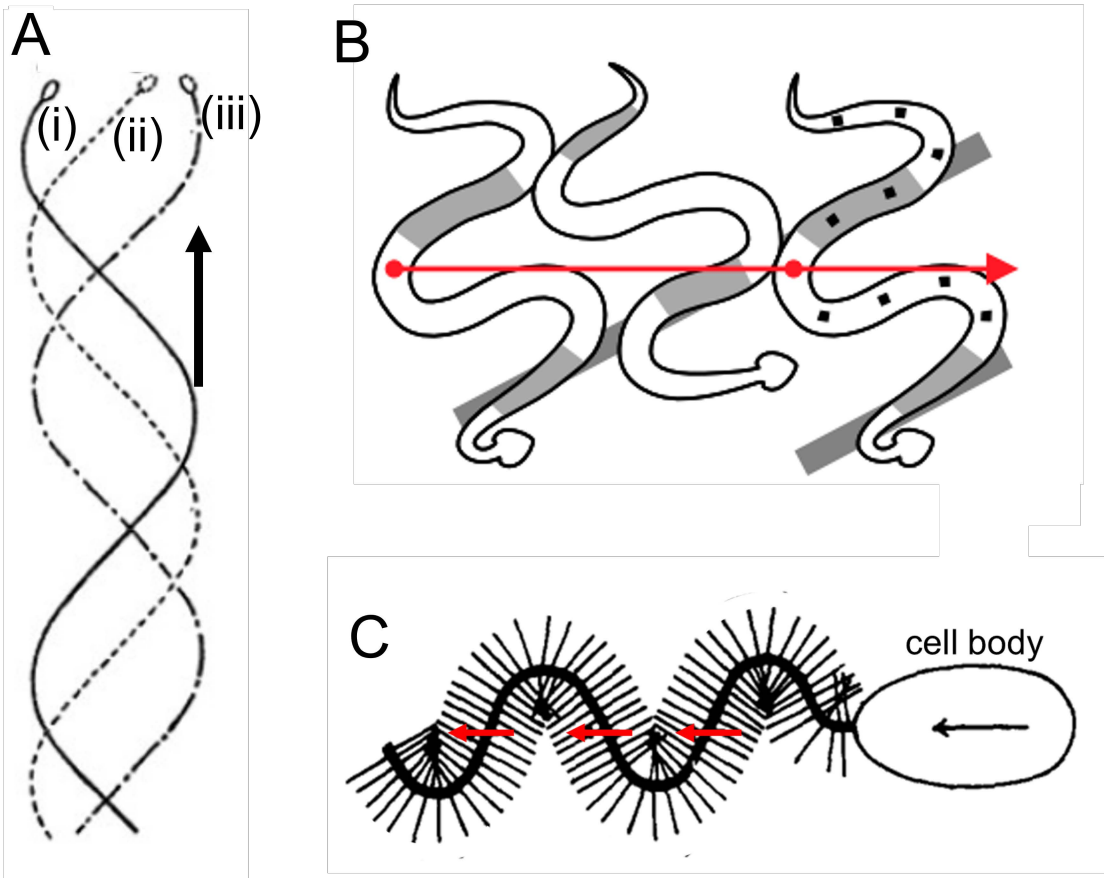

Figure 1.5: **Classification of waves relative to body and direction of motion.** (A) Diagram of horizontal waves (e.g., lateral undulation) in a limbless system. Arrow shows the direction of motion. Time progresses from (i) to (iii). Waves are retrograde, propagated opposite the direction of motion. Figure adapted from [65]. (B) Diagram of a combination of horizontal and vertical waves (i.e., sidewinding). Arrow shows the direction of motion and time profession. Grey shaded regions correspond to body segments that are in contact to substrate. Time progresses from left to right. Figure adapted from [40]. (C) Diagram of motile alga with hispid flagella. Arrows correspond propagation direction of the wave (red) and the direction of motion (black). Figure adapted from [66].

virens [68]) and motile alga (*Ochromonas malhamensis* [66, 69, 70]) achieve forward motion via direct waves (Figure 1.5C). The common principle between these systems is the distinct morphology relative to other undulators; the body (flagellum in *Oc. malhamensis*) has perpendicular oriented appendages ("hisps" in *Oc. malhamensis*). For systems that rely on retrograde waves, drag forces are greater for lateral motion than for forward/backward motion [68, 69, 70]. In the case of polycheate worms and motile alga, the appendages/hisps

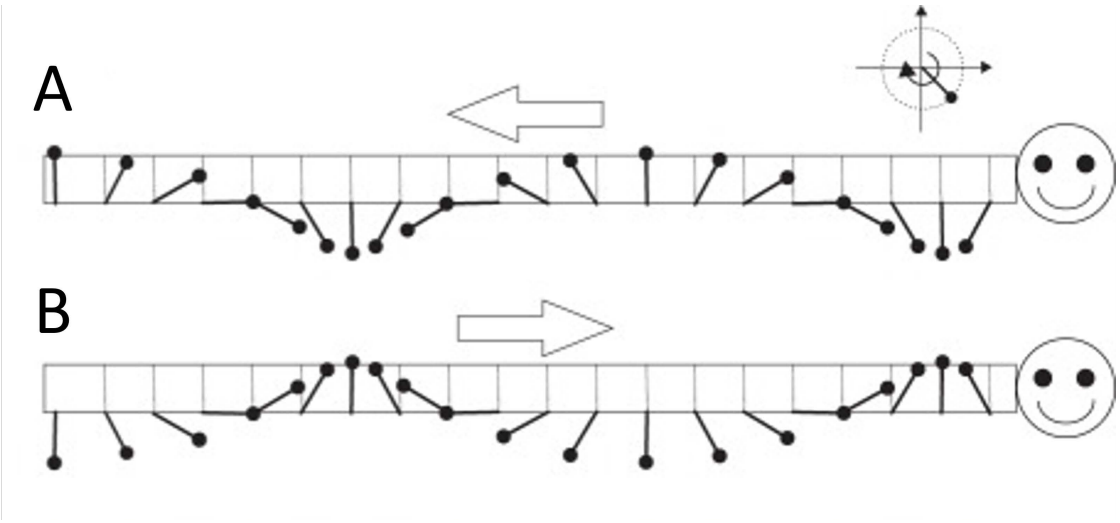

Figure 1.6: **Waves in legged systems.** Diagrams of (A) retrograde and (B) direct leg wave propagation. Locomotor moves from left to right. Arrows denote the direction of propagation of the limbs. Figure adapted from [67].

result in drag forces that are greater for forward/backward motion than for lateral motion. Similar principles can be found in surface swimming centipedes, as we will show in Chapter 5.

As previously mentioned, many-legged systems can exhibit metachronal waves. Similar to body waves, whether a metachronal wave is considered direct or retrograde depends on the direction of propagation relative to the direction of motion of the locomotor. Assuming forward motion, metachronal waves propagated posteriorly (in the caudal direction) are known as retrograde waves, whereas metachronal waves propagated anteriorly (in the rostral direction) are known as direct waves (Figure 1.6). A wave is determined to be either direct or retrograde by using the appendage aggregates as a proxy for propagation direction. The direction of propagation of the wave depends on the locomotor; that is, there are no dominant wave directions across the entire diversity of organisms. In fluids, krill use a retrograde wave, where as polycheates use direct waves. In terrestrial environments, there are five centipede order that have been broadly classified to exhibit either direct (two orders) or retrograde (three orders) limbs waves [20]. On the other hand, millipedes have only been reported to exhibit direct limb waves [25, 24].

1.4 Non-inertial locomotion and Resistive Force Theory

Microscopic swimmers locomote in a low Reynolds number regimes due to their scale. In such a locomotor regime, forces from the surrounding medium resist the motion of the swimmer. That is, the Reynolds number (Re, the ratio of inertial to viscous forces) is small ($Re \ll 1$), $Re = UL/v$, where U is the velocity of the swimmer, L is the length scale, and v is the kinematic viscosity of the fluid. Thus, the ability for these swimmers to generate self-propulsion (or exhibit other behaviors, as in Chapter 2) depends on the shape changes of their body and/or appendages, rather than the acceleration of the fluid or the locomotor. Specifically, resistive forces arise due to fluid viscosity (viscous damping) and inertial forces are negligible [41, 71]. If these organisms stop self-deforming during locomotion, there is no "inertial coasting" and thus come to a stop. In contrast, macroscopic swimmers (e.g., eels, lamprey [11, 12]) that use undulations can leverage the forces generated by the fluid and body inertia.

In this non-inertial regime reciprocal motion does not produce forward motion. Purcell [72] described this as the *Scallop Theorem* (Figure 1.7). In a high Reynolds number regime, a scallop opens and closes its shell at different speeds (opening slowly, closing fast) to eject water away from the shell and produce some net displacement in the opposite direction that the water is ejected. However, if the scallop is in a low Reynolds number regime, irrespective of the timing between opening and closing, viscous damping makes the effects of reactive forces negligible. In other words, reciprocal motion of the scallop will not lead to propulsion due to the equivalent flow in and out of the shell. Thus, for swimmers in highly damped regimes forward propulsion is achieved by a cyclic pattern (i.e., gait) of asymmetric shape deformations [72] for non-reciprocal motion. That is, as discussed by Purcell [72], a swimmer requires at least two degrees of freedom (e.g., three-link swimmer) to break time reversal-symmetry and achieve propulsion in low Reynolds environments. In Chapter 3, we will show these features of low Reynolds number swimming and implement

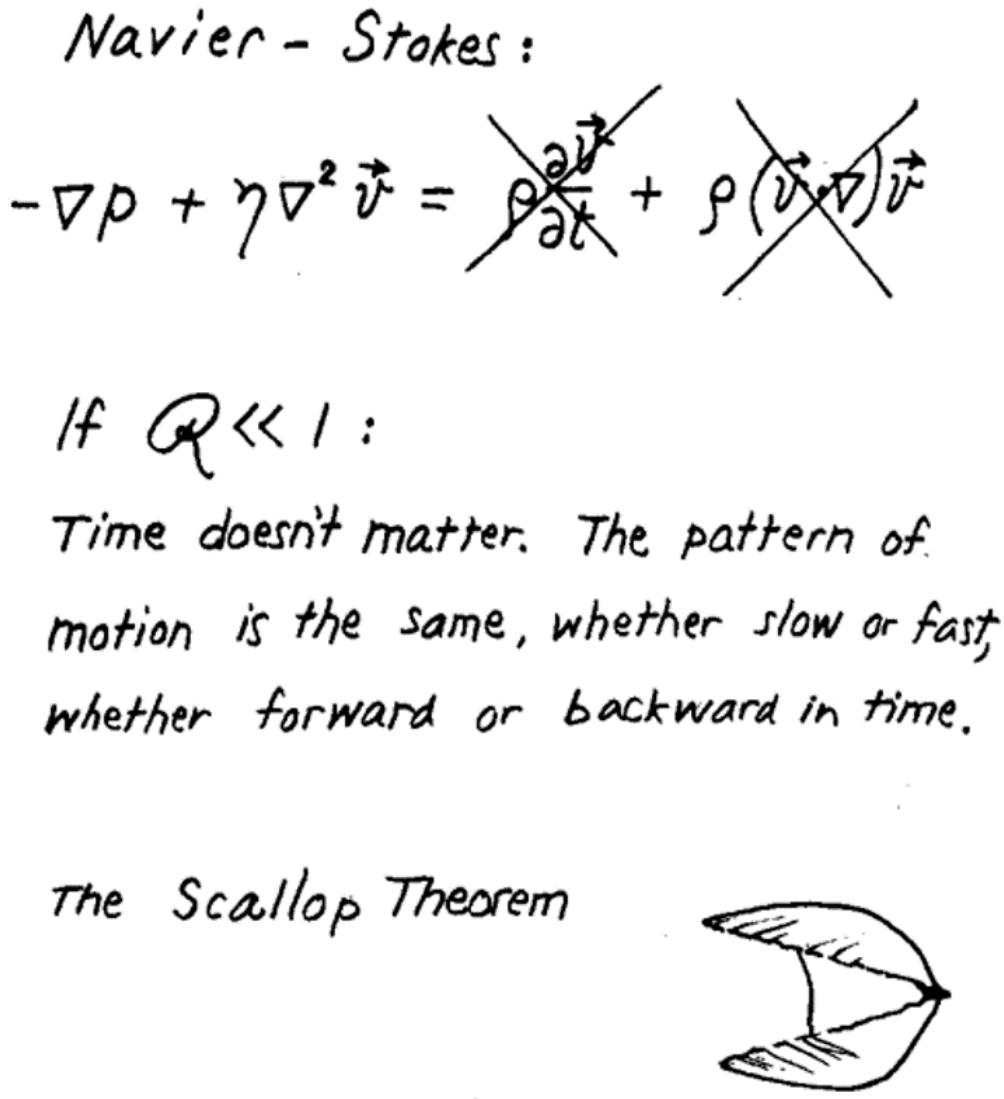

Figure 1.7: **Scallop Theorem.** In high Reynolds number fluids, a scallop can leverage inertia with a single degree of freedom to produce motion. In low Reynolds, inertial terms in the Navier-Stokes equation are negligible and propulsion is not achieved with symmetric gaits (in shape or time). Figure from [72].

reversal symmetry breaking for effective propulsion.

Resistive Force Theory (RFT) was developed to model and predict performance of low Reynolds number swimmers [71]. Instead of solving the full Navier-Stokes equations, RFT provides simpler approximations [73, 47]. That is, RFT assumes that the forces acting on infinitesimal segments of a body are independent (i.e., do not influence forces on other segments), and thus the total force acting on the entirety of the body is the sum of the forces

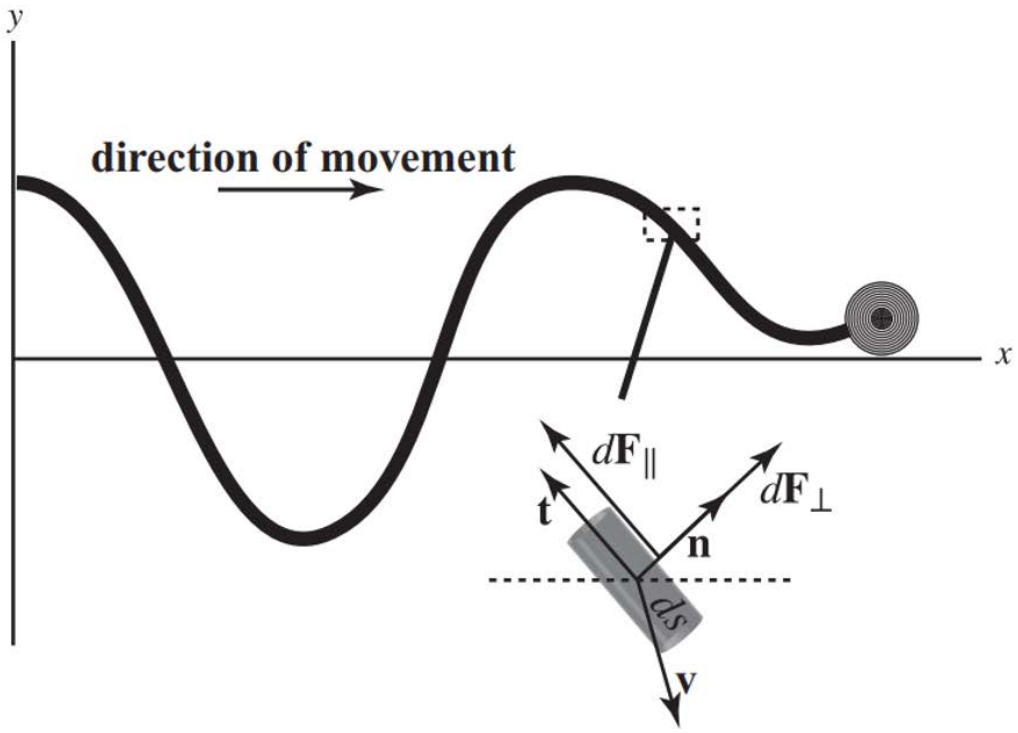

Figure 1.8: **Resitive Force Theory.** Illustration of a two-dimensional swimmer. A wave is propagated down the body (negative x-direction) generating forward propulsion (positive x-direction). The body is partitioned into infinitesimal segments (*ds*), each with a specific orientation (tangent , $\hat{\mathbf{t}}$, and normal, $\hat{\mathbf{n}}$) and velocity ($\mathbf{v}$), experiencing perpendicular ($d\boldsymbol{F}_{\perp}$) and parallel ($d\boldsymbol{F}_{||}$) forces. Figure from [47].

acting on each segment (Figure 1.8). The accuracy and effectiveness of RFT depends on this underlying assumption (decoupled force/flow fields) [74]. We note that for some high Reynolds number swimmers, where inertial effects are not negligible, this assumption does not hold. Flow is generated down the swimmers body and vortex is shed at the rear for thrust generation [12].

RFT has not only proven effective in viscous fluids [71, 75, 76, 77]; it has also been successfully applied to frictional fluids (i.e., granular media [78, 79, 35, 37]) where frictional forces (instead of viscous) dominate inertial forces. Therefore, terrestrial undulators that locomote in frictional damped regimes are also to a good approximation *non-inertial systems.* Similar to low Reynolds number swimmers, self-propulsion depends on the shape

changes of the terrestrial locomotor, and no gliding or coasting phases aid locomotion (due to frictional damping). Unlike in the Navier-Stokes equations for fluids, until recent work [74] there were no constitutive equations for forces acting on infinitesimal segments for frictional fluids. Thus, forces had been measured empirically by dragging a model segment through the media with varying orientation to obtain perpendicular and parallel forces acting on the segment (Figure 1.8). We adopt a RFT approach in Chapter 5, where inertia is dominated by water surface waves requiring us to make the first water-air drag measurements.

Whether in fluid or in terrestrial environments, a rich diversity of organisms locomote in non-inertial regimes [3, 4, 39, 35, 36, 40, 15, 70]. A general question that can be asked for all of these is, what is the appropriate sequence of self-deformation to generate a desired behavior? In doing so, we can study how the locomotor coordinates its degrees of freedom to exhibit the behavior. A combination of biological experiments, robophysical modeling, and theoretical modeling can shed some insight into these unknowns. Further, while laboratory models are relatively simple, systematic studies can broaden our understanding of how a particular behavior is desirable in the context of the locomotor's natural surroundings. Moreover, insights into the control principles of these organisms can aid the development of deployable robot models that exhibit comparable capabilities to perform tasks in a variety of scales and environments, such as targeted drug delivery (at the microscopic scale) and search-and-rescue (at the macroscopic scale).

1.5 Robophysical modeling

Organisms maneuver and navigate across challenging environments. Inspired by the diversity of behaviors in biological systems, roboticists, engineers, and increasingly physicists have developed robots with animal-like capabilities. These have been achieved by studying the interplay between an locomotor's morphology, physiology, control strategy, and the environment. For example, previous work has shown that gecko (*Gekko gecko*)

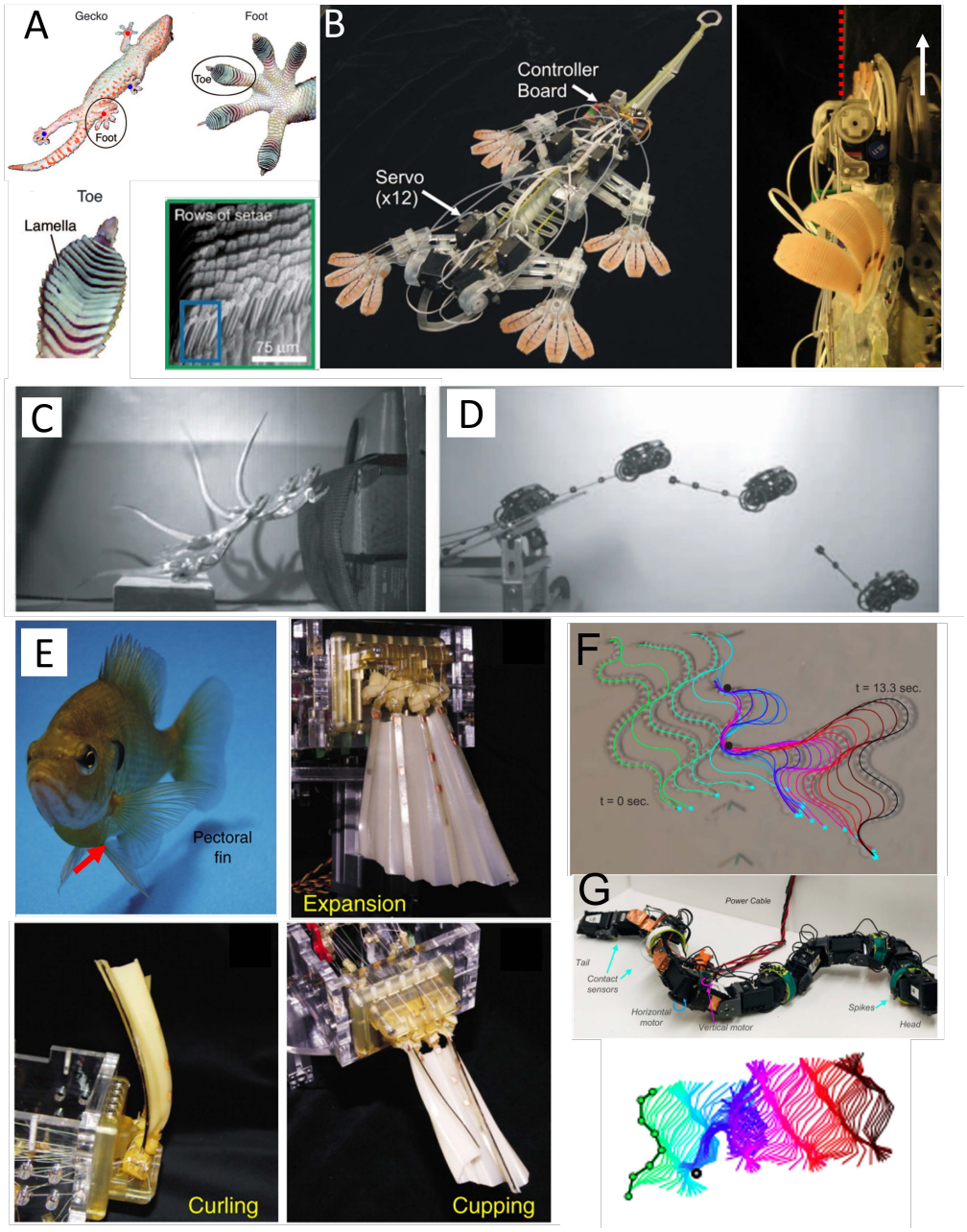

Figure 1.9: **Robophysical models and their biological counterparts.** (A) Gecko climbing (top left), a foot (top right) and toe (bottom left), and a microscopy image of the setae (bottom right). Red and blue dots corresponds to free and attached feet, respectively. (B) Gecko inspired robot. Right panel shows robot vertically climbing a surface. Arrow denotes the direction of motion. Figures adapted from [80, 81, 82]. (C) Lizard and (D) robot model using the tail to stabilize their body. Figure adapted from [83]. (E) Bluegill sunfish (top left) and robotic pectoral fin (remaining panels) with exhibiting different motions. Red arrow highlights pectoral fin. Figure adapted from [27]. (F) Sidewinder and (G) robophysical model using a propagate through behavior. Figure adapted from [40].

climbing is facilitated by setae (small hair-like structures) on their feet that adhere to surfaces through van der Waals forces, that depend on the limb-surface contact angle [80, 84, 81] (Figure 1.9A). During landing and lifting of each limb, the gecko changes the contact angle between the surface such that adhesion force is increased during landing and decreased during lifting [81]. Inspired by gecko climbing, researchers developed a robot model (Stickybot) that relies on directional synthetic adhesive pads [85, 82] (Figure 1.9B). Multiple levels of compliance at various length scales (from centimeters to micrometers) are implemented in the robot such that its body can conform to distinct surfaces [85]. The robot is able to climb multiple vertical surfaces using gecko-like movement [85].

Robots can also serve as simplified locomotors models that allow for repeatable testing in a controlled laboratory environment [43, 51, 86, 87, 83, 31, 27], an approach known as robophysics [88]. Parameters such as body morphology, joint/limb angles, actuation speed can be highly controlled (unlike in organisms) to study a resulting behavior. For instance, studies have found that red-headed agama lizards (*Agama agama*) actively control the swing of their tails to stabilize their bodies while jumping to an adjacent vertical surface [83] (Figure 1.9C). With the use of a lizard-size robot, researchers showed that an actively swinging tail leads to less body rotation and greater stability, in comparison to a robot with a passive tail or no tail [83] (Figure 1.9D). Similarly, studies done on bluegill sunfish (*Lepomis machrochirus*, Figure 1.9E) showed that the pectoral fin (on the lateral side of the body) can generate thrust on both the instroke (fin moving towards the body) and outstroke (fin moving away from the body); this is achieved by deformation across and along the length of the fin, as well as deformations of individual fin rays [89, 32, 33, 90, 27]. A robotic model of the pectoral fin not only captures the force patterns generated in sunfish but also demonstrated how stroke kinematic can alter the force production patterns [27] (Figure 1.9E). In limbless systems, studies of sidewinders have found that these animals exhibit primarily a ”propagate through” behavior (one of three behaviors observed) to negotiate sparse heterogeneities [40]. During a propagate through behavior, snakes lifts

a moving portion (not generating body-substrate contact) of its body and deforms it around an obstacle, propagating the deformation posteriorly as it continues sidewinding [40] (Figure 1.9F). Using a robophysical model, researchers found that the propagate through behavior is achieved by the modulation of the horizontal wave, in combination with firm anchoring of the anterior contact region [40] (Figure 1.9G). In all of the examples above, a robophysical modeling approach allowed researchers to discover principles behind a locomotor's behavior, providing insight that can further the development of robots.

1.6 Kinematic estimation to quantify behavior

To study organismal locomotion and control, accurate behavior quantification is desirable. As previously mentioned, in non-inertial regimes the locomotor's external behavior is dictated by internal shape changes. Therefore, extracting the geometrical configuration of the body and/or appendages is important to study a behavior of interest. We note that although not discussed here, some of the methods mentioned below can also be useful when studying multiple organisms and their collective behavior, such as flocking and schooling.

The simplest form of tracking consists of obtaining the centroid position over time [91]. This treats an organism as a single point, and can be useful when studying/measuring navigation or locomotion, although it cannot capture the organism's orientation or heading. To overcome this, researchers have used ellipses that cross the minor and major axis of the organism [91], when these are not symmetric (having the same length).

Typically, centroid or ellipse tracking is obtained via background subtraction, a scheme that differentiates the organism (foreground) and its surroundings (background). Background subtraction is achieved by generating a median image of all frames; the limiting factor of this approach is that it fails if the organism is static for an extended period of time. On the other hand, if there is sufficient contrast between the background and the foreground, a color or pixel intensity (for grayscale images) threshold can provide proper distinction between the two. We note that background subtraction, color thresholding,

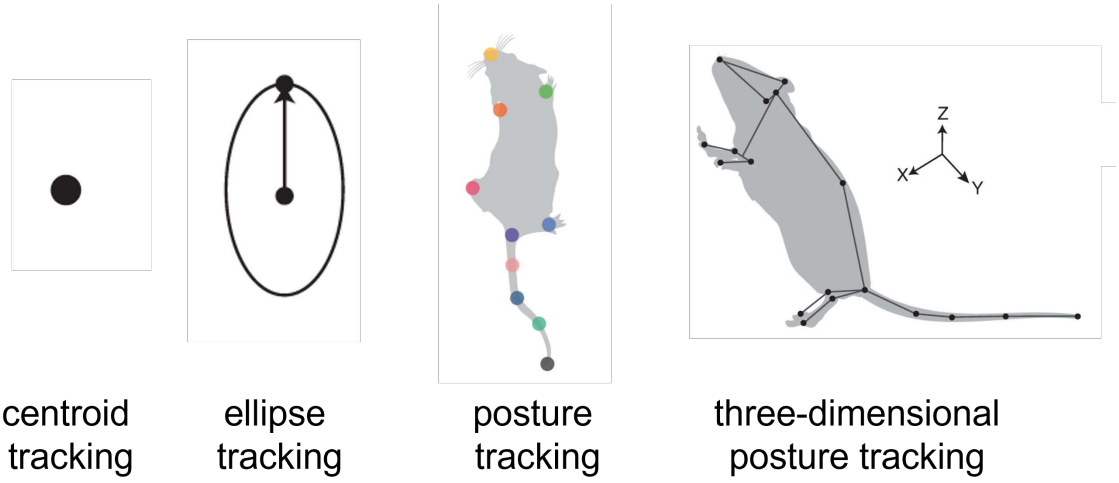

Figure 1.10: **Types of tracking approaches.** Diagrams of types of tracking approaches (from left to right): centroid tracking, ellipse tracking, posture tracking, and three dimensional posture tracking. Figure adapted from [91].

and/or pixel intensity thresholding are often sufficient to obtain body midlines of limbless organisms. However, if there are segments that collide or self-intersect (i.e., overlap), background subtraction and thresholding schemes cannot properly identify the bounds (i.e., edges) of the body, providing inaccurate body shapes and coordinates over time.

Both centroid and ellipse tracking cannot provide information of individual appendages, and thus cannot capture various animal behaviors (e.g., grooming and appendage coordination) [91]. This can be overcome by tracking the posture (also referred to as pose) of the organism over time. To do this, one approach consists of using physical markers (e.g., reflective); with high contrast between the marker, the organism, and the background, previously mentioned color or pixel thresholding schemes can be used to obtain each marker's position over time. In some cases, an external software is used such that tracking is simplified, accurate, and can capture three-dimensional motion, although such software can be costly [92, 93, 36]. While overlap of body segments and/or appendages can produce inaccurate coordinates, these can be remedied with manual annotation or digital filtering.

Another approach is the use of deep-learning based trackers, that rely on relatively minimal user input to provide posture estimation. A recently developed deep-learning based

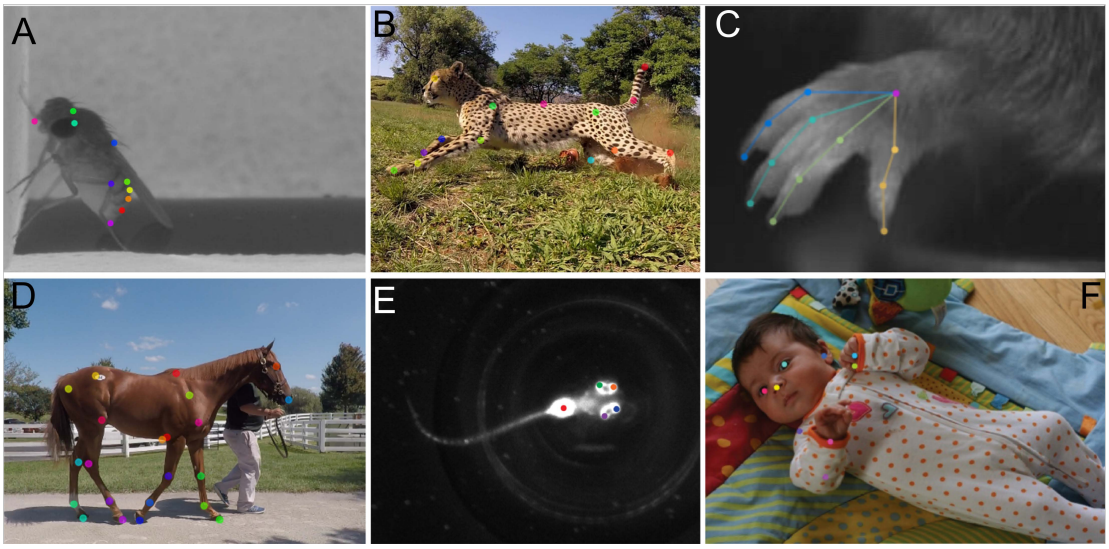

Figure 1.11: **Deep learning to track multiple systems.** Examples of DeepLabCut-applied labels: (A) a fruit fly, (B) a cheetah, (C) a mouse hand, (D) a horse, (E) a zebrafish, and (F) a baby. Figure adapted from [94].

tracker often used to quantify behavior is known as DeepLabCut (DLC) [95]. DLC is based on transfer learning with deep neural networks, with the use of minimal user input [95]. In short, DLC's routine proceeds as follows: 1) extract frames for manual annotation, 2) generate a training data set based on the annotated frames, 3) train networks on desired features (e.g., points along limbs), and 4) return features on remaining frames [95]. This has proven to be an effective tool to track many different systems (Figure 1.11). Previous studies have used DLC to study a variety of organisms and behaviors such as decision making in mice [96], spinal motoneurons and leg movement in human newborns [97], social interactions in bats [98], chicken behavior [99], body language in rodent social communication [100], and many others. Similar to posture tracking with physical markers, overlapping body segments and/or appendages can cause failures in the neural networks, and consequently, the outputted positions. In some cases, the annotation of additional frames and videos can result in more reliable tracking. In other cases, even with extensive manual labeling this software fails. Thus, manual annotation of the entirety of the trial is necessary but this can be laborious and time consuming.

1.7 Organization of the thesis

In this thesis, we will study undulators in highly damped regimes across scales. We study various systems ranging from limbless and few appendages to many-legged systems. These inhabit distinct environments, however, share the properties of non-inertial regimes. That is, locomotor performance is dependent on the internal shape changes due to viscous (in fluids) or frictional (in terrestrial substrates) damping, making inertial effects negligible. Thus, we focus on how these organisms coordinate their many degrees of freedom to exhibit a particular behavior. The rest of this thesis is organized as follows:

- **Chapter 2.** The study of *Cae. elegans* turning strategies in laboratory environments, adapted from a manuscript in preparation.

- **Chapter 3.** The effects of appendage coordination of hydrodynamics performance in quadriflagellate algae with the use of a robophysical model, adapted from a publication in *Bioinspiration and Biomimetics* [43].

- **Chapter 4.** The role of active and passive mechanics in centipedes (*Scd. polymorpha* and *Scc. sexspinosus*) traversing rugose terrains, adapted from a submitted publication in the *Journal of Experimental Biology* [101].

- **Chapter 5.** The swimming dynamics of a centipede (*Li. forficatus*) swimming on the water surface, adapted from a submitted publication to *Physical Review Letters* [102].

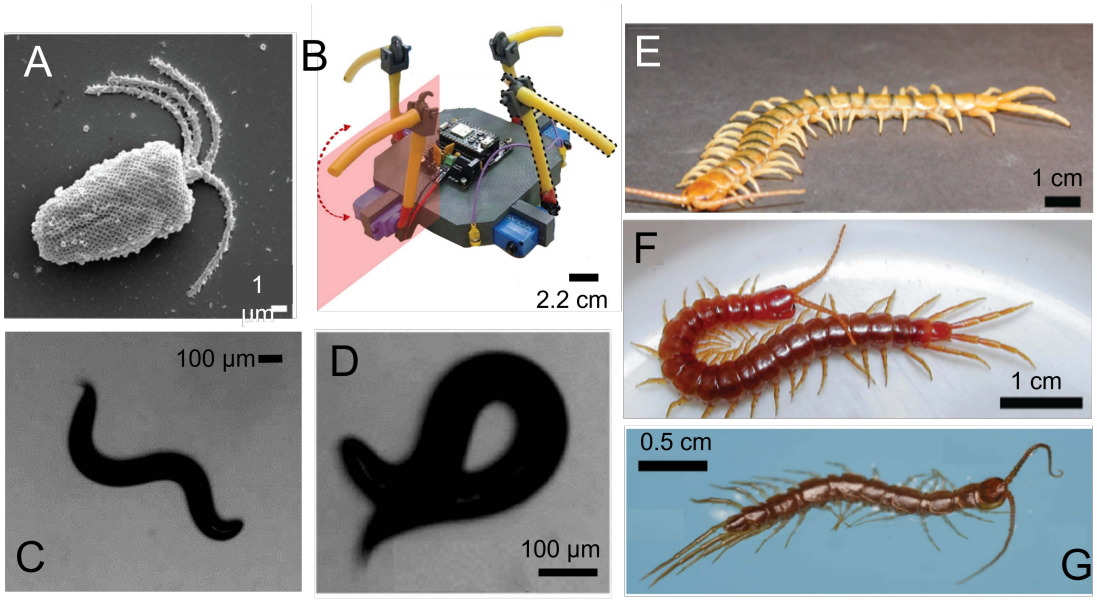

Figure 1.12: **Undulators studied in this thesis.** (A) Scanning electron microscope image of quadriflagellate algae (*P. gelidicola*). (B) Robophysical model of quadriflagellate algae. Figures adapted from [43]. *Cae. elegans* exhibiting postures during (C) forward motion and (D) and omega turn. Centipedes, (E) *Scd. polymorpha* and (F) *Scc. sexspinosus*, studied in comparative study, traversing rough terrains. Figures adapted from [101] (G) Surface swimming centipede, *Li. forficatus.* Figure adapted from [102].

CHAPTER 2

CAE. ELEGANS TURNING BEHAVIORS

2.1 Summary

To navigate various environments, slithering animals (e.g., snakes, nematodes) generate traveling waves of body curvature. Of interest is the mm-long nematode worm *Caenorhabditis elegans*; often thought of as simple with only 302 neurons, this worm is capable of exhibiting a variety of locomotor behaviors (e.g., turns, reversals, pirouettes). Although the neuromechanical control of forward locomotion in *Cae. elegans* is well researched and understood, much remains unknown of worm turning. Here, we investigate two known turning behaviors exhibited by the worms on agar, omega turns and small-angled turns, and analyze the body undulation dynamics. Using PCA analysis and geometric modeling, we find that omega turns and small-angled turns are not distinct turning behaviors; instead they fall into the same spectrum of turning behaviors. Turning can be modeled as a superposition of two traveling waves (turning and forward wave) with distinct spatial frequency. Changes in turning behaviors and degree of turning are subject to amplitude modulation of the turning wave. In fluid (M9 buffer), dimensionality reduction cannot capture superimposed traveling waves due to indistinguishable spatial frequencies. Instead, turning can be modeled as a single body wave, subject to both amplitude modulation and phase modulation.

This chapter's contents are adapted from a co-first authored manuscript in preparation by Baxi Chong*, Kelimar Diaz*, Christopher Pierce, Eva Erickson, and Daniel I. Goldman

2.2 Introduction

Animals move in a variety of environments throughout their lifetime. Limbed animals use their appendages to make and break discrete contact with their surroundings and generate motion. On the other hand, limbless animals rely solely on their body; limbless locomotors primarily rely on waves of body undulation, continuously generating body-substrate contact, and achieving propulsion. While undulatory locomotion is ubiquitous and remarkably robust, there is much to understand regarding the control principles that underlie this environmentally versatile locomotion strategy.

Cae. elegans is a model system that can increase our understanding of undulatory neuromechanical control due to its highly versatile locomotion [7, 5]. Previous studies showed this worm modulates its undulatory wave across fluids (and non-Newtonian fluids) with viscosity spanning several orders of magnitude. Further, this worm encounters a variety of environments in nature; it can be found in rotting fruit, damp soil, and potentially the body of molluscs (e.g., slugs) [6] (Figure 2.1A). In these environments, *Cae. elegans* may encounter heterogeneities that challenge its navigational capabilities.

Forward motion has been extensively studied in *Cae. elegans* [8, 5, 7]. The undulation wavelength and frequency depend on the resistance of the surrounding medium; with increasing medium resistance, the worms exhibit increasing wavelengths and decreasing undulation frequencies [5]. This modulation of undulation wavelength and frequency has been found to be partially driven by proprioceptive neurons that detect the worm's local deformations [103, 104].

Less is known about worm maneuvering strategies, such as turning. Previous studies on worm turning have focused primarily on omega turns, during which the worm generates high curvature bends forming an omega (Ω) shape with its body [105] (Figure 2.1B). These studies have shown that omega turns allow the worms to explore their surrounding environments [106], avoid navigational bias [107], and escape external noxious stimuli [108]. Yet,

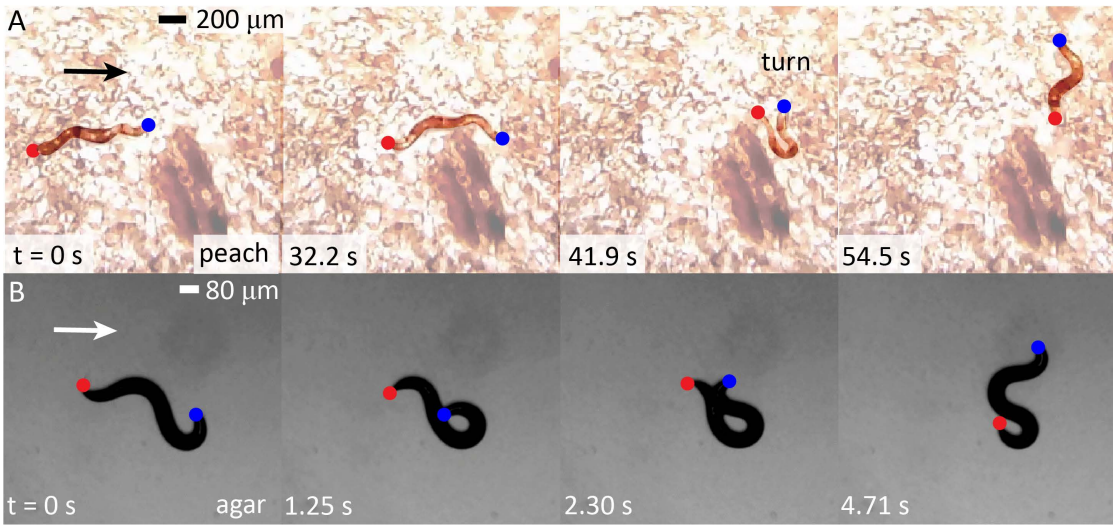

Figure 2.1: ***Cae. elegans* in naturalistic and model environments.** Snapshots of *Cae. elegans* locomoting and performing an omega turn on (A) rotten fruit (peach) and (B) agar. Blue and red circles denote the head and tail, respectively. Arrows show direction of motion.

how these animals generate and control for turning behaviors remains unknown. We posit the ability for these worms to perform turns is essential for maneuverability and navigation in complex environments, such as those that they encounter throughout their life-cycle.

Whether in fluids or in agarose gel, *Cae. elegans* locomotes in dissipative environments. That is, the ability for this worm to generate propulsion depends on internal shape changes to overcome damping. A powerful tool to relate shape changes to some external behavior is geometric mechanics. Geometric mechanics was developed in the 1980s to study locomotion in low Reynolds number regimes [72, 109]. Instead of laborious calculations, geometric mechanics offers a diagrammatic approach with the use of height functions, providing insight into the patterns of self-deformation in non-inertial systems [39, 110, 15].

Here, we study *Cae. elegans* turning strategies, namely small-angled and omega turns, in both laboratory model environments (agar and fluid). Using dimensionality-reduction techniques, we find that these turns can be rationalized as a superposition of two traveling waves with distinct spatial frequency: a forward wave and a turning wave. We show with a geometric approach that changes in the turning behavior and consequently the turning rate

are subject to amplitude modulation of the turning wave. This suggests that two turns, that have been considered discrete behaviors, arise from a single control mechanism.

2.3 Materials and methods

2.3.1 *Cae. elegans* preparation

Prior to an experimental trial, worms were washed in M9 buffer to remove any bacteria on the animals' body. A single worm was placed per agar plate and M9 buffer bulk fluid. For experiments performed in M9 buffer, animals were placed in 25 μL of M9 buffer on a glass slide. 3D movement was not constrained, only turns that occurred primarily in two dimensions were selected.

2.3.2 *Cae. elegans* kinematics

Worm turning kinematics were captured at 30 frames per second (fps) via a bright field microscope (Leica ATC 2000) and a point gray camera (Basler, acA1300-200um). Custom MATLAB code was used to digitize kinematics of small-angled turns. Kinematics of omega turns were digitized using the animal-pose estimation software DeepLabCut (DLC) [95]. Animal mid-lines were interpolated to 90 equally-spaced points along the worm's body using a cubic spline fit. Mid-lines were used to calculate the curvatures (κ) using custom MATLAB code. Net rotation was measured by calculating the angle between the body posture before and after an omega turn (Figure 2.10A).

2.4 Results and discussion

2.4.1 Dimensionality reduction of turning behaviors

We performed animal experiments on plates of nematode growth media (NGM, unseeded) agar and M9 buffer (see Materials and methods). When placed on agar plates, the worms would roam the plate and perform distinct turning strategies (i.e., small-angled and omega

turns). Small turns can be described as a small bend generated on the head and propagated along the body to produce a change in the heading angle (Figure 2.2A). In contrast, omega turns are generated when the worm's head sweeps near the tail, forming an omega-like shape with its body (Figure 2.2B). We note that worms are capable of performing delta turns - omega turns with greater body amplitude [107]. However, in our analysis, we did not differentiate between omega and delta turns. While previous work suggests that omega and delta turns are "triggered" by separate processes, overall these two turns have similar kinematics, turning rates, and contribute little bias in the direction of the animal's trajectories [107].

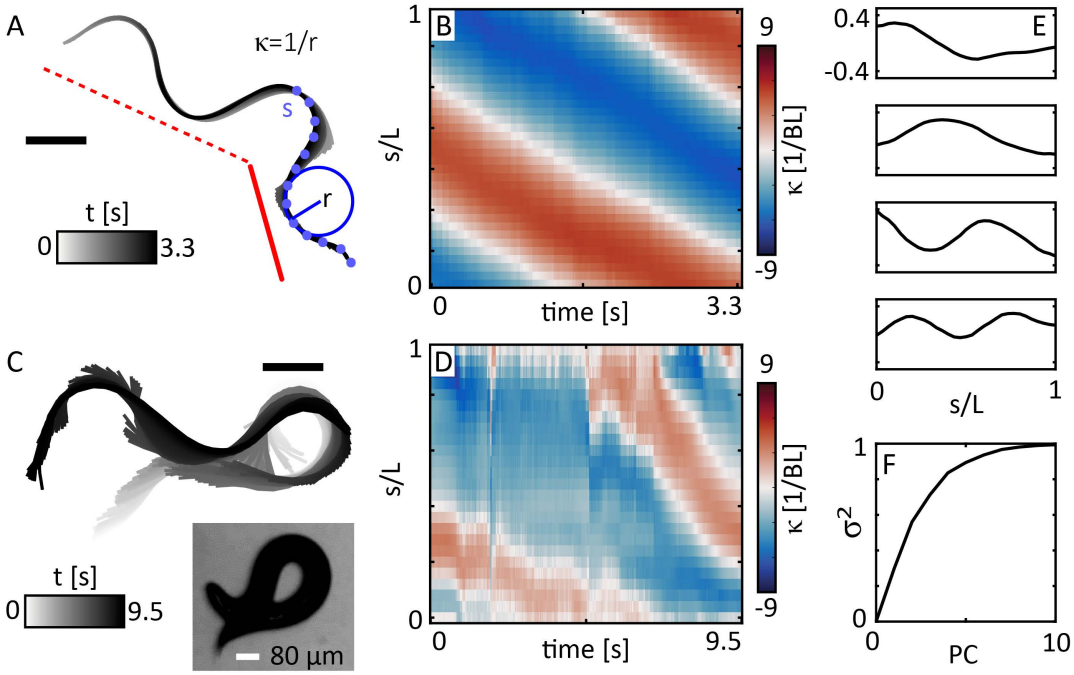

Figure 2.2: ***Cae. elegans* turning strategies.** (A) Example trajectory of a small-angled turn on agar, colored by time. Dashed and solid red line denote direction of motion before and after the turn. Scale bar corresponds to 80 μm. (B) Space-time plots of curvatures, κ, for trajectory shown in (A). (C) Example trajectory of an omega turn on agar, colored by time. Scale bar corresponds to 80 μm. (D) Space-time plots of curvatures, κ, for trajectory shown in (C). (E) PCA of κ for both small and omega turns on agar. (F) Variance explained (80%) for the first four components.

Principal component analysis (PCA) on animal postures has been used to describe an

animal's behavior [8, 36]. In previous studies, a single principal component (PC) corresponds to turning behaviors [8] when a worm is roaming on a plate and exhibits a variety of behaviors. In addition, forward locomotion is represented by linear superimposition of sinusoidal PC pairs (i.e., two PCs capture forward motion) [8, 39]. Instead of performing PCA on roaming worms (encompassing a wide range of behaviors) we performed PCA solely on turning behaviors on agar and found that four PCs capture most of the variation in the body postures (80% of the variance) (Figure 2.2E-F). Three out of these four PCs have similar counterparts to those reported in [8]. However, a single PC (PC_2) emerges that is associated with turning. Further, we find that PC_1 and PC_2 can describe turning behaviors and share a similar spatial frequency (number of waves along the body) of $n_t = 1$. On the other hand, PC_3 and PC_4 are present during forward motion and also have a similar spatial frequency of $n_f = 1.5$, consistent with previous work [8, 39]. The similarities in spatial frequency between PC pairs (PC_1 and PC_2, PC_3 and PC_4) suggests these correspond to sinusoidal pairs and can represent traveling waves [111]. Thus, we posit *Cae. elegans* turning is achieved by controlling two superimposed traveling waves, represented by pairs of sinusoidal PCs.

We use these four PCs as a low dimensional representation of turning behaviors, approximating curvature changes overtime as:

$$\kappa(s,t)\lambda_s = \alpha_1(t)\beta_1(s) + \alpha_2(t)\beta_2(s) + \alpha_3(t)\beta_3(s) + \alpha_4(t)\beta_4(s) \tag{2.1}$$

where s corresponds to a point along the body from head to tail, and β_i and α_i correspond to each PC and its amplitude, respectively. Equation 2.1 can be written as

$$\kappa(s,t)\lambda_s = \omega_1 cos(\phi_1)\beta_1(s) + \omega_1 sin(\phi_1)\beta_2(s) + \omega_2 cos(\phi_2)\beta_3(s) + \omega_2 sin(\phi_2)\beta_4(s) \tag{2.2}$$

where ω_1 and ϕ_1 correspond to the amplitude and phase of the turning wave, and $omega_2$ and ϕ_2 correspond to the amplitude and phase of the forward wave. Simplifying Equa-

tion 2.2, the resulting expression becomes

$$\kappa(s,t)\lambda(s) = \omega_1 sin(2\pi s n_1/L + \phi 1) + \omega_2 cos(2\pi s n_2/L + \phi_2) \tag{2.3}$$

where L corresponds to the length of the animal, and n_1 corresponds to the spatial frequency of the turning wave (n_t), and n_2 corresponds to the spatial frequency of the forward wave (n_f).

2.4.2 Geometric framework for turning

To investigate how *Cae. elegans* coordinates two traveling waves to generate turns, we use the geometric mechanics framework. Geometric mechanics is a physical and mathematical tool that can be used to analyze animal behavior [39, 110, 15]. This geometric framework has been previously used to study forward propulsion of various systems such as sand-swimming lizards, salamanders, snakes [39, 110, 15], and even synthetic locomotors (robot models) [112, 110, 113, 114]. Further, geometric mechanics has been successfully used to study turning behaviors [115, 116, 39, 117, 110].

To introduce this framework, consider forward motion of a system in which movement can be captured by a two dimensional representation of its body postures, such as in *Cae. elegans* [8, 39] and other undulators [36, 39]. Then, a gait can be represented as a closed loop in the shape space (body postures that the locomotor can adopt), where any given closed loop in the shape space can lead to distinct locomotor dynamics (Figure 2.3A-B). That is, small body shape changes are related to small changes in both rotation and translation. In geometric mechanics, and these are assumed to be linearly related as

$$\boldsymbol{\xi} = A(\boldsymbol{\alpha})\dot{\boldsymbol{\alpha}} \tag{2.4}$$

where $\boldsymbol{\xi} = [\xi_x\ \xi_y\ \xi_\theta]^T$ is the forward, lateral, and rotational body velocities, $\boldsymbol{\alpha} = [\alpha_1\ \alpha_2]^T$ is the body shape, $\dot{\boldsymbol{\alpha}}$ is the velocity at which the body is changing shapes ("shape" veloc-

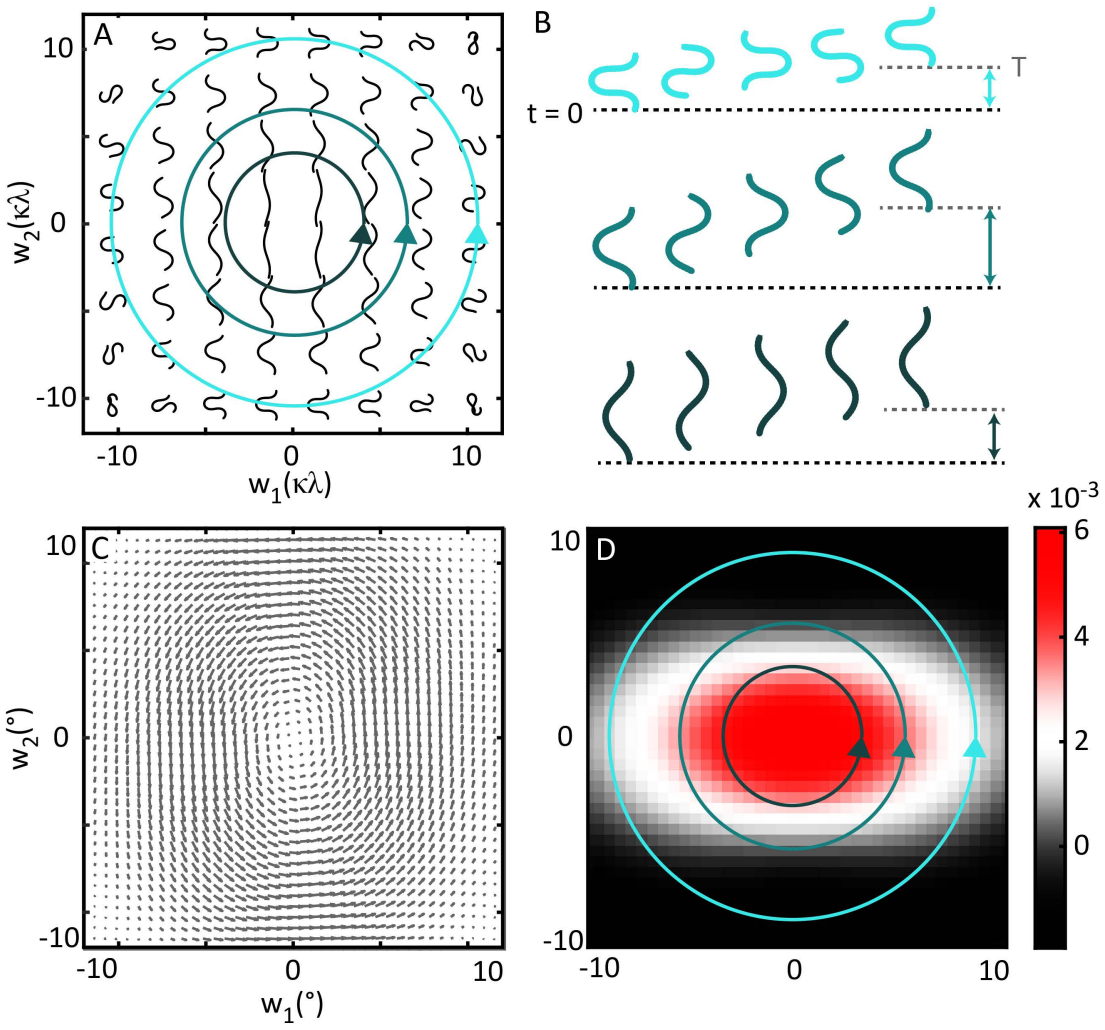

Figure 2.3: **Geometric framework for worm locomotion.** (A) A two-dimensional shape space. The shape basis functions of the shape space are derived from eigen-worms observed during worm forward motion. The wave of traveling body curvature can be represented by circular paths in the shape space. (B) Sequences of body shape changes over a gait period (left to right) for three distinct (different amplitudes) circular paths leading to different net displacement. (C) Connection vector field corresponding to forward motion. (D) Height function corresponding to forward motion.

ity), and A is the local connection which relates $\boldsymbol{\xi}$ and $\dot{\boldsymbol{\alpha}}$. Equation Equation 2.4 separates the position and orientation (group variables) of the locomotor from the exhibited shapes (shape variables), providing an explicit map that relates shape changes to displacement in the world frame. For a two dimensional reduced shape space ($\boldsymbol{\alpha} \in \mathbb{R}^2$), the local connection ($A(\boldsymbol{\alpha})$) is a 2x3 matrix where each forms a "connection vector field" (Figure 2.3C). However, determining performance from a connection vector field can be challenging and

non-intuitive. To overcome this challenge we can leverage Stokes' theorem [118, 119].

For any given closed loop, $\partial\psi$, in the shape space, displacement can be approximated by

$$[\Delta x\ \Delta y\ \Delta\theta]^T = \int_{\partial\psi} A(\boldsymbol{\alpha})\dot{\boldsymbol{\alpha}}d\boldsymbol{\alpha} \tag{2.5}$$

Then, by Stokes' theorem, the line integral along $\partial\psi$ is equal to the area integral of the curl of $A(\boldsymbol{\alpha})$ over the surface area encompassed by $\partial\psi$:

$$\int_{\partial\psi} A(\boldsymbol{\alpha})\dot{\boldsymbol{\alpha}}d\boldsymbol{\alpha} = \int\int_{\psi} \nabla \times (A(\boldsymbol{\alpha}))d\alpha_1 d\alpha_2 \tag{2.6}$$

where ψ corresponds to the area encompassed by $\partial\psi$ and the curl, $\nabla \times (A(\boldsymbol{\alpha}))$, corresponds to the "height function" (Figure 2.3D). A height function provides a visual map to identify the output displacement given a pattern of self-deformation without the need for parametrizations of stroke patterns [120]. A closed path that encloses a greater amount of positive area, resulting in a large area integral, and consequently a greater displacement (Figure 2.3). Given the dimensions of $A(\boldsymbol{\alpha})$, a height function can be obtained for forward, lateral, and rotational displacement.

As previously mentioned, PCA revealed that turning behaviors in *Cae. elegans* can be described as a superposition of traveling waves (two-wave template), a forward and a turning wave, similar to [117] can be given by

$$\kappa(s,t)\lambda(s) = \omega_1 sin(2\pi s n_1/L + \phi 1) + \omega_2 cos(2\pi s n_2/L + \phi_2). \tag{2.7}$$

Figure 2.4A(i)-A(iii) shows the shape space spanned by the two traveling waves. As mentioned above, connection vector fields can be obtained, for which each arrow corresponds to infinitesimal rotation (Figure 2.4B(i)-B(iii)). Height functions in Figure 2.4C(i)-C(iii show paths that optimize turning rate and minimize collisions (Figure 2.4D(i)-D(iii)), similar to those in [117]. We note, self-intersection may be an important feature of omega

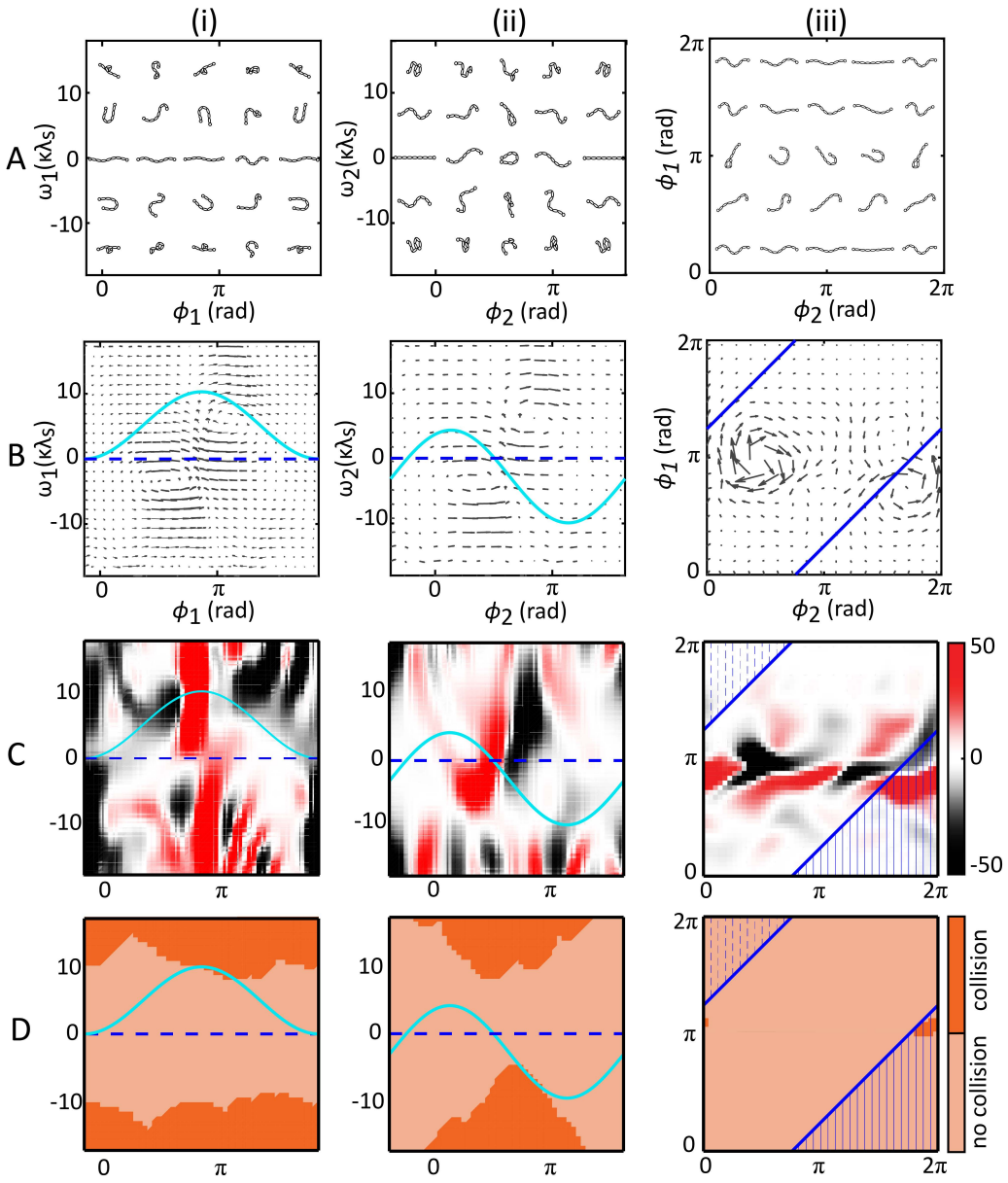

Figure 2.4: (A) The two-dimensional shape sub-space for (i) coordination between amplitude modulation and phase modulation of turning wave, (ii), coordination between amplitude modulation and phase modulation of forward wave (iii) coordination between forward wave and turning wave. (B) Connection vector field corresponding to (i), (ii), (iii). (C) Height function corresponding to (i), (ii), (iii). (D) Self-collision maps on the shape space for (i), (ii), (iii). Light solid blue line corresponds to gait paths that maximize the surface integral while avoiding the self-collision regions. Dashed dark blue line corresponds to assistive lines used to form closed loops with the gait path. Solid dark blue line corresponds the integral of the surface enclosed in the lower right corner (shadow by solid line) minus the surface enclosed in the upper left corner (shadow by dashed line) [120].

turns, however we avoid such body configurations in our analysis. Further, while proper phasing between the forward and turning wave is important to optimize turning rate, in this study we focus on two distinct turning behaviors that are at two opposite ends of the spectrum. That is, while omega turns generate high net rotation, small-angled turns, as the name suggests, produce a low net rotation [8, 107, 106]. Aside from the generated rotation, there is a similar feature in these two turns; when the worm is turning there is a change in the amplitude at the head. Thus, we posit that these turns, although visually discrete, lie on a continuum and are subject to amplitude modulation. In other words, *Cae. elegans* can exhibit an omega or a small-angled turn by modulating the amplitude of the superimposed traveling waves.

To investigate this hypothesis, we used the geometric framework to obtain a theoretical prediction of rotation (as degrees per cycle) as a function of off-origin distance (x_c) of the trajectories of the PC projections (Figure 2.5). The off-origin distance serves as a proxy for changes in the amplitude during turning, as forward motion produces trajectories that are centered at the origin, and the animal exhibits negligible rotation in the world frame [8, 39]. Figure 2.5B shows two trajectories of the PC projections of the turning wave. We observed that the trajectory of the small-angled turn is centered approximately at the origin, whereas the trajectory for the omega turn is shifted toward the negative direction along the x-axis. Thus, there is increasing rotation with increasing off-origin distance, captured by both empirically measured data as well as the geometric mechanics prediction (Figure 2.5C). The relationship between net rotation and off-origin distance measured in experimental data reinforces the hypothesis that turning behaviors observed in *Cae. elegans* lie on a continuum. That is, what was thought to be two distinct turning behaviors, small-angles turns and omega turns, can be described as a single behavior with a two superimposed waves.

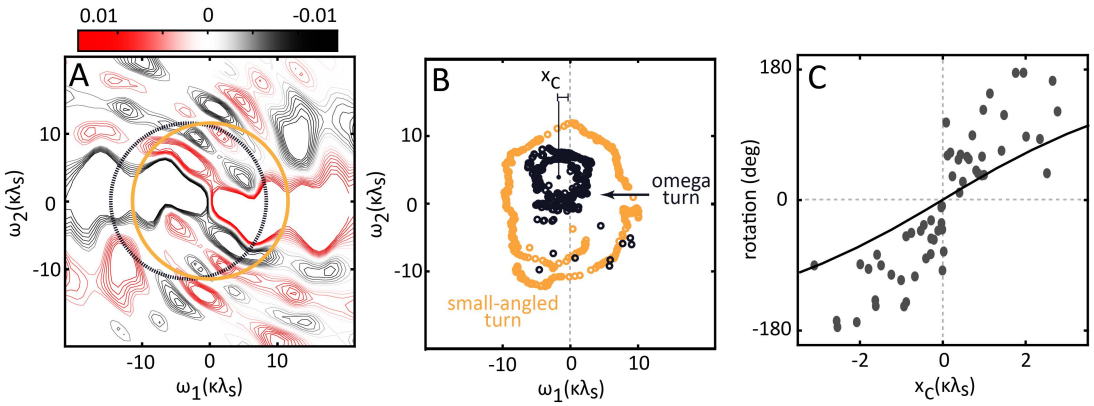

Figure 2.5: **Geometric mechanics prediction of worm turning on agar.** (A) Height function corresponding to the turning wave. The shape space is defined as the linear space spanned by PC_1 and PC_2. (B) Experimentally obtained trajectories formed during an omega and small turn. (C) Rotation as a function of off-origin ellipse centroid distance, x_c. Solid black lines corresponds to geometric mechanic prediction.

2.4.3 Turning behaviors in fluids

Similar to on agar, worms spontaneously perform turns in fluids. These look kinematically comparable but the lower resistance from the media affects both the undulation wavelength and frequency [5]. Adopting the dimensionality reduction approach, we performed PCA on turning behavior in fluid (Figure 2.6A-D). Unlike in agar, two sinusiodal PCs capture the majority of the variance in the worm's body postures (78% of the variance) (Figure 2.6E-F). This would suggest that the neuromechanical control for turning is dependent of the environment. However, this is inconsistent with this worm's strategy for forward motion, where a single gait is modulated across environment of distinct resistance [5]. Thus, we hypothesize that PCA could not capture a two wave template if the spatial frequencies between the forward and turning wave were comparable, collapsing these into a single wave with a spatial frequency of $n = 0.7$.

To test our hypothesis, we theoretically analyzed the orthogonality (ψ) between spatial frequencies. That is, we verified if comparable spatial frequencies would be distinguishable by PCA. When $\psi = 90°$, spatial frequencies are distinct and can thus be captured by PCA. Figure 2.6G shows ψ for varied spatial frequency of the turning wave, while keeping

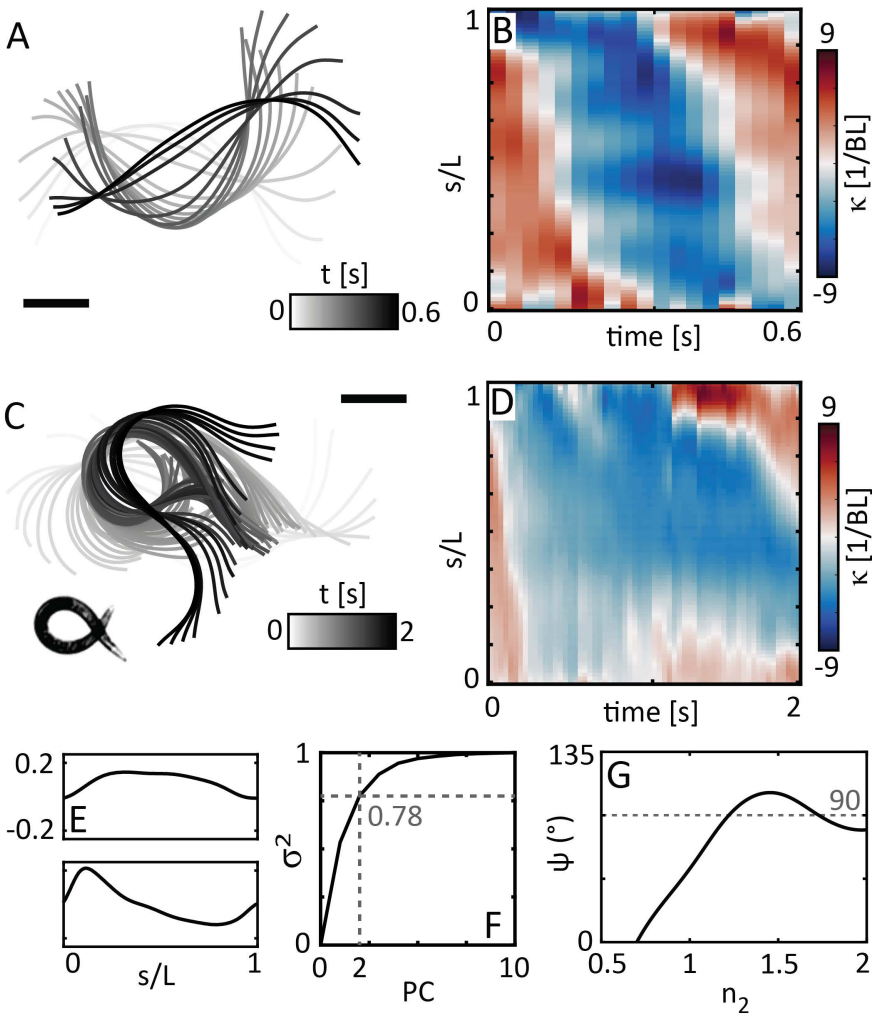

Figure 2.6: ***Cae. elegans* turning in fluids.** (A) Example trajectory of a small-angled turn in fluid, colored by time. (B) Space-time plots of curvatures, κ, for trajectory shown in (A). (C) Example trajectory of an omega turn in fluid, colored by time. Scale bars correspond to 80 μm. Inset shows photo of *Cae. elegans* in buffer performing an omega turn. (D) Space-time plots of curvatures, κ, for trajectory shown in (C). (E) PCA of κ for omega turns in buffer. (F) Variance explained (78%) for the first two components. (G) Theoretical simulations of orthogonality between spatial frequencies.

the spatial frequency of the forward wave fixed ($n_1 = 0.7$). We observed that spatial frequencies below 1.25 decreases ψ, increasing the difficulty to distinguish between the forward and turning wave.

Similar to agar, we apply the geometric framework to turning behaviors in buffer obtain a to predict rotation as function of x_c of the trajectories of the PC projections (Figure 2.7). Figure 2.7B shows two trajectories of the PC projections. Consistent with our observations

of turning behaviors on agar, we find that rotation increases with increasing x_c. This is once again captured by both empirically measured data as well as the geometric mechanics prediction (Figure 2.7C).

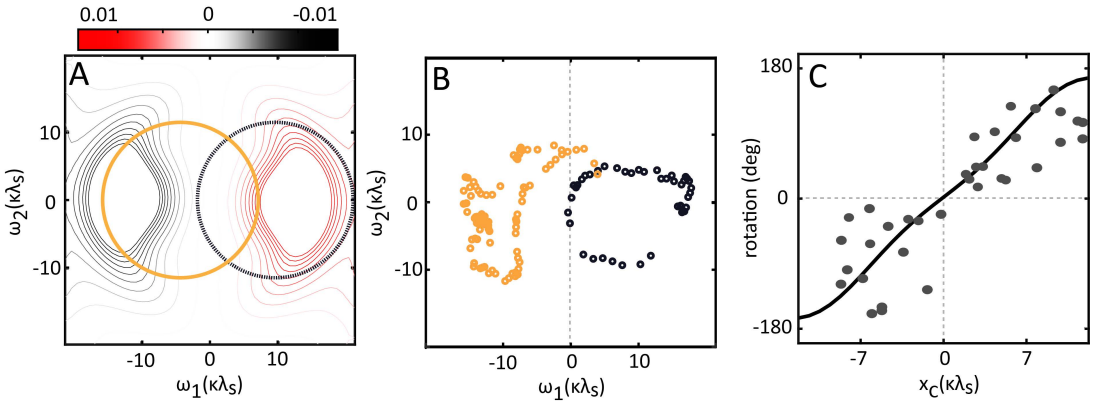

Figure 2.7: **Geometric mechanics predictions for worm turning in fluid.** (A) Height function corresponding to the turning in buffer. The shape space is defined as the linear space spanned by PC_1 and PC_2. (B) Experimentally obtained trajectories formed during two distinct turns. (C) Rotation as a function of off-origin ellipse centroid distance, x_c. Solid black line corresponds to geometric mechanic prediction.

The difference between agar and buffer is that, since the turning and forward wave collapse into one, the change of behavior from forward to turning can be observed in the trajectories of the PC projections. In buffer, a circle centered about the origin [39] corresponds to forward motion, and any turning motion causes the trajectory to shift away from the origin. Figure 2.8 shows a trajectory of the projections for a worm performing both forward motion and turning, resulting in two distinct ellipses. When the worm is thrashing to move forward, it is also performing a long turn. In other words, in the world frame the path that the worm is traveling is curved, resulting in a distinct ellipse (left-most, dashed line in Figure 2.8) in the projections. As time progresses, the worm spontaneously performs an omega turn that changes the trajectory into a different ellipse (right-most, solid line in Figure 2.8). Once the worm finishes performing an omega turn and continues thrashing, the trajectory returns to the first ellipse.

We tested whether a two-wave template could capture omega turns in a robophysical model (length = 102 cm, width = 5 cm, 8 segments). As described in [117], each segment

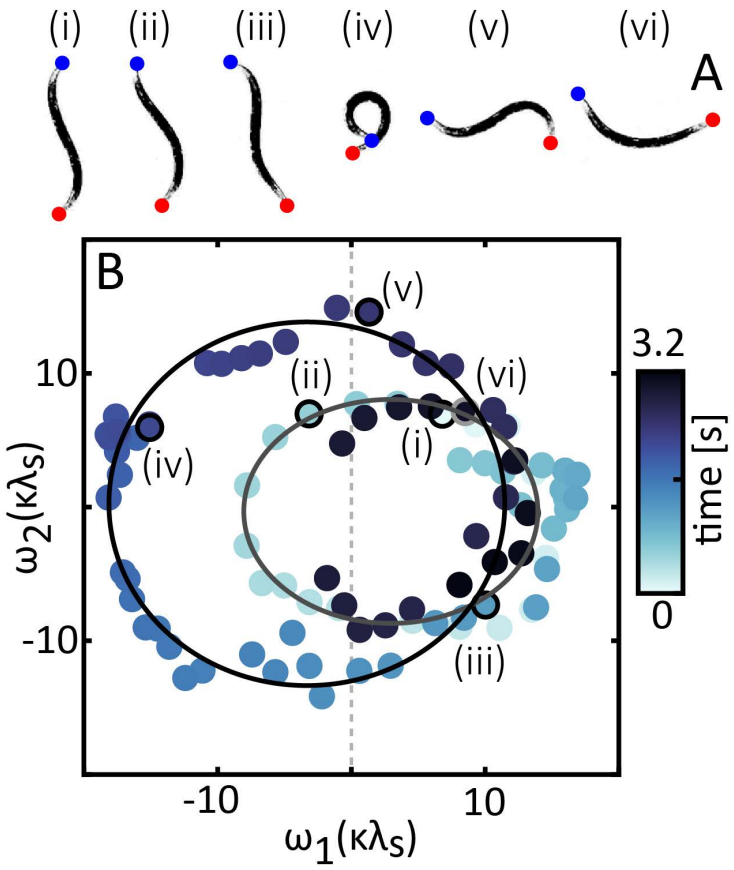

Figure 2.8: **Forward motion and turning is captured by trajectories of PC projections.** (A) Snapshots of *Cae. elegans* performing forward motion and an omega turn. Blue and red circles correspond to the head and the tail of the worm, respectively. (B) Trajectories formed by two modes during both forward and turning, colored by time. Ellipses correspond to trajectories during forward motion (solid gray) and an omega turn (solid black).

is commanded to achieve a joint angle prescribed by

$$\theta_i = \omega_1 sin(\phi_1 + 2\pi n_1 \frac{i}{N}) + \omega_2 sin(\phi_2 + 2\pi n_2 \frac{i}{N}) \tag{2.8}$$

where i corresponds to the joint index and N corresponds to the total number of joints (ω_1, n_1, ϕ_1, ω_2, n_2, and ϕ_2 have the same definition as in Equation 2.7). As observed in Figure 2.9 with this two-wave template the robot successfully executes an omega turn and captured body rotation over a gait cycle.

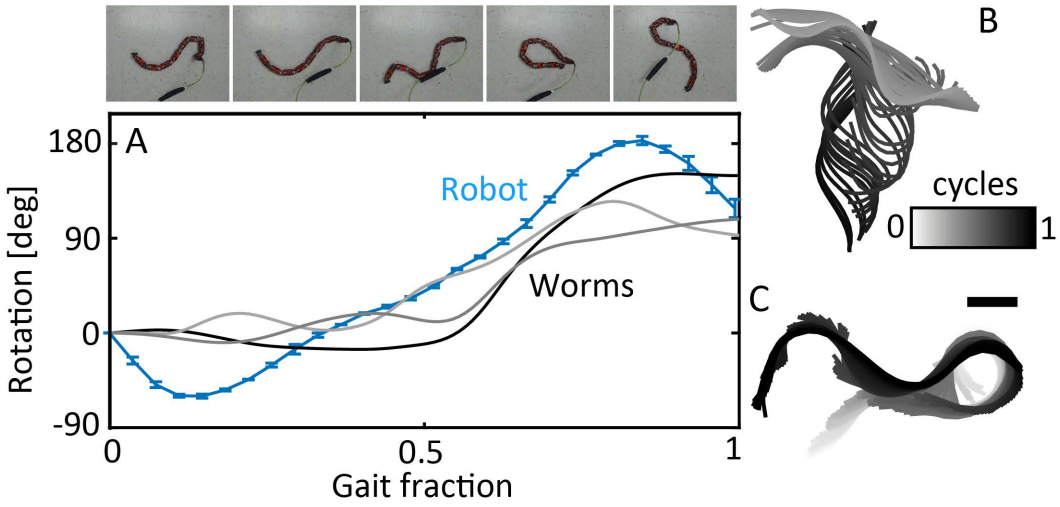

Figure 2.9: **Robophysical modeling of worm turning.** (A) Rotation over a single gait cycle for robophysical model using a two-wave template to perform turns. Blue and gray lines correspond to the robot and animal trials, respectively. Top inset shows snapshots of the robot performing an omega turn. (B) Example trajectory of an omega turn performed by the (B) robot and (C) the worm, colored by time.

2.5 Conclusion

We studied *Cae. elegans* turning behaviors in laboratory environments, using both agar and fluid (M9 buffer) media. Specifically, we focused on two turning behaviors, small-angled and omega turned. Using dimensionality-reduction techniques (PCA), we found that turning behaviors could be described as a superposition of two sinusoidal traveling waves with distinct spatial frequency. Geometric mechanics predicted rotation performance and consequently turning behavior could be related to the off-origin distance from the center of the trajectories of the PC projections. In fluid, PCA did not capture the superposition of two waves, we posit, due to comparable spatial frequency between the waves. Nonetheless, the same relationship was predicted using geometric mechanics. Our work suggests that although small-angled and omega turns are thought to be distinct turning behaviors, these are generated and controlled by the turning wave; by modulating the amplitude of the turning wave, the worm can achieve either small-angled or omega turns.

While not studied here, we posit these turns allow *Cae. elegans* to maneuver across

complex heterogeneous environments, such as those that they encounter in nature (subsection 2.7.1). Previous work [117] has shown that a two-wave template allows limbless robots to maneuver within a model heterogeneous terrain (i.e., randomized lattice). This is unlike other strategies that require complex control to facilitate lattice traversal [121]. Thus, we expect our work can lead to augmented capabilities of present and future limbless robots for maneuvering diverse terrains.

2.6 Contributions

The contributions for the project are detailed as follows:

Kelimar Diaz performed *Cae. elegans* turning experiments, tracked the animal postures in fluid, and assisted in analysis and processing of the data (i.e., PCA). Eva Erickson performed tracking of animal postures on agar. Baxi Chong developed and applied the geometric mechanics framework. Tianyu Wang programmed and performed robot experiments. Baxi Chong, Kelimar Diaz, Christopher Pierce, and Daniel I. Goldman conceived the study and interpreted the data. Baxi Chong, Kelimar Diaz, and Christopher Pierce co-wrote the manuscript in preparation. Daniel I. Goldman supervised project, provided comments on and modified the manuscript.

2.7 Appendix

2.7.1 Turning performance in confined environments

We performed preliminary experiments with *Cae. elegans* on fluid-filled (M9 buffer) hexagonal lattices (spacing between posts = 320 μm, post diameter = 200 μm) to test turning performance in heterogeneous environments. We focused solely on omega turns and compared the turning performance with omega turns observed on agar and in fluid (M9 buffer). Net rotation was measured by calculating the angle between the body posture before and after an omega turn (Figure 2.10A). Further, we measured swept area (normal-

ized by the total area a worm *could* sweep, the area of a circle) by calculating the area of each omega turn trajectory (Figure 2.10B). We observed that *Cae. elegans* can achieve high turning performance independent of the environments (Figure 2.10C). Interestingly, similar to the observations for forward motion [9, 10], opportunistic use of the posts may enhance turning performance relative to homogeneous fluid. Similarly, we observed that omega turns allows the worms to sweep a small area, potentially enhanced with opportunistic post used in fluids (Figure 2.10D).

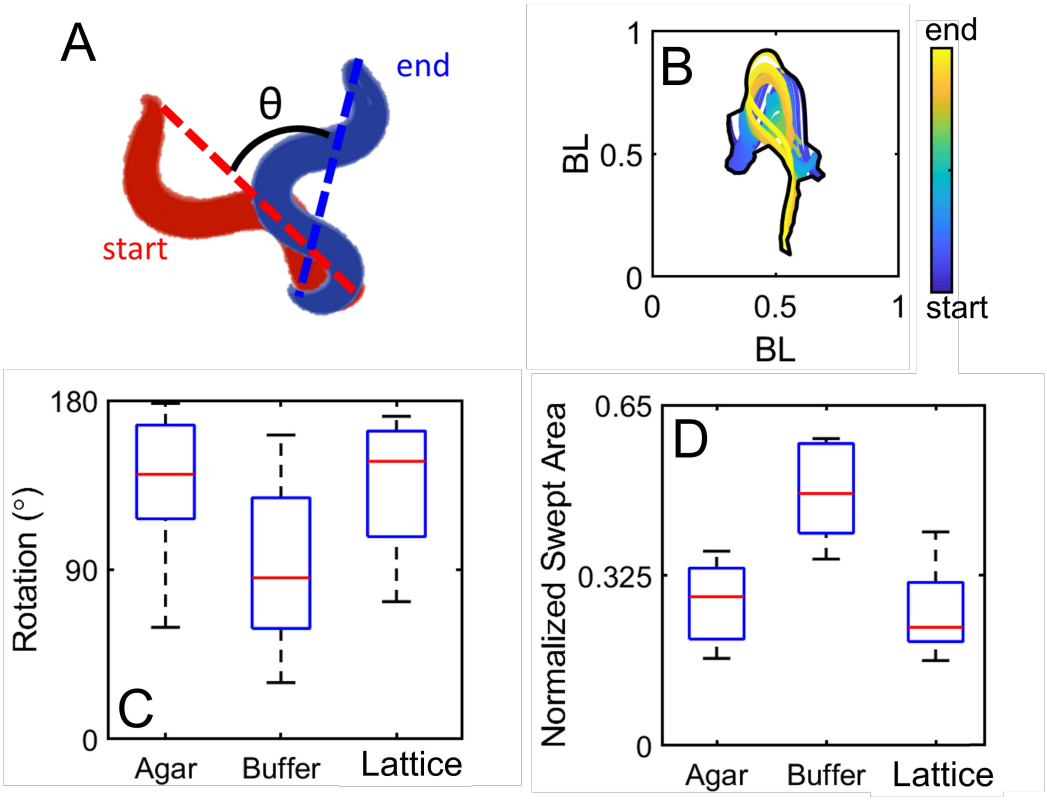

Figure 2.10: **Omega turns in various environments.** Snapshot of the perpendicular robophysical model swimming in mineral oil. Average position between LEDs was used as a proxy for robot body centroid due to the fluid opacity. Arrow shows the direction of motion.

CHAPTER 3

A ROBOPHYSICAL MODEL FOR QUADRIFLAGELLATE PROPULSION

3.1 Summary

Locomotion at the microscale is remarkably sophisticated. Microorganisms have evolved diverse strategies to move within highly viscous environments, using deformable, propulsion-generating appendages such as cilia and flagella to drive helical or undulatory motion. In single-celled algae, these appendages can be arranged in different ways around an approximately 10 μm long cell body, and coordinated in distinct temporal patterns. Inspired by the observation that some quadriflagellates (bearing four flagella) have a similar morphology and flagellar beat pattern, yet swim at different speeds, this study seeks to determine whether variations in swimming performance could arise solely from differences in swimming gait. Robotics approaches are particularly suited to such investigations, where the phase relationships between appendages can be readily manipulated. Here, we developed autonomous, algae-inspired robophysical models that can self-propel in a viscous fluid. These macroscopic robots (length and width = 8.5 cm, height = 2 cm) have four independently actuated 'flagella' (length = 13 cm) that oscillate under low-Reynolds number conditions (Re $\sim \mathcal{O}(10^{-1})$). We tested the swimming performance of these robot models with appendages arranged two distinct configurations, and coordinated in three distinct gaits. The gaits, namely the pronk, the trot, and the gallop, correspond to gaits adopted by distinct microalgal species. When the appendages are inserted perpendicularly around a central 'body', the robot achieved a net performance of $0.15 - 0.63$ body lengths per gait

This chapter's contents are adapted from a first authored paper published 2021 in Bioinspiration and Biomimetics [43] by Kelimar Diaz, Tommie L. Robinson, Yasemin Ozkan-Aydin, Enes Aydin, Daniel I. Goldman, and Kirsty Y. Wan

cycle, with the trot gait being the fastest. Robotic swimming performance was found to be comparable to that of the algal microswimmers across all gaits. By creating a minimal robot that can successfully reproduce cilia-inspired drag-based swimming, our work paves the way for the design of next-generation devices that have the capacity to autonomously navigate aqueous environments.

3.2 Introduction

The ability to generate self-propulsion is a distinguishing feature of most living organisms. In the macroscopic world, locomotion is typically associated with inertia [122], though recent work has revealed the dominance of friction over inertia in terrestrial locomotion [123, 40]. On the other hand, locomotion at the microscopic scale is subject to low Reynolds number physics, and cannot take advantage of inertial coasting. Without motility, a bacterium can only coast a minuscule distance an order of magnitude below the Ångström scale [72]. Over billions of years of evolution, microorganisms have become adept at swimming, evolving distinct mechanisms for powering and maintaining self-propulsion through a fluid, often achieving speeds of several tens of cell-body lengths per second. This active motility confers a significant survival advantage, allowing microbes to navigate freely towards regions or locations where there are abundant nutrients or resources [124]. Depending on the arrangement (relative to the cell body) and number of locomotor appendages (i.e., number of flagella or cilia), single cells can execute swimming gaits that are surprisingly reminiscent of animals. For example, the model biflagellate alga *Chlamydomonas* actuates two flagella in a breaststroke [125], while quadriflagellate algae (single cells with four-flagella) exhibit distinctive quadrupedal gaits such as the trot or the gallop [26] (Figure 3.1A,B).

In recent years, advances have been made in understanding the biomechanics of microswimming. Here, the Reynolds number is small, $Re = UL/\nu$, where L is a typical length scale of the swimmer, U a typical velocity scale, and ν is the kinematic viscosity

of the fluid. Equally important is the oscillatory Reynolds number $Re^{\text{osc}} = L^2\omega/\nu$ [126], where ω the typical stroke frequency (which sets a tip velocity of ωL). When both are small, flows are then governed by the Stokes equations: $0 = \nabla p - \mu\nabla^2\mathbf{v}$ and $\nabla \cdot \mathbf{v} = 0$ (where $\mathbf{v}$ and p are the flow and pressure fields), and have no explicit time-dependence. Microorganisms are able to break time-reversal symmetry using non-reciprocal strokes or body deformations, often involving whip-like appendages called cilia and flagella [72, 127]. While bacteria make use of rigid helical flagella [128], eukaryotes actuate motile cilia which produce asymmetric waves of propulsion [129, 130]. For a microorganism oscillating a $10\ \mu m$ flagellum at 50 Hz, $Re \sim 10^{-3}$, and $Re^{\text{osc}} \sim 10^{-2}$. One further asymmetry is required for forward propulsion [75]: In living cells this can be achieved by shape asymmetry, which is ensured by the slender aspect ratio of all cilia and flagella (about 100). Rigid colloidal particles can also self-propel by diffusiophoresis without shape changes by generating concentrating gradients [131]. A rod sweeping through a fluid in the perpendicular (tangential) direction of the axis of the rod experiences approximately twice the drag compared to when it is moved in the parallel (normal) direction [132]. Organisms across all scales have been found to exploit this basic anisotropy for locomotion [40, 2, 47].

Despite the use of cilia and flagella as a common propulsion mechanism, the microscale locomotion strategies of microorganisms have diversified significantly across different phyla [44]. It is not well-understood why different gaits exist nor how they are coordinated. For centuries, locomotor gaits have been studied in the context of terrestrial animals, where the sequences of relative movement sustained by subsets of limbs leads to propulsion. In vertebrates, gaits are thought to be generated by central pattern generators (CPGs) [133]. But how can orderly, deterministic appendage coordination occur in single cells in the absence of nervous control [44, 4]? Recent theoretical and experimental work have show that dynamic gait selection, at least in flagellates, appears to be an active and species-dependent process driven by intracellular and mechanical coupling [4, 134]. Notably, distinct quadriflagellates can self-propel at different speeds despite an apparently

identical arrangement of flagella around the cell body [26, 135]. Since the ancestral form of the green algal lineage may have have been a unicellular organisms with four flagella [136], there is much incentive to understand the precise mechanisms of appendage coordination in such systems.

In the quest to address these open questions of movement control, extant organisms can provide only a limited parameter space of possibilities in terms of size, shape, beat frequency, and others. This often makes it challenging to investigate certain configurations or physical regimes. Theoretical and computational approaches have been instrumental in shaping our understanding of active propulsion [132, 137], but these can be computationally expensive or reliant on simplifying assumptions. Meanwhile robophysical modelling has emerged as a powerful and versatile technique for elucidating organismal behaviour by engineering customised configurations that can be easily tested in a controlled laboratory setting [138, 88, 139]. The revolution in robophysical modelling has been driven in part by low-cost electronics (motors, microcontrollers), and increasingly accessible control technologies that can complement theoretical modelling to provide real biological insights [88, 140]. However, trying to model cell movement is a significant conceptual challenge when working *at the microscale*. Even though increasingly controllable micro- and nano- devices have been fabricated to mimic the locomotive behaviours of biological swimmers [141, 142], these are driven by external magnetic, electric, or chemical fields. Magnetic fields are often unable to deliver fine spatial control, required to independently actuate individual artificial cilia in a given array or network though there have been some recent progress in device miniturisation [143]. As theoretical representations of flagellates, artificial swimmers and microrobots, minimal models based on a small number of moving components (e.g., beads, rods) have yielded significant insights into the effect of gait coordination on self-propulsion and motility [144, 145, 146, 147]. Meanwhile, more realistic models of swimming cells that account for filament elasticity and shape have also been developed for single or arrays of cilia [148, 149, 150], but these approaches have not yet been applied to

study the influence of swimming *gaits* in freely-moving multiflagellates.

The intrinsic limits of device manufacturing at small scales makes 'microrobots' unsuitable to as realistic models of cell motility. To understand the influence of gait on self-propulsion at low-Reynolds number, our goal is to build a dynamically-scaled, self-powered, robophysical model, where the movement of individual locomotor appendages can be independently prescribed and controlled. In contrast to traditional microrobots, the larger size allows us to explore and take advantage of increasingly sophisticated electronics and control architectures [151, 152]. We can readily program these "roboflagellates" to execute specific swimming gaits, making them well suited for testing theories of bio-inspired and autonomous locomotion at a low-Reynolds number regime. This chapter is organised as follows: We first identified and measured the relative swimming performance of three closely-related species of quadriflagellate algae that exhibit near-identical morphology but distinct swimming speeds. Next we built a O(10)cm robot that can self-propel in a highly-viscous fluid when modeling the asymmetric beat pattern of the algal flagella, capturing the low-Reynolds number kinematics. By arranging the robotic flagella in one of two possible configurations (parallel or perpendicular) relative to a central "cell body", we imposed and tested three distinct flagellar actuation patterns (gaits) that occur in the biological quadriflagellates, namely the pronk, the trot, and the gallop. In each case, we compared the hydrodynamic swimming performance of the robot to that of the corresponding algal species. Finally, we discuss the relevance of these results for understanding how functional differences in swimming performance may arise from morphologically similar structures, and highlight the implications of this from an eco-evolutionary perspective.

3.3 Materials and Methods

3.3.1 Culturing and imaging of algae

Three species of algae (*Pyramimonas parkeae*, *Pyramimonas tetrarhynchus* and *Carteria crucifera*) were cultured axenically (i.e., independent cultures, without other species)

according to previously published protocols [26, 4]. Free-swimming individuals were tracked in open microfluidic chambers using a high-speed camera (Phantom Vision Research). Brightfield imaging was conducted with 40x or 60x objectives using standard inverted microscopes (Leica DMi8 and Nikon T2000-U) under white light illumination. Free-swimming trajectories were obtained from high-speed videos in which single cells crossed the focal plane, with the use of the open source software TrackMate (Fiji) [153]. Ten cells per species were used to determine the performance of each swimming gait. Tracks in which cells performed transient gaits, tumbles, or changed directions were not used in this analysis. The body length of each cell was measured along the long axis (anterior-posterior) of the organism. An average body length of 13.95 ± 2.05 μm, 12.54 ± 0.65 μm, and 12.82 ± 0.72 μm was found for *P. parkeae*, *P. tetrarhynchus* and *Car. crucifera*, respectively.

3.3.2 Quadriflagellate robophysical model

We designed a dynamically-scaled robot to ensure that the robophysical model is self-powered and did not require external fields - all controllers and servos are fully self-contained (Figure 3.1C). We performed robot experiments in a highly viscous fluid (mineral oil, McMaster, 1000 cSt, product no. 1401K75) to approximate the low Reynolds number regime experienced by the algae (Figure 3.1C). A subset of trials were conducted in glycerin (vegetable glycerin, Blue Water Chem Group, product no. B07FQWDTH7) of comparable viscosity to the mineral oil, to enable better visualisation and tracking of appendage movement. The robot consisted of a 3D printed body (length and width = 8.5 cm, height = 2 cm, additional CAD details in Figure 3.13) attached to four flagella that were independently actuated by waterproof servo motors (Savox, product no. SW0250MG, max torque of 3.5 kg/0.34 Nm, operating at 4.8 V). Each appendage was oriented such that the stroke lies in the plane perpendicular to the body (Figure 3.1D). Foam (FOAMULAR Insulating Sheathing (IS) XPS Insulation) was attached on the robot body to achieve neutral buoyancy

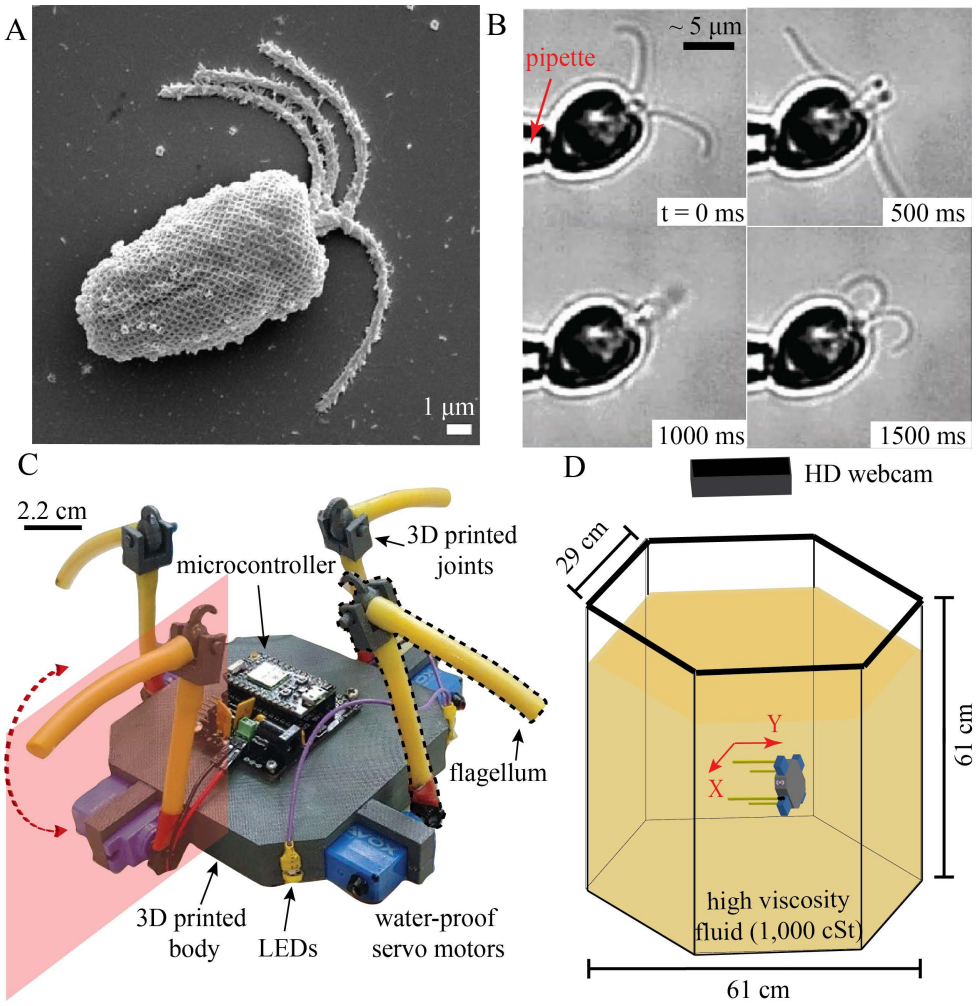

Figure 3.1: **Design and fabrication of a dynamically-scaled robophysical model of a microswimmer with four flagella.** (A) Scanning electron microscope (SEM) image of *Pyramimonas gelidicola* [154]. (B) Snapshots of *Pyramimonas parkeae* held by a pipette. (C) Robophysical model of quadriflagellate algae. (D) Experimental set-up. The arena is a hexagonal tank filled with mineral oil or glycerin of high viscosity, to approximate the low Reynolds number regime experienced by the algae.

and allow it to swim untethered. Commanded appendage positions were achieved using a microcontroller (Photon, Particle, part ID: PHOTONH) that allowed actuation of the robot with the use of Wi-Fi. The microcontroller and each motor were connected via a IOT Servo Shield (Actuonix, part ID: IOT-SHIELD-PHOTON), a circuit board specific to our microcontroller. Four LEDs were placed on the 3D printed body to facilitate tracking. The robot was powered with three lithium ion polymer batteries (3.7 V, 2500 mAh), each powering directly the microcontroller, the motors, and any attached LEDs. With this microcontroller,

the robot was able to achieve self-propulsion over approximately one hour.

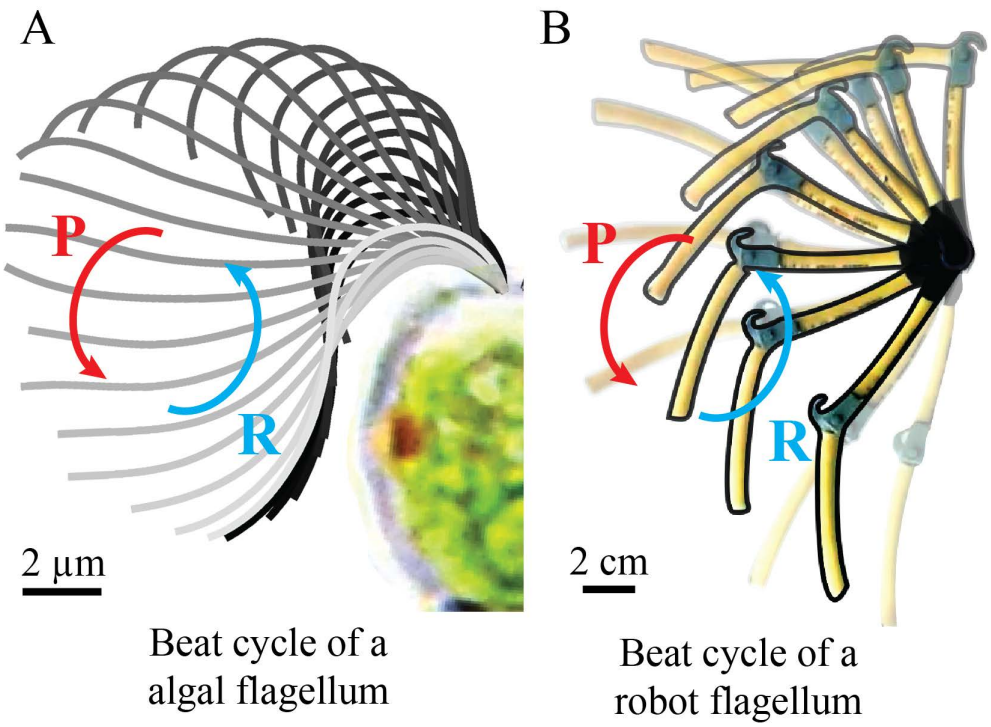

Figure 3.2: **Breaking time-reversal symmetry with a hinged two-link bio-inspired flagellum.** One beat cycle of an (A) algal flagellum compared to a (B) robot flagellum. P: power stroke, R: recovery stroke. Each robot flagellum segment has a length of 6.5 cm and diameter of 3.1 mm. Asymmetric beat patterns are achieved via a 3D printed joint. The movement patterns of the algal flagellum were measured in water. Robot beat pattern was visualized in a high-viscosity fluid (glycerin).

Inspired by the flagellar beating waveform of the organisms, we implemented a simple two-link robotic flagellum connected via a 3D printed joint (Figure 3.2). Each flagella (length = 6.5 cm, diameter = 3.1 mm, polypropylene-based thermoplastic elastomer (TPE)) could bend passively to break time-reversal symmetry, without the need to actively prescribe the beating shape over a beat cycle (Figure 3.1C). No external control sensing or environmental awareness was implemented, our robot was completely open loop. Each gait maintained a constant phase difference between adjacent flagella set by prescribed joint angles of the proximal segment (where the motor and flagella connected) (Figure 3.3). Each gait was uploaded to the microcontroller via Wi-Fi, allowing the controllers to actuate the motors. Unless otherwise specified, all gaits were prescribed with a flagellar beating fre-

quency of 0.14 Hz.

For the movement of the robot in mineral oil (kinematic viscosity $\mu/\rho = 10$ cm^2/s), the Reynolds number for the body (Re) was 0.14 ($L = 3.8$ cm, $U = 0.38$ cm/s), while the oscillatory Reynolds number Re^{osc} was 0.20 ($L = 3.8$ cm, $\omega = 0.14$ Hz). For the experiments conducted in glycerin (kinematic viscosity $\mu/\rho = 11.83$ cm^2/s), $Re = 0.27$ ($L = 6.89$ cm, $U = 0.40$ cm/s), and $Re^{\text{osc}} = 0.55$ ($L = 6.89$ cm, $\omega = 0.14$ Hz).

We imposed three distinct gaits to the robot similar to those observed in quadriflagellate algae – the pronk, the trot, and the gallop. The different coordination patterns were achieved by prescribing the phase differences between adjacent flagella. The resulting gait sequences were confirmed for an immobilised robot body, where the distance from each flagellum tip to the cell body was used as proxy for phase. In the pronk gait, all four appendages move simultaneously, without any phase difference ($\varphi = 0°$) between adjacent flagella (Figure 3.3A). The trot gait is defined by alternating pairs of flagella each of which is generating a pattern analogous to a breaststroke, with a phase difference of half a gait cycle (φ=180°) (Figure 3.3B). In the gallop gait, each appendage moves with a phase difference of a quarter-gait cycle relative to its neighbour (Figure 3.3C). The directionality (clockwise or counter-clockwise) of the gallop gait is determined by the phase difference (φ) between the first appendage (m_1) and an adjacent appendage (m_2 or m_4). We tested the gallop gait in both a clockwise (φ=90°between m_1 and m_2) and counter-clockwise (φ=180°between m_1 and m_2) direction. We imposed a clockwise and counter-clockwise direction to investigate how chirality can affect the performance of the gallop gait.

Due to the opacity of the oil, we attached lightweight LEDs to the robot's body to facilitate motion tracking (Figure 3.14). All LEDs were digitized using custom MATLAB algorithms. We approximated the center of geometry of the robot by averaging the position of the LEDs over time. Then, we used the tracks to determine the distance traversed by the robot in units of body lengths per beat cycle. A total of 9 trials were taken per gait, for each robot configuration. A trial was terminated either when the robot contacted a boundary,

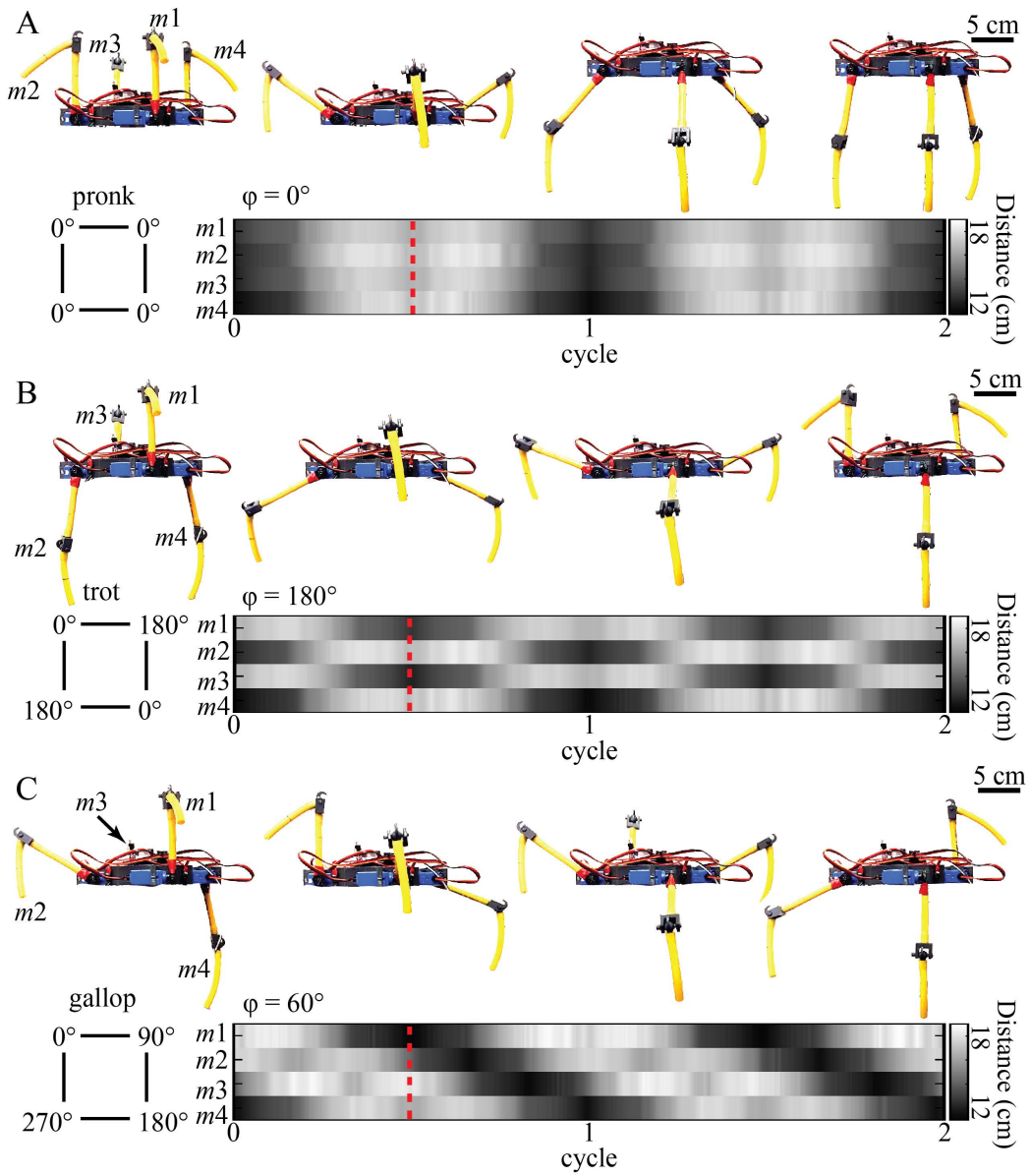

Figure 3.3: **Quadriflagellate gaits prescribed to the robot.** Distance from the center of geometry of the robot to the tip of each flagella was used as a proxy for the phase between adjacent flagella, labelled $m1$-4. (A) The pronk gait: zero phase difference (φ=0°) between adjacent flagella. (B) The trot gait: alternating pairs of flagella with a phase difference of half a gait cycle (φ=180°). (C) The gallop gait: adjacent flagella with a phase difference of a quarter of a gait cycle (φ=90°). Snapshots of the robot showing the flagella configurations during each gait over half a gait cycle. The dashed red line delineates half a gait cycle from the start of the recording. [Note to visualise the gaits fully the robot was not placed in fluid.]

or if the LEDs were no longer visible as the robot slowly drifted downwards (i.e., sunk) over time; this is due to the 3D material trapping fluid and increasing in mass. Thus, each

trial comprised $6 - 10$ cycles per gait. The dynamics of the flagella were not observed in the mineral oil due to the opacity of the fluid. Thus, in subsequent experiments, we used glycerin as an alternative high viscosity fluid to visualize and track movement of the flagella during active swimming. However, because glycerin is not a dielectric fluid (i.e., glycerin conducts electricity), wi-fi connectivity was interrupted and the circuits were negatively affected. To resolve this, we substituted our microcontroller (Pro Trinket, Adafruit, product ID: 2000) and sealed the circuits with a gasket and a 3D printed cap. In glycerin, flagella kinematics were digitized using DLTdv8 [155].

3.4 Results and Discussion

3.4.1 Swimming performance dependence on gait for the algae

We identified the quadriflagellates as an ideal study group owing to their morphological diversity (in size, shape, and aspect-ratio), and abundance in marine, terrestrial, freshwater habitats. A key trait among quadriflagellates is the arrangement of flagella around the anterior of the cell [136, 156]. Here, we take advantage of this diversity to compare the swimming behaviour of three species (*Pyramimonas tetrarhynchus*, *Pyramimonas parkeae*, and *Carteria crucifera*) that employ three distinct gaits - respectively the pronk, the trot, and the gallop. We conjecture that inter-species differences in quadriflagellate swimming performance can be attributed to differences in gait alone - where the same basic stroke is applied to ensembles of appendages but according to distinct phase relationships.

Two of these algae belong to the genus *Pyramimonas*, a Prasinophyte algae belonging to an early diverging class which is thought to have given rise to the core Chlorophyte algae, comprising species with two, four, eight, or up to sixteen flagella [157, 26]. Four flagella of identical length and beat pattern emerge from an deep anterior groove or pit in the cell body. The third species, *Car. crucifera*, is a Volvocalean flagellate that is closely related to the model biflagellate *Chlamydomonas*. Despite this phylogenetic divergence, all three species are similar in body size and flagellar morphology, and appear obovoid (egg-shaped)

to cordate (heart-shaped) in side profile [158, 159].

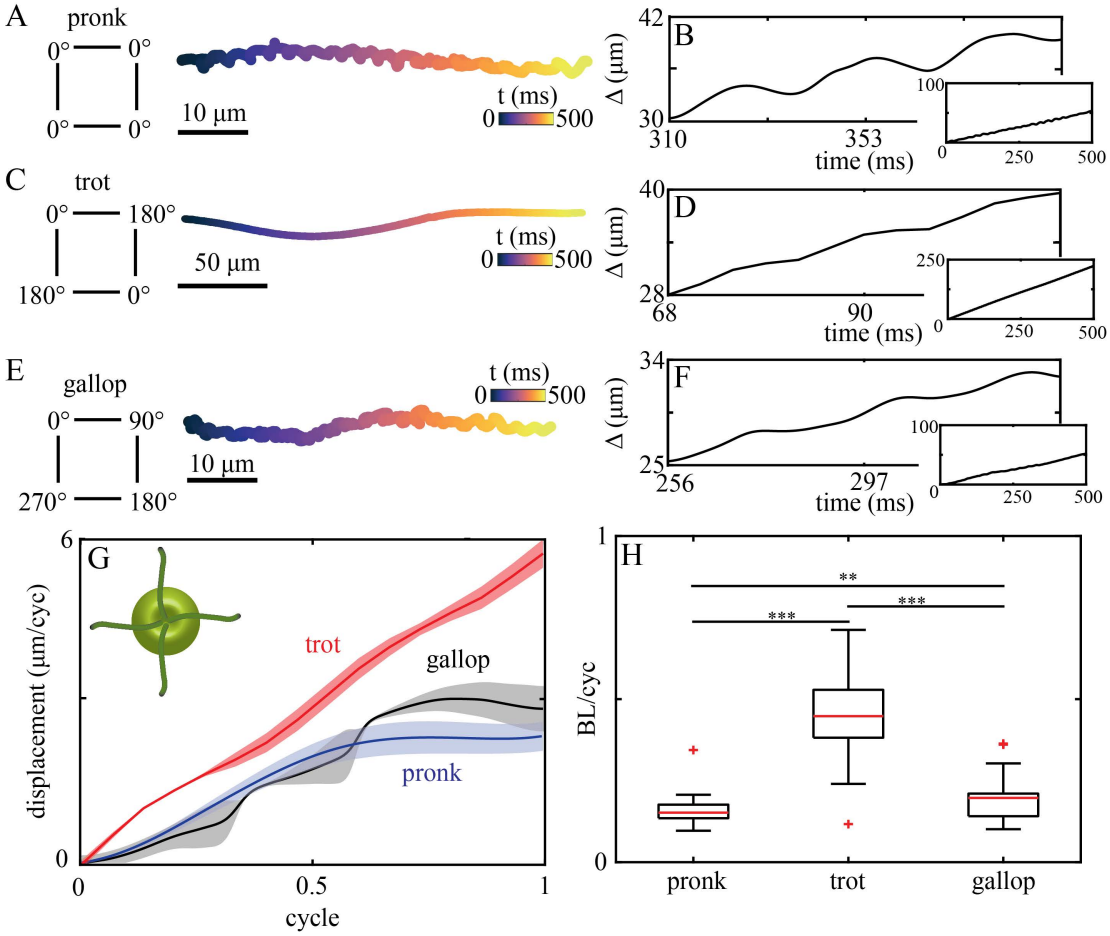

Figure 3.4: **Gaits, kinematics, and hydrodynamic performance of quadriflagellate algae.** All experiments were conducted in culture media - which had the same viscosity as water. For the pronking gait of *Pyramimonas tetrarhynchus*: (A) a sample (cell-centroid) trajectory colored by time, and (B) forward displacement over time for three cycles. Inset shows forward displacement over time of trajectory. For the trotting gait of *Pyramimonas parkeae*: (C) a sample (cell-centroid) trajectory colored by time, and (D) forward displacement over time for three cycles. Inset shows forward displacement over time of trajectory. For the galloping gait of *Carteria crucifera*: (E) a sample (cell-centroid) trajectory colored by time, and (F) forward displacement over time for three cycles. Inset shows forward displacement over time of trajectory. (G) Mean displacement within a gait cycle for all gaits - the pronk (blue line), trot (red line), and gallop (black line). Shaded areas correspond to the standard deviation. (H) Median displacement computed in terms of body lengths per cycle, for each gait. Red crosses correspond to outliers. Asterisks correspond to statistical significance of differences observed. Differences are significant at $p \leq 0.01$, $p \leq 0.001$ for two and three asterisks, respectively.

In all three cases, cells swim smoothly flagella-first (known as puller-type) at speeds

of $\mathcal{O}(100)$ μm$/s$. Translational motion is coupled to an axial rotation (i.e., rotation of the cell body) to produce swimming along helical trajectories [160]. Abrupt gait transitions can occur either spontaneously or when triggered by mechanical contact, during which the flagella are directed to the front of the cell in a so-called shock-response [28]. Cells can also reversibly stop and start swimming, when all or some of the flagella transiently cease to beat [4].

In all cases, free-swimming trajectories are superhelical, where small-scale swirls at the scale of single-cells are produced by the periodic flagellar oscillations. Three representative tracks, projected onto the focal plane, are shown in Figure 3.4 (A,C,E). Using these tracks, we estimated for each of the three gaits the displacement per cycle, including the cumulative displacement as a function of phase during the beat cycle (Figure 3.4G) as well as the mean forward progress per complete cycle (Figure 3.4H). Measured swimming speeds were 126$\pm$24, 408$\pm$46, and 127$\pm$25 $\mu m/s$ for the pronk, the trot, and the gallop, respectively. Our results show that the trot gait is the fastest gait in the microalgae. Meanwhile the pronk and gallop gaits lead to comparable swimming speeds.

3.4.2 Time-reversal symmetry breaking

We first confirmed that our robophysical model swims in a low-Reynolds number regime by attaching 3D-printed rigid (unhinged, length = 13 cm) flagella to the body, and actuating these with both a time-symmetric as well as a time-asymmetric stroke pattern. To create a time-asymmetric stroke, we increased the beating frequency of the recovery stroke. Due to the rotational position based control of the motors, changes in the frequency were achieved by changing the rate at which joint angles were prescribed. The recovery stroke frequency was varied from 0.07 Hz to 0.21 Hz. As expected, reciprocal strokes produced negligible net swimming in both cases. For a time-symmetric pattern, the net displacement in the direction of movement after one complete cycle was 0.38$\pm$0.40 cm (0.05$\pm$0.05 BL) using the pronk gait (Figure 3.5A). When the stroke frequency was increased, and consequently

Reynolds number, the displacement of the robot increased (Figure 3.5B). Thus, at higher beat frequencies the system can reach intermediate Reynolds numbers. Hereafter, we used a flagella beat frequency of 0.14 Hz to ensure inertial effects remained negligible.

With hinged instead of rigid flagella (Figure 3.2B), the robot became capable of net forward propulsion. Each gait cycle can be characterized by a power stroke during which the robot gains distance, and a recovery stroke during which it loses distance. We first set out to test the effect of the flagella 'waveform' (i.e., beating pattern) on swimming performance, expected to scale approximately with stroke amplitude [161, 162].

3.4.3 Effects of flagellar undulation patterns

We implemented two distinct flagellar undulation patterns - as defined by the maximal sweep range of the segments. For simplicity and to prevent axial rotation, we then reduced our quadriflagellate robot to a biflagellate robot, by removing one pair of flagella. The remaining pair of flagella were programmed to follow a breaststroke pattern (Figure 3.6A). We prescribed and compared the swimming performance for two different sets of motor angles: i) [0°, 180°], and ii) [45°, 135°] (Figure 3.6A inset). The motion of the distal segment (i.e., segment farthest from the body, connected by the hinge) always follows passively, with the hinge breaking time-reversal symmetry. We tracked the flagella 'waveform' in the two cases and calculated the angles generated by each flagellum segment over time (from motor to joint and from joint to tip, Figure 3.6A). The two sweep amplitudes produced two distinct gaits in the θ_1-θ_2 shape space (Figure 3.6B, Figure 3.15). A reduced sweep range results in a higher beat frequency ($\omega = 0.14$ Hz for motor angles of [0°, 180°], and $\omega = 0.41$ Hz for motor angles of [45°, 135°]). The rescaled displacement shows swimming performance increases with amplitude (Figure 3.6C). The larger-amplitude breaststroke achieves a greater displacement after each gait cycle. This suggests that non-inertial locomotion is dictated by the pattern of self-deformation [161]. In other words, movement is kinematic, and net displacement is determined largely by the gait and its associated low-dimensional

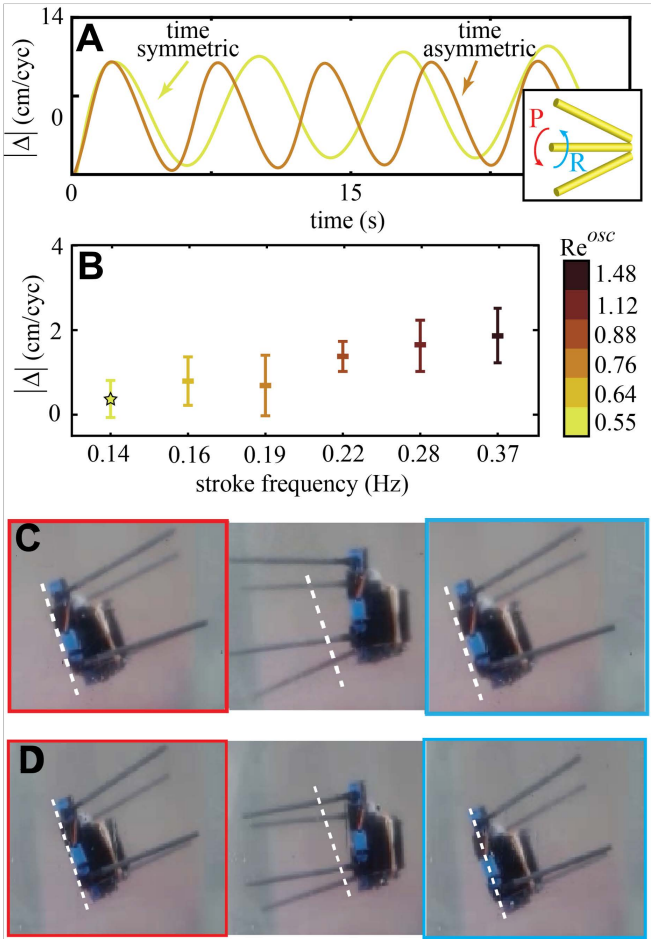

Figure 3.5: **Kinematic reversibility confirms low-Reynolds regime.** (A) Forward displacement traveled over time in glycerin with time-symmetric and time-asymmetric stroke pattern. Frequency of power and recovery stroke was 0.07 Hz for the time-symmetric stroke pattern. Frequency of the power and recovery stroke was 0.07 and 0.12 Hz, respectively. Negligible net displacement per cycle with time-symmetric and time-asymmetric stroke pattern. Inset shows one beat cycle of a single rigid flagellum moving back and forth. P: power stroke, R: recovery stroke. (B) Mean displacement as a function of stroke frequency. Star corresponds to frequency used for experiments shown for the rest of the experiments, unless otherwise stated. Error bars correspond to standard deviation. Snapshots of the robot during one gait cycle using rigid flagella for time-symmetric (C) and time-asymmetric (D) stroke pattern. Frequency of power and recovery stroke was 0.07 Hz for the time-symmetric stroke pattern. Frequency of the power and recovery stroke was 0.07 and 0.12 Hz, respectively. Left panel (outlined in red) shows the robot initiating a power stroke. Middle panel shows the robot during half a cycle. Right panel (outlined in blue) shows the end of the recovery stroke. Dashed lines highlight initial positions.

properties [163].

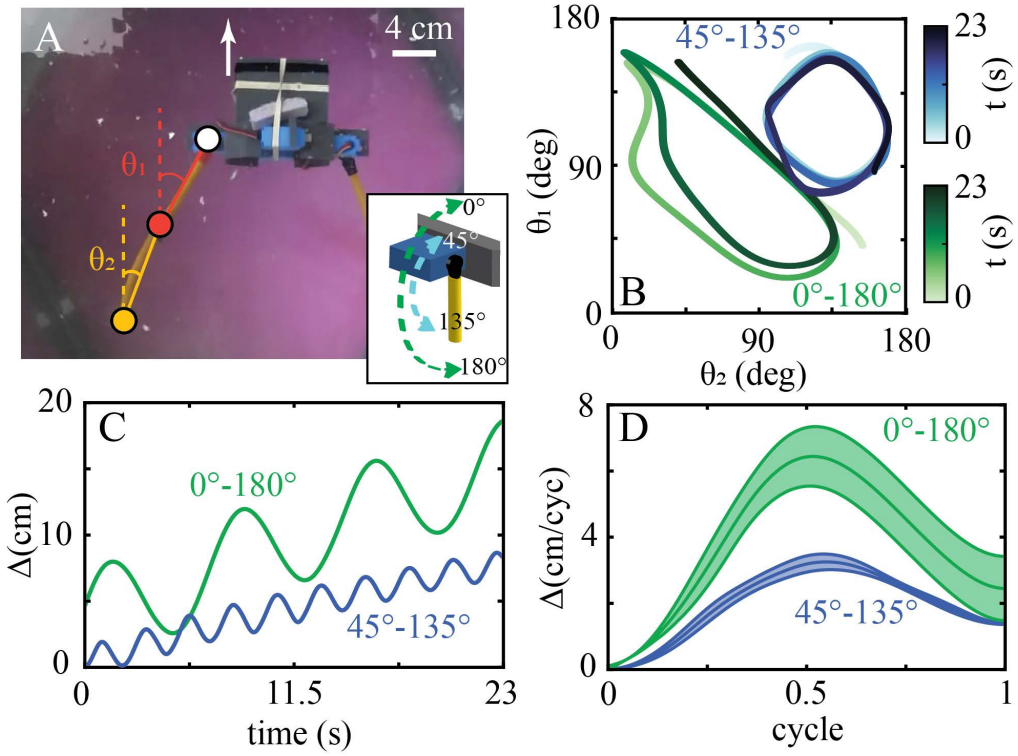

Figure 3.6: **Swimming performance increases with stroke amplitude.** (A) Quadriflagellate robot modified as a biflagellate robot, performing a breaststroke pattern with one pair of flagella. Angles θ_1 and θ_2 correspond to the angles generated by the flagella segment from the motor (white circle) to the joint (dark orange circle) and the segment from the joint (dark orange circle) to the tip (light orange circle). Inset shows variation of prescribed angles from 0°to 180°(green) and from 45°to 135°(blue). (B) θ_1 as a function of θ_2, colored by time, for the left flagellum. Green dots corresponds to angles from 0°to 180°. Blue dots corresponds to 45°to 135°. Note, right flagellum exhibits similar trajectories in the θ_1-θ_2 shape space (Figure 3.15). (C) Displacement traveled over time. Green line corresponds to angles from 0°to 180°. Blue line corresponds to 45°to 135°. (D) Mean displacement as a function of a gait cycle. Green line corresponds to angles from 0°to 180°. Blue line corresponds to 45°to 135°. Shaded areas correspond to the standard deviation. These experiments were conducted in glycerin with the alternative robot, to ensure the flagella beat pattern can be tracked.

3.4.4 Swimming performance dependence on gait and appendage placement

To test if swimming performance is dominated by gait or by other factors such as flagellar stiffness or waveform compliance, we prescribed the gaits exhibited by each algae species to our roboflagellate. We explored the effect of varying appendage phase coordination (gait) for two different configurations of four flagella, in which motors are positioned either

in a parallel or a perpendicular orientation with respect to the identical body.

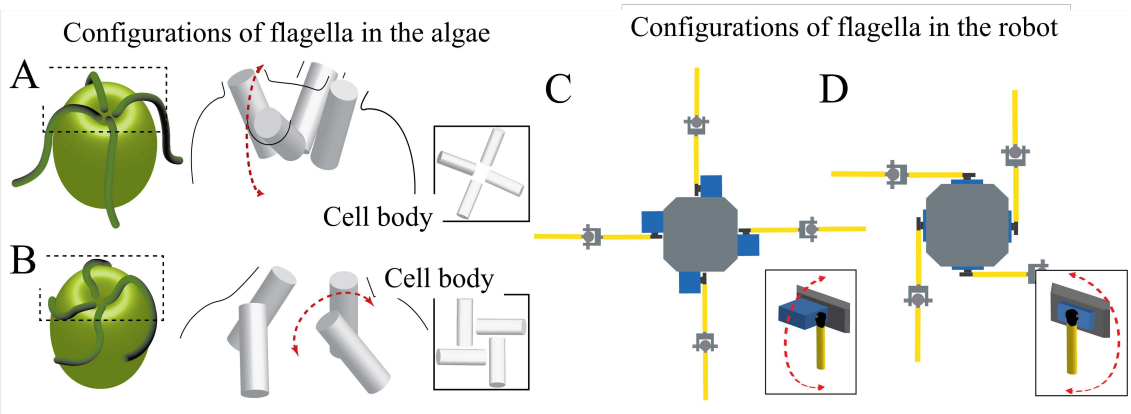

Figure 3.7: **Modelling appendage orientation.** (A) Illustration of two configurations of flagella and basal bodies that are found in quadriflagellates [156]. The flagella emerge from basal bodies (cylinders) that are oriented largely perpendicular (A), or parallel (B) to the cell body. Insets show anterior views (A: cruciate arrangement, B: turbine or windmill-like). Double-arrow indicates the approximate beat plane of the individual flagella. Similarly, two roboflagellate designs are presented. Motors and attached 'flagella' are oriented perpendicular (C) or parallel (D) to the central body. Again, double-arrow indicates oscillation plane.

These configurations were modeled on by naturally-occurring arrangements of basal bodies and flagella found in algal flagellates (Figure 3.7). All three species of algae studied here correspond to configuration A, in which the approximate plane of flagellar beating is perpendicular to the surface of the robot body. The main difference is that when viewed from the anterior of the cell, the four flagella are inserted with a clockwise twist or offset for *Carteria*, but an counter-clockwise offset for *Pyramimonas* [156]. Algal species reported to exhibit configuration B [156] were not available in culture and were not represented in the present study. Appendage coordination was prescribed in the robot by specifying the phase differences between flagella, to produce each of the three gaits: pronk, trot, or gallop, as previously described Figure 3.3.

For the perpendicular configuration, example trajectories as well as the cumulative forward displacement over time for each gait are shown in Figures Figure 3.8(B)-(C), (E)-(J). We also analyzed the detailed within-cycle dynamics for each gait. The pronk and both the clockwise (CW) gallop and counter-clockwise (CCW) gaits produce significant forward

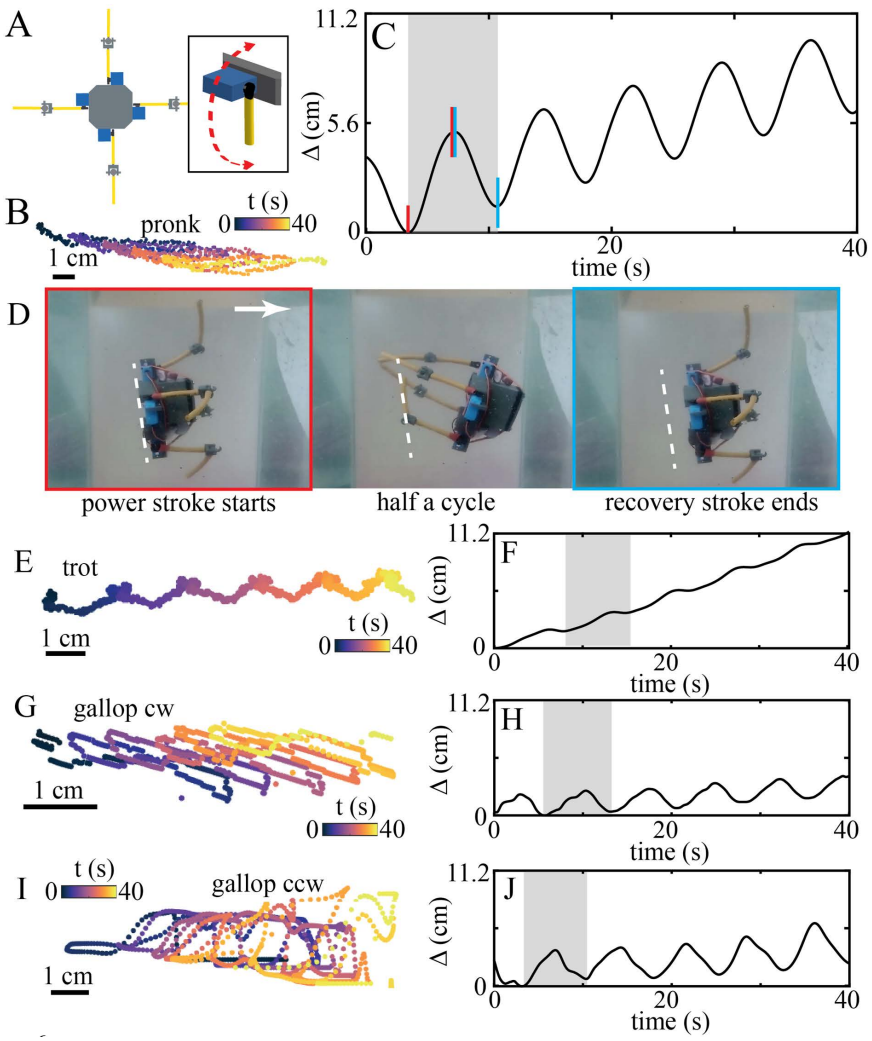

Figure 3.8: **Swimming gait kinematics for robot with flagella in the perpendicular orientation.** (A) Diagram of robot with motors oriented perpendicular to the body. Inset illustrates beating plane. For the pronk gait, (B) shows a sample trajectory of the robot, colored by time (5 cycles), and (C) the forward displacement traveled over time. For one gait cycle, red vertical lines highlight power stroke, and blue vertical lines highlight return stroke. (D) Snapshots of the robot during one cycle of the pronk gait. Left panel (outlined in red) shows the robot initiating a power stroke. Middle panel shows the robot during half a cycle. Right panel (outlined in blue) shows the robot completing the recovery stroke. Arrow shows swimming direction. Trajectory of the robot during the trot gait, colored by time (5 cycles) (E), and forward displacement traveled over time of the robot during the trot gait (F). Trajectory of the robot during the clockwise gallop gait, colored by time (5 cycles) (G), and forward displacement traveled over time of the robot during the clockwise gallop gait (H). Trajectory of the robot during the counter-clockwise gallop gait, colored by time (5 cycles) (I), and forward displacement traveled over time of the robot during the counter-clockwise gallop gait (J).

displacement during the power stroke (up to 5.7, 4, and 2 cm for the pronk, the CW gallop, and the CCW gallop, respectively, after half a gait cycle), but also produce a significant backward displacement during the recovery stroke, generating overall small displacement from cycle to cycle (0.33±0.04, 0.16±0.05, and 0.15±0.08 BL/cyc for the pronk, the CW gallop, and the CCW gallop respectively). On the other hand, while the trot does not achieve a greater displacement (only 2.3 cm after half a gait cycle) than the pronk or gallop during the power stroke, it loses a much smaller distance during the recovery stroke. This is because while one pair of flagella is moving towards the body and consequently producing backward motion, the other pair of flagella moves away from the body so as to resist this motion. This can also be observed in the trajectories, where the pronk and gallop gait shows backward motion, unlike the trot gait. Due to this, of the three gaits investigated the robot achieves the greatest hydrodynamic performance (0.6±0.08 BL/cyc) using the trot gait (Figure 3.9), just as in the algae.

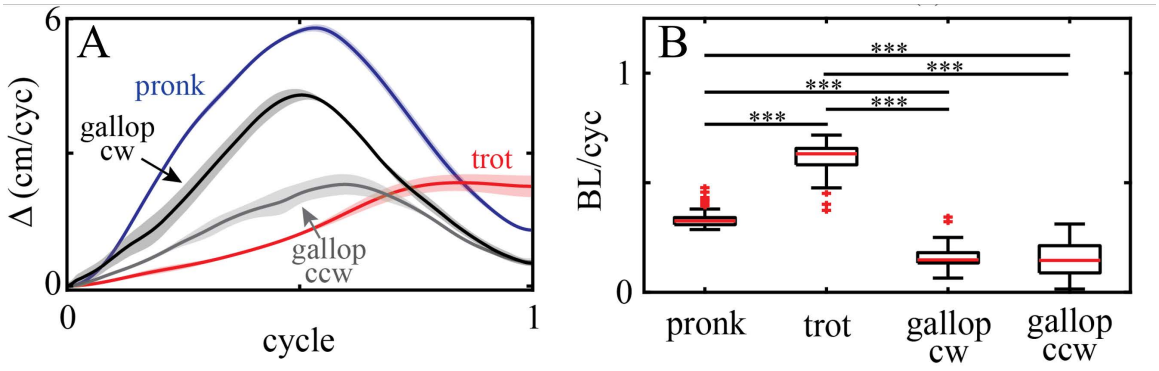

Figure 3.9: **Swimming performance for robot with flagella in the perpendicular orientation.**(A) Mean displacement over a gait cycle for all gaits - the pronk (blue line), trot (red line), clockwise gallop (black line), and counter-clockwise gallop (grey line). Shaded areas correspond to the standard deviation. (B) Body length per cycle as a function of swimming gait. Red crosses correspond to outliers. Asterisks correspond to statistical significance of differences observed. Differences are significant at $p \leq 0.001$ for three asterisks.

For the parallel configuration, example trajectories as well as the forward displacement over time for each gait can be seen in Figure 3.10(B)-(C), (E)-(J). Similar to the perpendicular configuration, the pronk gait allows the robot to gain a significant amount of distance

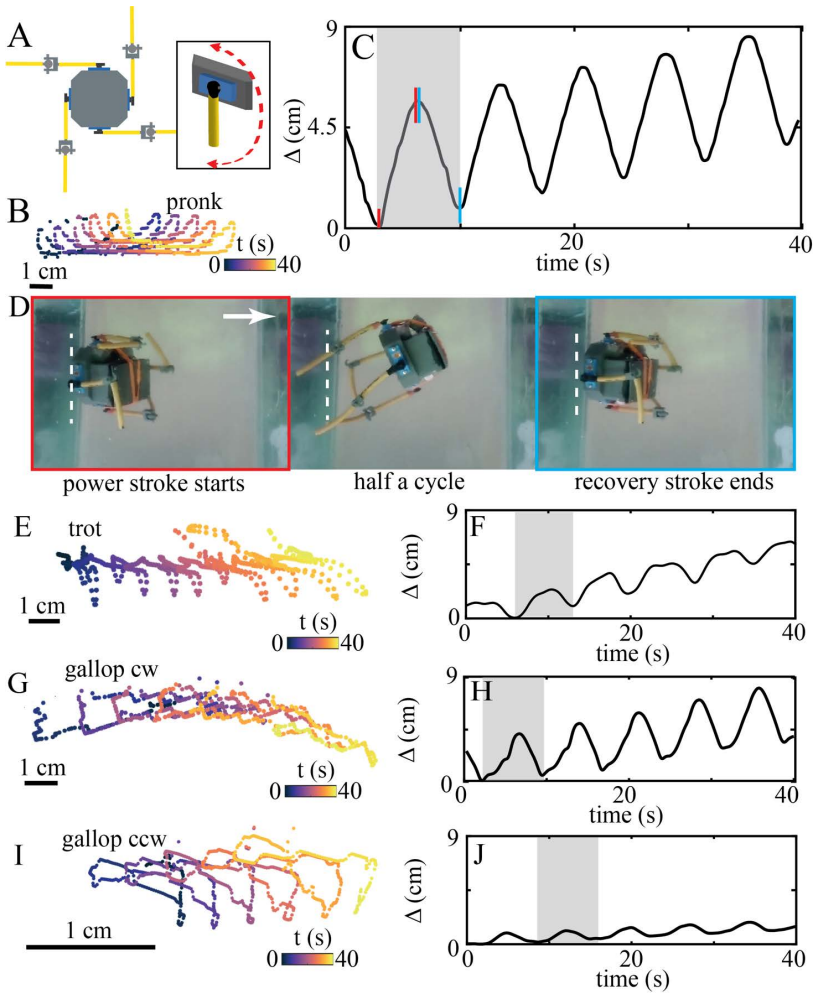

Figure 3.10: **Swimming gait kinematics for robot with flagella in the parallel orientation.** (A) Diagram of robot with motors oriented perpendicular to the body. Inset illustrates beating plane. For the pronk gait, (B) shows a sample trajectory of the robot, colored by time (5 cycles), and (C) the forward displacement traveled over time. For one gait cycle, red vertical lines highlight power stroke, and blue vertical lines highlight return stroke. (D) Snapshots of the robot during one cycle of the pronk gait. Left panel (outlined in red) shows the robot initiating a power stroke. Middle panel shows the robot during half a cycle. Right panel (outlined in blue) shows the robot completing the recovery stroke. Arrow shows swimming direction. Trajectory of the robot during the trot gait, colored by time (5 cycles) (E), and forward displacement traveled over time of the robot during the trot gait (F). Trajectory of the robot during the clockwise gallop gait, colored by time (5 cycles) (G), and forward displacement traveled over time of the robot during the clockwise gallop gait (H). Trajectory of the robot during the counter-clockwise gallop gait, colored by time (5 cycles) (I), and forward displacement traveled over time of the robot during the counter-clockwise gallop gait (J).

during the power stroke (up to 5 cm after half a gait cycle) but also lose a significant amount of distance during the recovery stroke, generating little net displacement from cycle to cycle. The CCW gallop gait displays a similar oscillatory pattern, however there is a discrepancy between the CCW and CW gallops (5.3 cm after half a gait cycle for the CW gallop, but only 1 cm for the CCW gallop). This is likely due to rotation-translation coupling in the second configuration (in which the flagella are inserted in the CCW sense), generating significant motion laterally and causing axial rotation of the robot. Similar to the perpendicular robot, the trot gait advances less during the power stroke (only 1.5 cm after half a gait cycle) and loses more distance during the recovery stroke, relative to the perpendicular configuration. The phasing between appendages in the trot gait again aids the robot in traversing a greater distance from cycle to cycle than the pronk (0.15±0.4 BL/cyc), and also greater than the average of the CW and CCW gallop gaits (0.15±0.9 BL/cyc). (We assume that by symmetry, this average between the two chiralities should cancel any rotational effects.) Thus, the trot remains a hydrodynamically effective gait for the parallel robot (0.26 ±0.08 BL/cyc) (Figure 3.11).

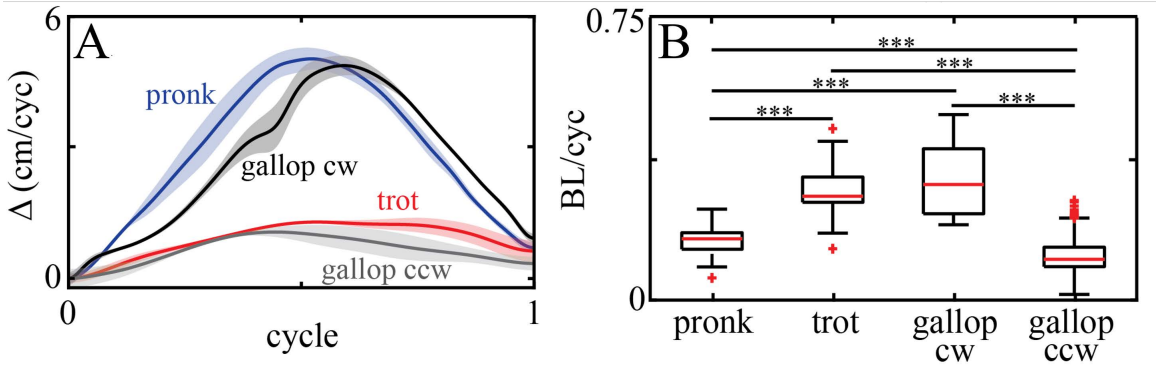

Figure 3.11: **Swimming performance for robot with flagella in the parallel orientation.** (A) Mean displacement over a gait cycle for all gaits - the pronk (blue line), trot (red line), clockwise gallop (black line), and counter-clockwise gallop (grey line). Shaded areas correspond to the standard deviation. (B) Body length per cycle as a function of swimming gait. Red crosses correspond to outliers. Asterisks correspond to statistical significance of differences observed. Differences are significant at $p \leq 0.001$ for three asterisks.

We conclude that the swimming performance of the roboflagellate is highly sensitive to

both gait and flagellar orientation (which defines the principal beat plane) of the flagella. It is possible that the organisms can access different regimes by controlling the 3D beat plane of their flagella, and that divergent flagellar placement evolved in different species as a result of different environmental selection pressures. In flagellates such as *Volvox*, nearby basal bodies (from which the flagella emerge) have rotated 90 degrees compared to the ancestral configuration found in the unicellular *Chlamydomonas*, likely to facilitate coordinated flagellar beating as an intact colony [26, 164].

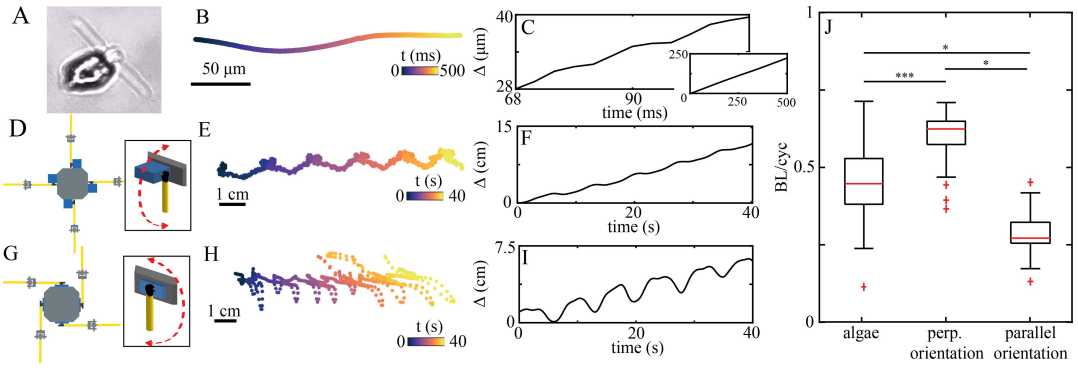

Figure 3.12: **Comparing the trot gait in the algae and robot.** (A) The alga *Pyramimonas parkeae* swimming using the trot gait. (B) Trajectory of *P. parkeae*, colored by time. (C) Forward displacement traveled over time by *P. parkeae*. (D) Diagram of robot with motors oriented perpendicular to the body. Inset illustrates beating plane. (E) Trajectory of the robot with perpendicular configuration using the trot gait, colored by time. (F) Forward displacement traveled over time of the robot with perpendicular configuration using the trot gait. (G) Diagram of robot with motors oriented parallel to the body. Inset illustrates beating plane. (H) Trajectory of the robot with parallel configuration using the trot gait, colored by time. (I) Forward displacement traveled over time of the robot with parallel configuration using the trot gait. (J) Body length per cycle for the trot gait for the algae, the perpendicular configuration, and the parallel configuration. Red crosses correspond to outliers. Asterisks correspond to statistical significance of differences observed. Differences are significant at $p \leq 0.05$, $p \leq 0.001$ for one and three asterisks, respectively.

3.4.5 Performance comparison to organisms

The above results show that a change in flagellar configuration can significantly change the performance of a given swimming gait. Focusing only on the trot, we note that this gait yielded the swimming performance for the algae and for the perpendicular robot, (Fig-

ure 3.12). Note that the speed of the algae trot gait is bounded above and below by that of the perpendicular and parallel robots.

In both robot configurations, significant axial rotation and lateral movement were observed in the free-swimming trajectories (Figure 3.12E,H) showing that our robophysical models do not swim as smoothly as their algal counterparts (Figure 3.12B). This is likely due to the discrepancy between the deformable stroke cycle of the continuous algal flagellum, compared to the angular movements of the two-link robot flagella. Additionally elastic elements in the algal cytoskeleton could play a role in gait stabilization by actively anchoring the flagella to the body [134, 165]. The cumulative displacement over time for a trotting cell and our perpendicular robot are comparable (Figure 3.12C,F). Meanwhile the parallel configuration displays larger amplitude oscillations in which a greater distance gained during each the power stroke is negated during the subsequent recovery stroke (Figure 3.12I). This is likely due to three-dimensional effects as mentioned above. In all, we find that the performance of the algae and both roboflagellate configurations are comparable in absolute terms, as measured in terms of body lengths per gait cycle. This agreement is surprising as we did not precisely match the dimensions of our robots to that of the algal cell, and unlike the algal flagella the robot 'flagella' were not capable of active bending [127] - being comprised only of rigid tubing and a plastic hinge.

3.5 Conclusion

Microscopic organisms have evolved to use many different ways of swimming at low-Reynolds number. Despite their size and simplicity, some single-celled algae can swim with different speeds using gaits analogous to animal gaits, that involve robust temporal ordering (i.e., relative phasing) of four flagella [4]. Here, we created the very first free-swimming robophysical model of these microswimmers to understand how motility and gait influences swimming. Dynamically-scaled robots enable scenarios to be tested that may not be possible in the live organism [166, 167, 168, 169]. Physical modelling

has previously provided insights into bacterial swimming [170], flagellar bundling [171], elastic tail propulsion [172], and metachronal actuation of in an on-rail robot with rigid appendages [173].

In contrast, our roboflagellate is self-powered and untethered (no external forces or torques) and was able to achieve fully-3D self-propulsion at low-Reynolds number. The robot recapitulated gait-dependent differences in swimming performance that we measured in the microalgae. These results reveal that phase coordination of propulsive appendages has a significant impact on hydrodynamic performance, while the orientation of appendages relative to the swimmer body also changes propulsion speed. In the perpendicular configuration that most closely models the three algal species studied here, the trot gait was consistently faster than either the pronk or gallop gait. We further predict that quadriflagellates with flagella oriented parallel to the cell body (configuration B) should swim more slowly than the three species studied here, for an equivalent gait. Moreover in all cases the displacement achieved by the robot in terms of body lengths per cycle was similar in absolute terms to the algae. Thus our dynamically-scaled robot is a good locomotor model of the biological microswimmer.

Our work raises open eco-evolutionary questions about the origins of the distinct motility patterns in the different quadriflagellate species. Distinct gaits likely reflect the relationship between an organism's metabolic requirements and its habitat. Freely-locomoting organisms at all scales, switch dynamically between multiple gaits [174, 175, 124]. While several *Pyramimonas* species exhibit sporadic bursts of rapid activity with extended inactive phases [28], *Volvocalean* algae including *Carteria* do not show such rest periods [4]. We conjecture that differences in gait provide an evolutionary advantage even at the microscale. Of the three algae studied here, two (*P. tetrarhynchus*, *Car. crucifera*) are freshwater species and one is a marine species (*P. parkeae*). *P. tetrarhynchus* was originally isolated from a peaty pool and cultured in a biphasic soil medium [158]. *Car. crucifera* is also a freshwater species that forms surface associations with leaves and other decaying

material. In contrast *P. parkeae* is most abundant in Arctic surface water and in tidal rock pools, where it can access sufficient sunlight for photosynthesis. *P. parkeae* also exhibits a unique diurnal vertical settling behaviour [176]. The latter behaviour, along with phototaxis, accentuates the need for vigorous swimming and hence the fast trot gait. Field data has shown that marine *Pyramimonas* routinely blooms in and around sea ice, where the unique polar environment (with extreme fluctuations in temperature, light, and salinity) is associated with a highly heterogeneous distribution of different *Pyramimonas* species even within the same water column [177]. The habitats of these algae may therefore be a key evolutionary driver leading to significant diversification of gait, even across species with apparently convergent morphology and size [178, 179]. Further experiments using both lab strains and wild isolates, controlling more precisely for culturing medium, are need to test this hypothesis. Our roboflagellate model can be used to explore mix-mode propulsion strategies and unsteady effects, such as nutrient dispersal.

We highlight two limitations of the current model. The first concerns boundary (see subsection 3.7.2) and finite-size effects, particularly due to fluid-structure interactions between moving appendages and the bounding tank, and between different parts of the robot. The presence of no-slip boundaries will alter the flow fields around a beating appendage, and change propulsion efficiency [180]. The chiral insertion of the robot flagella around the central body likely introduced an additional (unwanted) rotational movement. Second, the current robot relies on a two-link flagellum facilitated by a rigid 3D printed joint which has fewer degrees of freedom than the organisms (see subsection 3.7.1). The rigid joints have limited ability to resist torsion - which may be gait-dependent. Eukaryotic flagella and cilia can maintain their shape even when subject to significant hydrodynamic forces. They can also deform actively, to optimise propulsive force generation and efficacy [181, 182]. In future work we can resolve these limitations with more realistic roboflagellate designs, in parallel with hydrodynamic simulations and modelling to understand gait optimisation with truly deformable appendages.

In conclusion, we have presented a macroscopic robot capable of self-propulsion in a low-Reynolds number regime, and used this successfully to model aspects of microorganism swimming behaviour. This approach has potential for understanding different mechanisms of microscale swimming (e.g., gait selection, coordination and taxis [44]). From a technological perspective, these diverse propulsion strategies can provide unique, innovative solutions to the formidable challenge of navigating viscous fluids.

3.6 Contributions

This work was in collaboration with Prof. Kirsty Y. Wan, from the University of Exeter. The contributions for the project are detailed as follows:

Tommie L. Robinson designed the robots and performed experiments in mineral oil. Enes Aydin modified existing robots to develop robot for glycerin experiments. Kelimar Diaz assisted with experiments in mineral oil, performed experiments in glycerin, tracked the robots and the cells, and analyzed and processed the data. Kirsty Y. Wan performed algae swimming experiments. Kelimar Diaz, Tommie L. Robinson, Yasemin Ozkan-Aydin, Daniel I. Goldman, and Kirsty Y. Wan conceived the study and interpreted the results. Kelimar Diaz and Kirsty Y. Wan co-wrote the original manuscript [43]. Kirsty Y. Wan and Daniel I. Goldman supervised the project, provided comments on and modified the original manuscript [43].

3.7 Appendix

3.7.1 Correction on beat patterns

Upon using glycerin to observe beating patterns of the flagella, we observed that the flagellum oriented perpendicular to the tank bottom was generating beating patterns comparable to the other flagella (Figure 3.16A). This was due to buoyancy effects from the link material (surgical tubing). When we added masses (binder clips) to the misbehaving bottom

flagellum, the beat pattern became comparable to that of the other flagella(Figure 3.16B). Comparing the no-mass and added-mass scenarios, we found that the same patterns with respect to gait were reproduced in both parallel and perpendicular robots, with only a slight increase in speed across all gaits(Figure 3.17 and Figure 3.18). This is to be expected, as without the added mass the bottom flagellum would produce slightly less propulsion during the power stroke phase.

We compared our new results with the new robot in glycerine with our previous results in oil. For the perpendicular robot, the relative performances of the gaits were exactly the same as we had measured previously in Figure 3.9, with the trot gait still emerging as the fastest, followed by the pronk, then the gallop. For the parallel robot, there are some differences, e.g. with the gallop gait (Figure 3.11). This is due to the new robot having different dimensions (including an off-centered box in which electronics were sealed with a gasket), which introduces chirality which is an important factor for the gallop gait.

In summary, the relative performance of the gaits were not affected by the misbehaving bottom flagellum, proving that our design and original conclusions are robust. These comparisons also show that our robot can even be used to model the nuances of flagella-body interactions at low-Reynolds number, and the effect of body shape.

3.7.2 Boundary effects

While the tank was of a limited size, this was the largest tank we could obtain and reasonably house in the laboratory simultaneously. However, the boundary effects were consistent across all gaits (systematic effect), and consequently we do not expect they will change the conclusions presented here. In addition, we were careful to perform experiments with the robot moving approximately at the center of the tank. We note that that an object moving close to a solid boundary will encounter an increase in drag, this can be significant (up to 20% for a settling sphere) even when the size of the body is 1/100 that of the distance to the nearest wall. Yet, in all of our experiments the gait of the robot is imposed by the motors -

so when a higher drag is encountered the motors will simply produce more torque to deliver the same speed of flagellar movement. There is no environmental feedback (Figure 3.19). If we were to conduct future experiments in a much larger tank, we would be able to observe the movement of the robot over a greater number of beat cycles, and also study other aspects of 3 dimensional navigation, such as gait transitions.

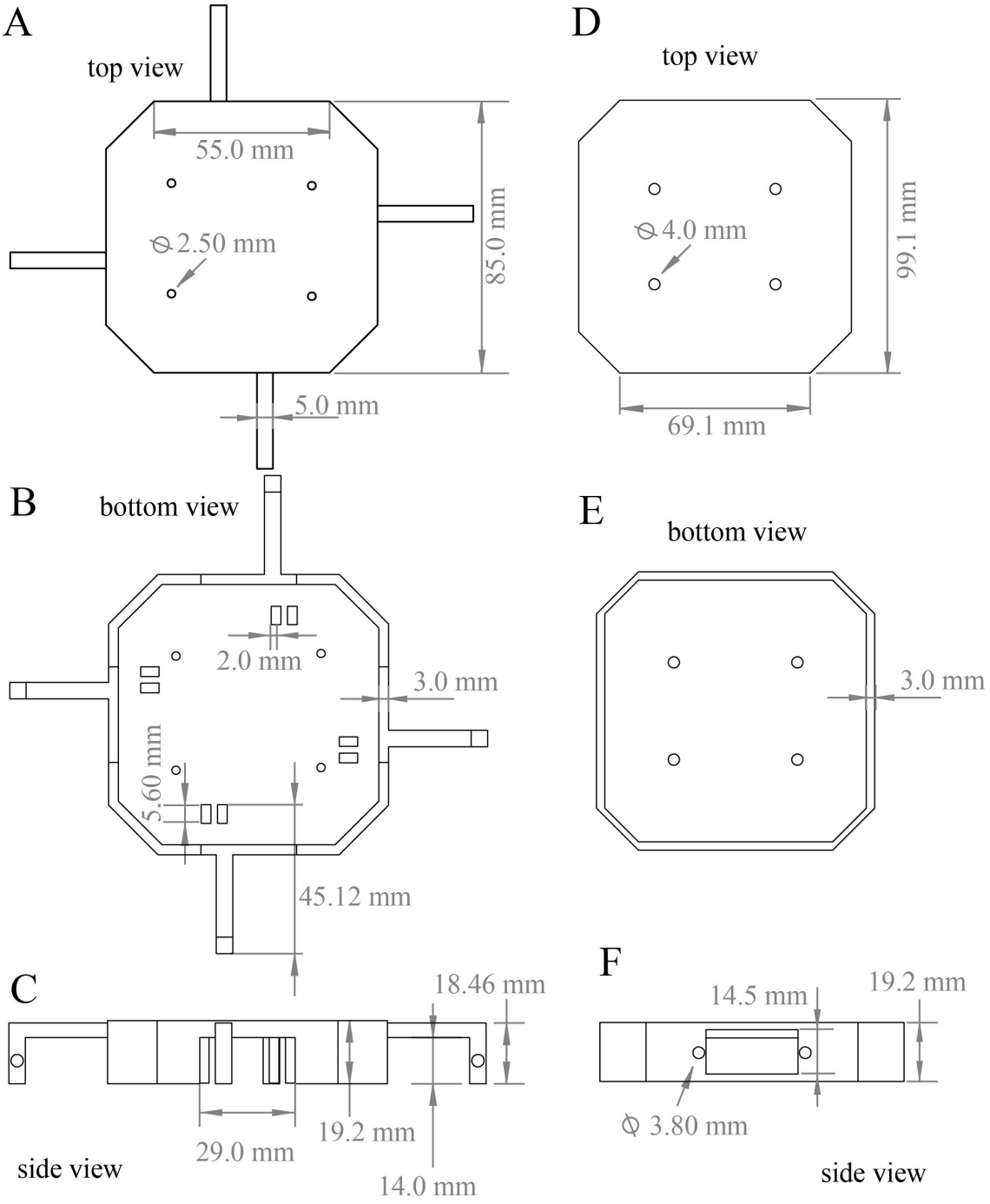

Figure 3.13: **CAD design of perpendicular and parallel robot.** CAD design for perpendicular robot 3D printed body from a top view (A), bottom view (B), and side view (C). CAD design for parallel robot 3D printed body from a top view (D), bottom view (E), and side view (F).

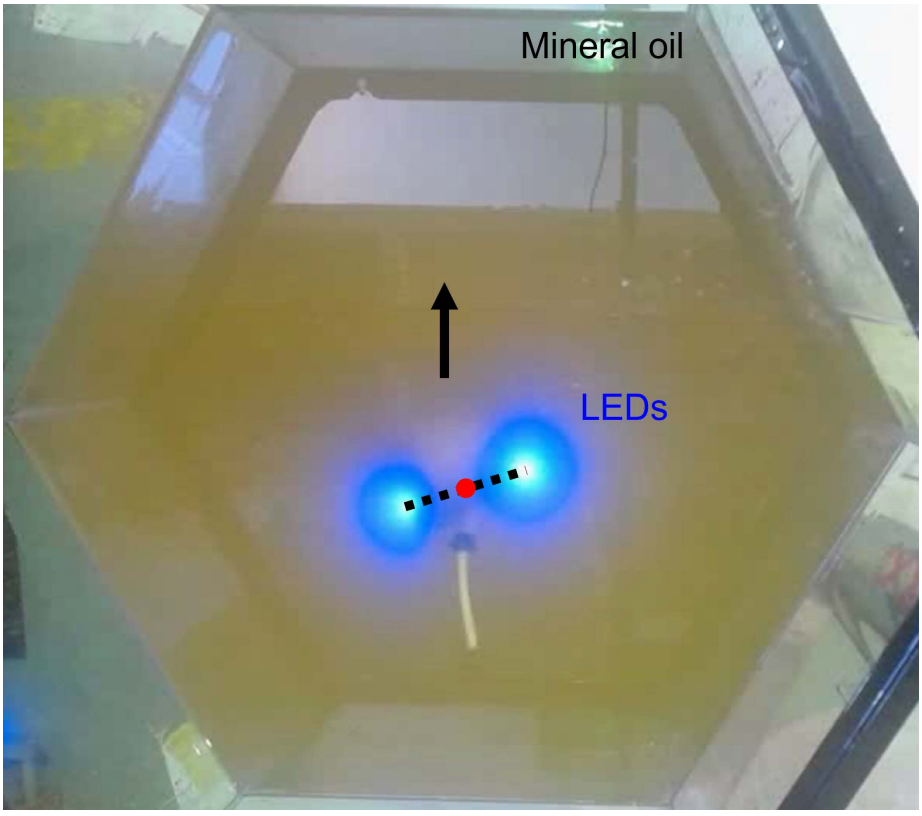

Figure 3.14: **Experiments conducted in mineral oil.** Snapshot of the perpendicular robophysical model swimming in mineral oil. Average position between LEDs was used as a proxy for robot body centroid due to the fluid opacity. Arrow shows the direction of motion.

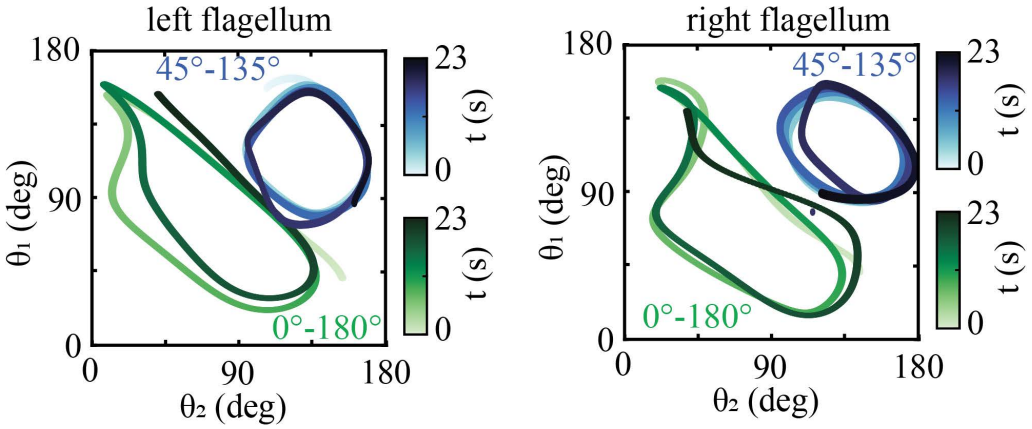

Figure 3.15: **Shape space of flagella for varying stroke amplitude**(A) θ_1 as a function of θ_2, colored by time for left flagellum. (B) θ_1 as a function of θ_2, colored by time for left flagellum. Green dots corresponds to angles from 0°to 180°. Blue dots corresponds to 45°to 135°.

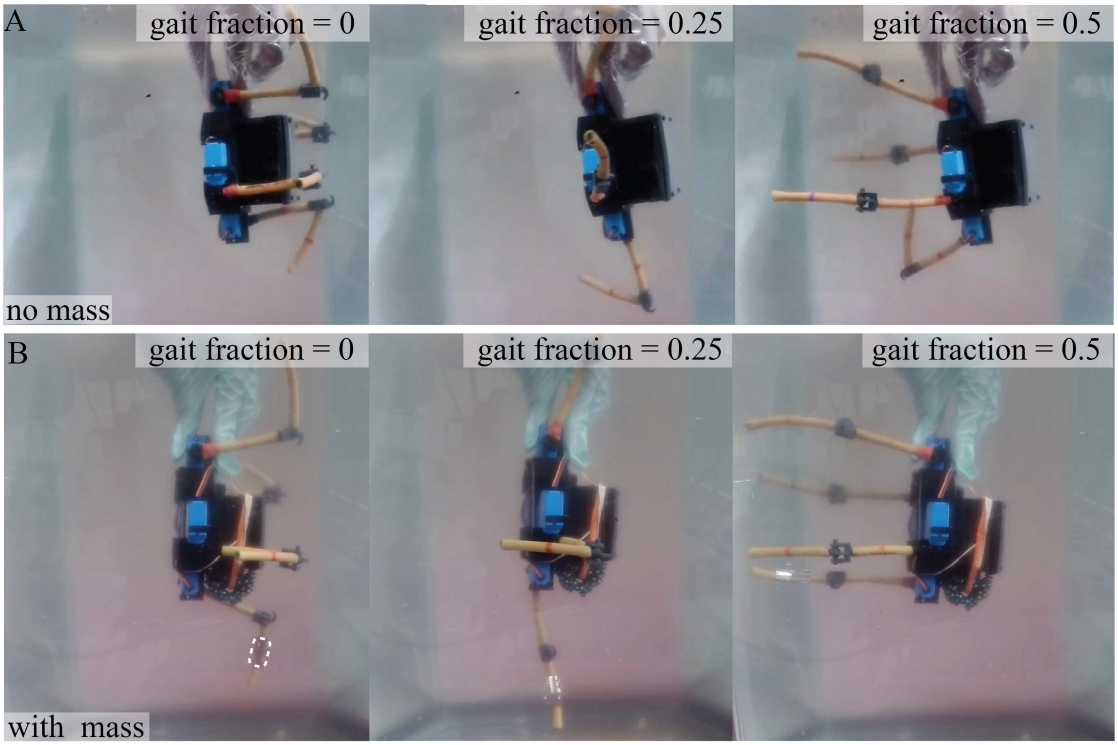

Figure 3.16: **Kinematics of robot with and without added mass.** Snapshots of robot beat pattern with no mass (A) and with added mass (B) on a single flagellum (bottom flagellum). White dashed lines highlight location where mass was placed. Snapshots show correction of beat pattern due to buoyancy of flagellum material when as mass is added. Bottom of the tank is oriented downwards in the page.

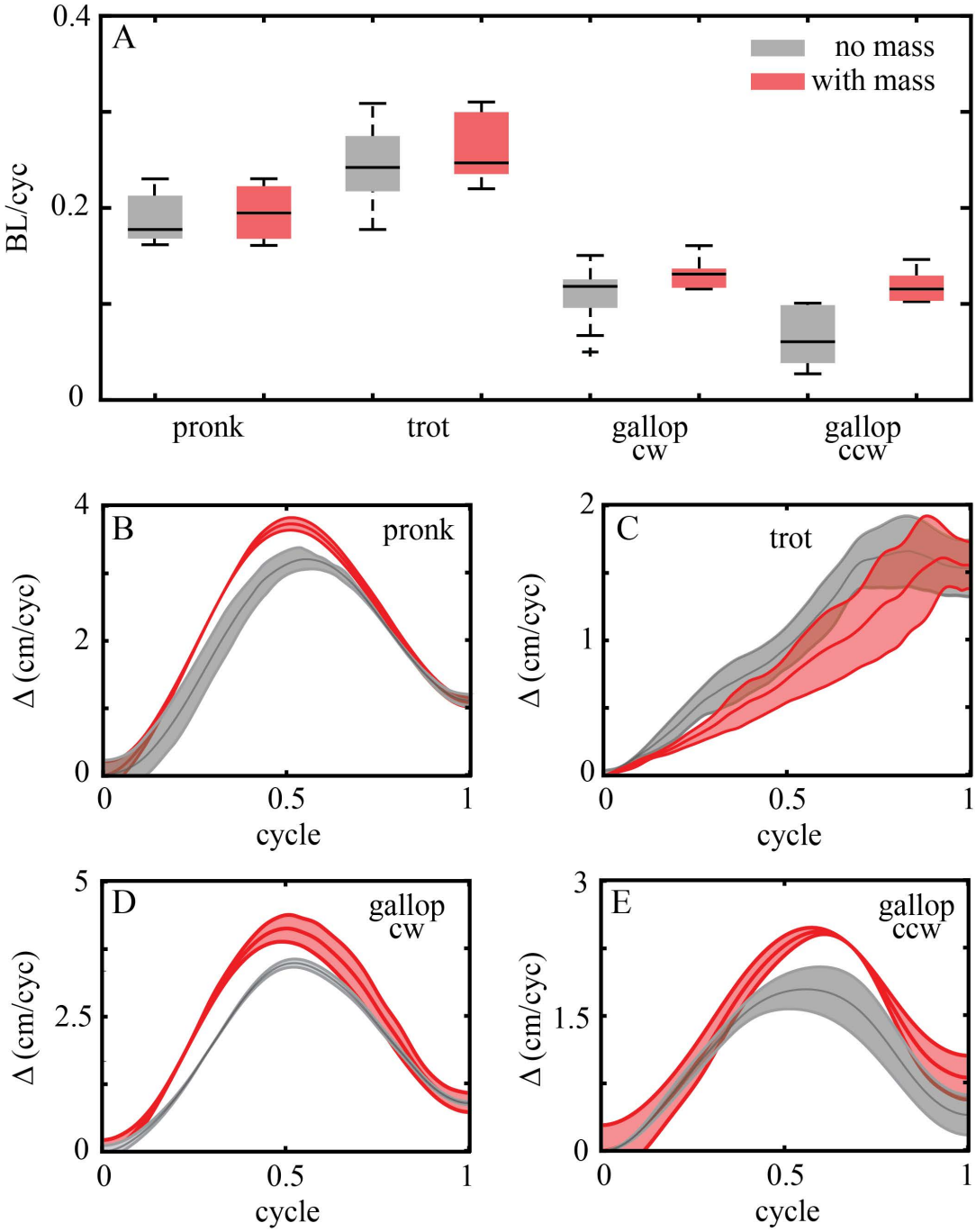

Figure 3.17: **Swimming performance of robot with perpendicular configuration with and without added mass.** (A) Body length per cycle as a function of swimming gait for the perpendicular configuration, with no mass (gray) and with added mass (red). Mean displacement over a gait cycle for all gaits - the pronk (B), trot (C), clockwise gallop (D), and counter-clockwise gallop (E). Gray lines correspond to trials with no mass. Red lines correspond to trials with added mass Shaded areas correspond to the standard deviation.

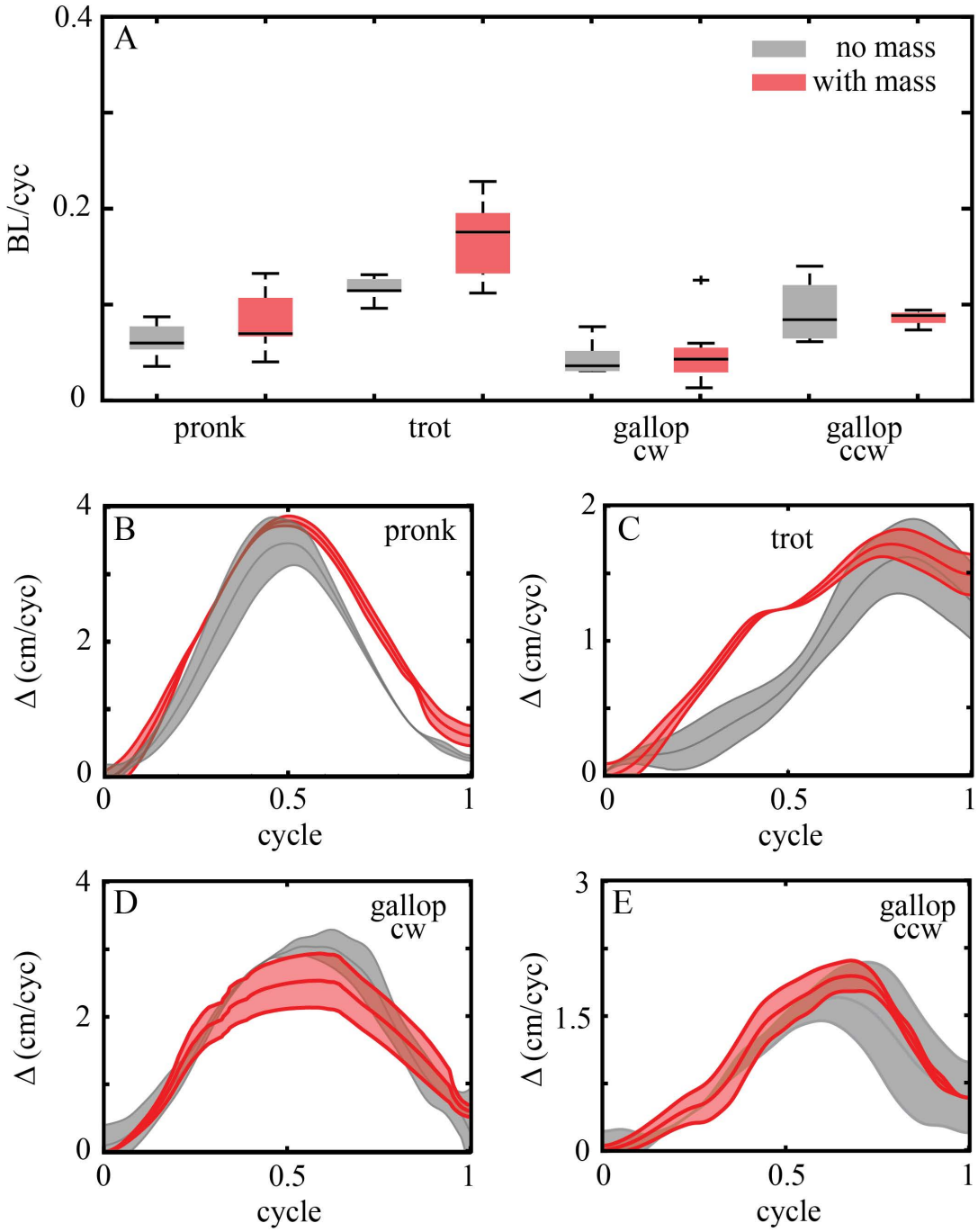

Figure 3.18: **Swimming performance of robot with parallel configuration with and without added mass.** (A) Body length per cycle as a function of swimming gait for the parallel configuration, with no mass (gray) and with added mass (red). Black crosses correspond to outliers. Mean displacement over a gait cycle for all gaits - the pronk (B), trot (C), clockwise gallop (D), and counter-clockwise gallop (E). Gray lines correspond to trials with no mass. Red lines correspond to trials with added mass Shaded areas correspond to the standard deviation.

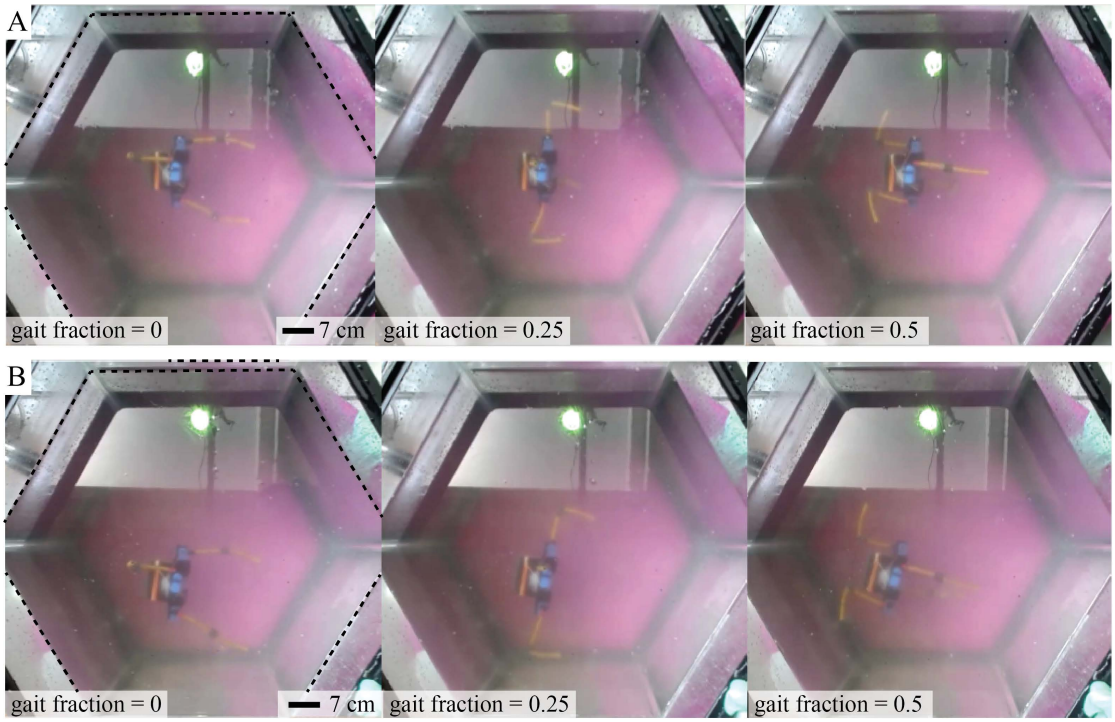

Figure 3.19: **Determining boundary effects.** Snapshots of robot performing the trot gait in the middle of the tank (A) and near the boundary (B). Black dashed lines highlight boundaries. Snapshots show negligible gait changes near the boundary (no environmental feedback). In (B) the two in-plane flagella also display good mirror-symmetry, despite the left flagellum being much closer to the boundary.

CHAPTER 4
ACTIVE AND PASSIVE MECHANICS FOR RUGOSE TERRAIN TRAVERSAL IN CENTIPEDES

4.1 Summary

Centipedes coordinate body and limb flexion to generate propulsion. On flat solid surfaces, the limb-stepping patterns can be characterized according to the direction in which limb-aggregates propagate, opposite to (retrograde) or with the direction of motion (direct). It is unknown how limb and body dynamics are modified in terrain with terradynamic complexity more representative of these animal's natural heterogeneous environments. Here, we investigated how centipedes that use retrograde and direct limb-stepping patterns, *Scd. polymorpha* and *Scc. sexspinosus*, respectively, coordinate their body and limbs to navigate laboratory environments which present footstep challenges and terrain rugosity. We recorded the kinematics and measured the locomotive performance of these animals traversing two rugose terrains with randomly distributed step heights and compared the kinematics to those on a flat frictional surface. *Scd. polymorpha* exhibited similar body and limb dynamics across all terrains and a decrease in speed with increased terrain rugosity. Unexpectedly, when placed in a rugose terrain, *Scc. sexspinosus* changed the direction of the limb-stepping pattern from direct to retrograde. Further, for both species, traversal of these rugose terrains was facilitated by hypothesized passive mechanics: upon horizontal collision of a limb with a block, the limb bent and later continued the stepping pattern. While centipedes have many degrees of freedom, our results suggest these animals negoti-

This chapter's contents are adapted from a first authored paper submitted 2022 in the Journal of Experimental Biology [101] by Kelimar Diaz, Eva Erickson, Baxi Chong, Daniel Soto, and Daniel I. Goldman

ate limb substrate interactions and navigate complex terrains by offloading complex control and leveraging the innate flexibility of their limbs.

4.2 Introduction

The study of terrestrial animal locomotion is of interest to scientists and engineers in part because of the capabilities for diverse organisms to navigate complex terradynamic environments [183, 1, 184, 185, 186, 78, 187, 188, 189, 31]. In inertia-dominated terradynamic regimes, animals use and control body and limb inertia to perform rapid locomotive behaviors and maneuvers [190, 191, 192, 13]. Studies of these animals have led to the development of robot models capable of executing similar maneuvers [193, 194, 195]. In contrast, in non-inertial regimes, animals ranging from limbless to multi-legged must continuously self-deform to generate motion and overcome damping [196, 197, 198, 35, 36, 86].

Centipedes – a class of invertebrates with numbers of limbs ranging from 15 to 191 limb pairs– are fast moving but as recent work has demonstrated, common species locomote largely within non-inertial regimes [199]. Centipedes locomote by generating and propagating a wave of limb flexion (termed here limb-stepping pattern) [55, 20]. The limb-stepping pattern can be classified depending on the direction of propagation. When the limb-aggregates (i.e., grouped limbs) are propagated opposite to the direction of motion (of the animal) they are called retrograde, whereas when they are propagated with the direction of motion, they are known as direct [62]. Previously, Manton [20] characterized how distinct orders of centipedes use either direct or retrograde limb-stepping patterns. Centipedes of the order Scolopendromorpha, Geophilomorpha and Craterostigmorpha use retrograde limb-stepping patterns, while centipedes of the order Scutigeromorpha and Lithobiomorpha use direct limb-stepping patterns. Furthermore, centipedes that use retrograde or direct limb stepping patterns exhibit distinct body dynamics. Centipedes that use retrograde limb-stepping patterns exhibit body undulation, increasing body amplitude with increasing forward speed [20, 200]. In contrast, centipedes that use direct limb-stepping patterns do not

exhibit body undulation, even when stimulated to move at relatively high speeds [20, 200]. However, what factors determine the selection of limb-stepping patterns remain unknown.

In the mid 20th century, Manton pioneered quantitative studies of centipedes and other arthropods [55, 20, 200]. Since then, few studies have focused on centipedes' locomotion, in part due to the difficulty to track the many limbs for video recordings. Previous studies have explored different aspects of centipede locomotion such as muscle activation patterns during body bending [21], gap traversal [67], the effect of compromised appendages (i.e., missing limbs) [67], and the effect of substrate friction [63]. However, these studies have been limited to flat, solid, homogeneous terrains, unlike the centipedes' natural environments. These animals must contend with heterogeneities (i.e., rocks, leaf litter, twigs) inherent to their natural surroundings. In this regime, passive adaptive responses without sensory modulation or neural feedback (often referred to as preflexes [201, 202]) may be beneficial for locomotion on rugged terrains by reducing the complexity associated with precisely controlling many degrees of freedom. Previous studies with other arthropods have revealed that complex terrain traversal can be achieved by passive mechanics. These can be inherent to the animal's morphology (e.g., passive mechanical spines along limbs in cockroaches and spiders [86, 203]) or emerge as a response to specific events (e.g., passive mechanical adhesive pads in ants [204, 205]).

In contrast to few recent biological centipede studies, synthetic (i.e., robots) multi-legged locomotors have become of interest over the last years. Such robots have been developed to perform turning maneuvers [206, 207], navigate complex environments [208, 209, 210], overcome limb failures [211], among other capabilities. However, these were designed to serve as autonomous robots, few used as models [199, 183, 212, 213] to explain centipede locomotor behaviors.

Here, we present the first study of biological centipedes locomoting on laboratory rugose terrain for two species, *Scd. polymorpha* and *Scc. sexspinosus* (Figure 4.1A,B). These two centipedes have distinct kinematics on flat solid substrates; *Scd. polymor-*

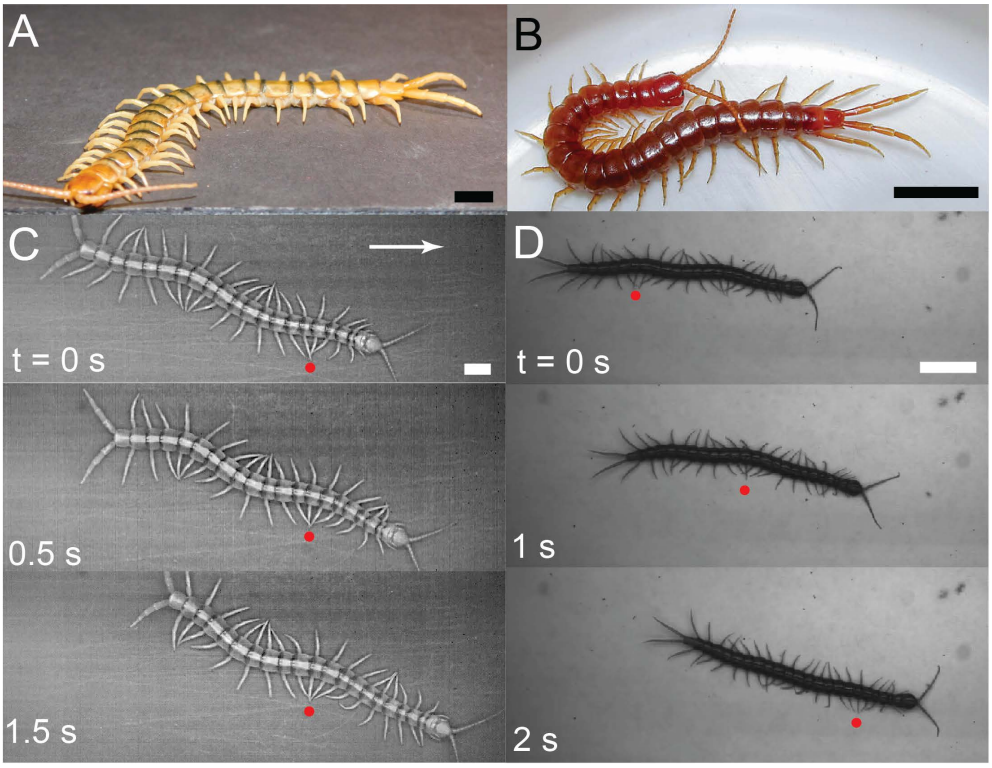

Figure 4.1: **Centipedes with distinct limb-stepping patterns.** Photo of (A) *Scolopendra polymorpha* and (B) *Scolopocryptops sexspinosus* (Image credit: Derek Hennen). Image sequence showing (C) *Scd. polymorpha* and (D) *Scc. sexspinosus* running on foam core. Red dots highlight a single location where adjacent limbs are aggregated. All scalebars correspond to 1 cm.

pha uses retrograde limb-stepping patterns, whereas *Scc. sexspinosus* uses direct (Figure 4.1C,D). Specifically, we study how these animals navigate and negotiate complex terradynamic interactions associated with the rugosity of the terrains. We report the performance of these animals for varying terrain rugosity and found that *Scd. polymorpha* does not change locomotive strategy (i.e., limb-stepping pattern) on complex terrain. In contrast, *Scc. sexspinosus* exhibits a change from a direct to retrograde. Further, we discovered an emergent passive behavior during limb-terrain interactions for both centipede species; when a limb collided with a block, it passively bent in the direction the force from the block was applied on it. Finally, we discuss the implications of gait switching in *Scc. sexspinosus* and possible advantages to the observed passive mechanics in both centipede species.

4.3 Materials and Methods

4.3.1 Animals

All centipedes were wild caught. *Scd. polymorpha* were caught in Del Rio Val Verde County Texas. *Scc. sexspinosus* were caught in Valley National Park (VNP), Summit County, Ohio. Four centipedes of each species were used in experiments with a mean body length of 7.7$\pm$1.5 cm and 6.2$\pm$1.1 cm, for *Scd. polymorpha* and *Scc. sexspinosus*, respectively. *Scd. polymorpha* had 19 body segments with 19 joints and leg pairs. *Scc. sexspinosus* had 21 body segments with 21 joints and leg pairs. Centipedes were housed separately in plastic containers on a 12 hr:12 hr L:D photoperiod at room temperature (20-22°C). Centipedes were provided a source of water and were fed mealworms weekly.

4.3.2 Flat and rugose terrains

Experiments were conducted on three different terrains (flat, less rugose, more rugose) placed in a glass tank (length = 51 cm, width = 27 cm, height = 32 cm) (Figure 4.2A). The flat terrain was a homogeneous level foamcore sheet. rugose terrains consisted of Gaussian [198, 208, 214] and inverted Gaussian distributed [215, 216] blocks of varying heights (generated via custom MATLAB code[1]), for the less and more rugose terrain, respectively (Figure 4.2B). As in [214], we define rugosity (R_g) as the standard deviation of the block heights normalized by the dimensions of the blocks ($R_g = 0, 0.17$ and 0.44 for flat, less rugose, and more rugose terrain, respectively). Dimensions of each rugose terrain were scaled to the size of each species body (length = 24 cm, width = 12 cm, for *Scd. polymorpha*; length = 16, width = 8 cm, for *Scc. sexspinosus*). Each rugose terrain consisted of a 3D printed (Stratasys uPrint SE plus, material: ABSplus P430) height field, with 8 rows by 16 columns of square blocks (length and width = 1.5 cm for *Scd. polymorpha*, length and width = 1 cm for *Scc. sexspinosus*). For *Scd. polymorpha*, block heights varied from 0 to

[1]Original code can be found in https://doi.org/10.5281/zenodo.7121219

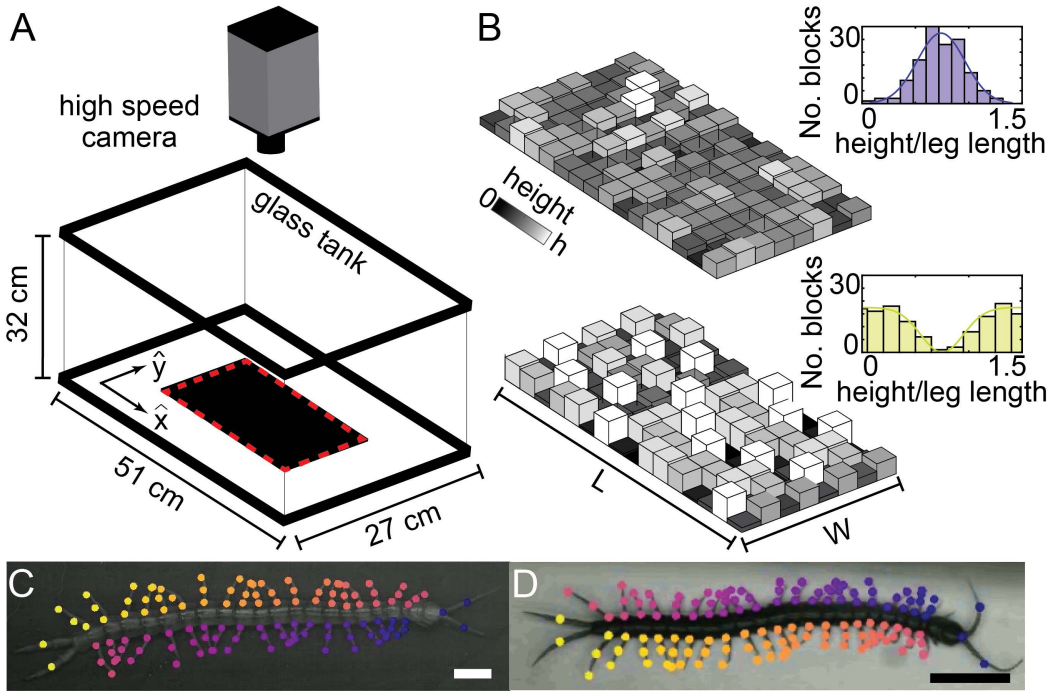

Figure 4.2: **Experimental design and complex terrains.** (A) Experimental set-up. Experiments were conducted in a 27 cm x 51 cm x 32 cm glass tank with a high speed camera placed vertically over the selected terrain. (B) Lower (top) rugose terrain ($R_g = 0.17$) with Gaussian distributed blocks of varying heights. Higher (bottom) rugose terrain ($R_g = 0.44$) with inverted Gaussian distributed blocks of varying heights. Insets shows the Gaussian (top) and inverted Gaussian (bottom) distribution for $R_g = 0.17$ and 0.44, respectively. For $R_g = 0.17$, terrain block heights vary from 0 to 1 cm and from 0 to 0.75 cm for *Scd. polymorpha* and *Scc. sexspinosus*, respectively. For $R_g = 0.44$, terrain block heights vary from from 0 to 1.5 cm and from 0 to 1 cm for *Scd. polymorpha* and *Scc. sexspinosus*, respectively. Blocks are colored by relative height. Labeled frame to track the kinematics of (C) *Scd. polymorpha* and (D) *Scc. sexspinosus* using DeepLabCut [95]. All scalebars correspond to 1 cm.

1 cm and 0 to 1.5 cm, for $R_g = 0.17$ and 0.44, respectively. For *Scc. sexspinosus*, block heights varied from 0 to 0.75 cm and 0 to 1 cm, $R_g = 0.17$ and 0.44, respectively. Terrains were placed level in the glass tank. All experiments were conducted at room temperature (20-22°C).

4.3.3 Kinematic recordings

All experiments were recorded using a high speed camera (AOS, S-motion) positioned directly over the terrains to capture the kinematics from a top-down view (Figure 4.2A).

Videos were recorded at a resolution of 1280x700 pixels and a frame rate of 738 frames per second (fps). For both species, five videos per centipede (N = 4) per terrain were collected, with the exception of $R_g = 0.44$ trials for *Scd. polymorpha* for which a centipede lost a limb and died shortly after. A trial was concluded when the centipede traversed the terrain without leaving the field of view and/or bounds of the terrain (i.e., width of the terrain). Animals that lost limbs or were molting were not used in experiments until the limbs were regrown or the animal had completed its molt. For *Scd. polymorpha*, the average trial time was 0.8 ± 0.36 s, 0.82 ± 0.57 s, and 2.67 ± 1.23 s for $R_g = 0, 0.17$, and 0.44, respectively. For *S. sexpinosus*, the average trial time was 1.09 ± 0.27 s, 1.31 ± 0.54 s, and 2.16 ± 0.81 s for $R_g = 0, 0.17$ and 0.44, respectively. For all trials, the centipedes received no external stimulus to traverse the terrains.

4.3.4 Motion tracking

Positional data was extracted from videos with animal pose estimation software DeepLabCut (DLC) [95]. Twenty frames from each video were manually labeled and then DLC provided positions for labeled points on all other frames. Each frame had 130 and 118 points manually labeled for *Scd. polymorpha* and *Scc. sexspinosus*, respectively. Three points per limb (at the body-limb point, mid-limb, and tip) were manually annotated, as well as points on the posterior and anterior antennae (Figure 4.2C,D). Points were placed within 0.5 cm of each limb-point position. Positional data obtained for *Scd. polymorpha* had a likelihood of 0.99$\pm$0.03, 0.98$\pm$.05, and 0.96$\pm$0.08 for $R_g = 0, 0.17$, and 0.44, respectively. Positional data obtained for *Scc. sexspinosus* had a likelihood of 0.96$\pm$0.08, 0.95$\pm$0.15, and 0.94$\pm$0.12 for $R_g = 0, 0.17$, and 0.44, respectively.

4.3.5 Body and limb parameters

Digitized kinematics were used to calculate the body and limb parameters using custom MATLAB code. First, a Gaussian filter was used to smooth the x- and y-coordinates of

each tracked point. Filtered body-limb points on both sides (left and right) were averaged over time to obtain a body midline. Body angles (φ) were obtained by finding the angle between the adjacent body segments. Leg angles (θ) were obtained by calculating the angle between a limb (dashed white line) and the local body segment (Figure 4.3A(i)).

Leg angles were used to calculate phase over time for each limb on the centipede's body, similar to methods in [63]. Each leg phase (ϕ_i) was obtained from the difference between changes in the leg angle ($\Delta\theta_i$) from the time average and its derivative ($\Delta\dot{\theta}_i$) (Figure 4.6) [63]. The retraction (T_{ret}) period was obtained by finding the timing between $\phi_i = 0$ and $\phi_i = \pi$. The stride (T_{stride}) period was obtained by calculating the timing between successive points when $\phi_i = 0$. Duty factor (DF) was calculated as the ratio of the retraction and stride periods ($DF = T_{ret}/T_{stride}$). Stride frequency was calculated as the inverse of the stride period ($\omega_{stride} = 1/T_{stride}$). Step length ($L_{step}$) was obtained by calculating the total distance traveled for each associated T_{ret}. Stride length (L_{stride}) was calculated as the ratio of the step length and the duty factor ($L_{stride} = L_{step}/DF$). Because steps and/or strides could be interrupted due to limb substrate collisions, DF, ω_{stride}, L_{step}, and L_{stride} were averaged for all limbs and the entirety of each trial. Statistical tests (t-test) for experimentally obtained parameters were performed using a custom MATLAB code.

4.4 Results

4.4.1 Centipede kinematics

For both centipede species, we performed 20 trials for $R_g = 0$, 20 trials for $R_g = 0.17$, and 20 trials for $R_g = 0.44$ (16 in the case of *Scd. polymorpha*) (Figure 4.3, Figure 4.4). For $R_g = 0$, *Scd. polymorpha* exhibited body waves and limb-stepping patterns propagated from head to tail (opposite to the direction of motion) along the body axis (Figure 4.3A-D(i)). In contrast, for $R_g = 0.17$ and 0.44 we observed the same limb-stepping pattern but no regular body undulation. That is, there was no body undulation that emerged from high running speeds. Instead, bands of curvature emerged due to the path that the cen-

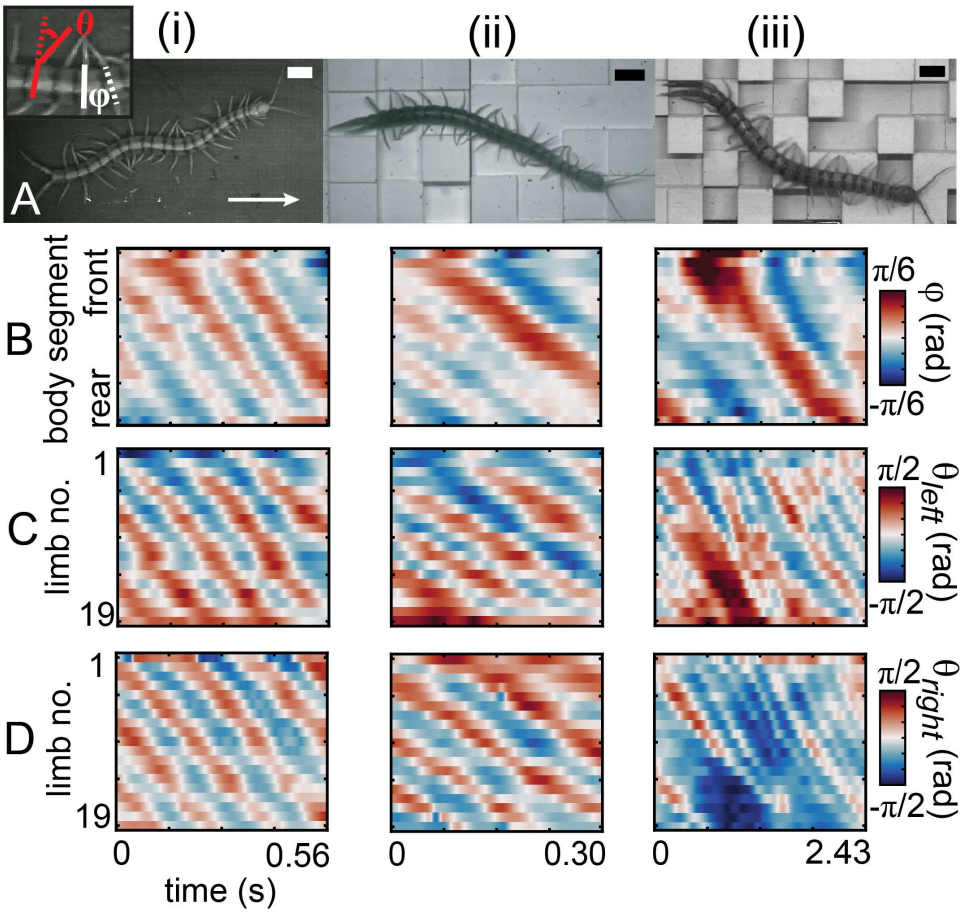

Figure 4.3: ***Scd. polymorpha* locomoting on terrains with varying rugosity.** (A) Images of *Scd. polymorpha* on terrains with rugosity (i) $R_g = 0$, (ii) $R_g = 0.17$, and (iii) $R_g = 0.44$. Arrow shows the direction of motion of the animal (left to right) for all terrains. Inset shows how both body angles and leg angles were calculated. Body angles (φ) were obtained by finding the angle between the adjacent body segments (black lines). Leg angles (θ) were obtained by calculating the angle between a limb (dashed white line) and the local body segment (red lines). All scalebars correspond to 1 cm. Heat maps show the (B) body angles and limb angles on both the (C) left and (D) right side of the animal over time. Limb numbers 1 to 19 indicate those from front to rear. All panels were generated from a single trial for each terrain.

tipedes traveled along the terrain. We observed interruptions in the limb-stepping patterns with increasing terrain complexity (Figure 4.3C-D(iii)). These correspond to limb substrate collisions; as the centipede moved across the terrain, limb substrate contact on the horizontal plane (i.e., limb contacting the side of a block) could occur due to the height disparities.

For $R_g = 0$, *Scc. sexspinosus* did not exhibit body undulation, even when running at

high speeds. However, the centipede propagated limb-stepping patterns from tail to head (direct, with the direction of motion) (Figure 4.4B-D(i)). This was surprising, as centipedes in the order Scolopendromorpha are thought to only use retrograde limb-stepping patterns [20]. For $R_g = 0.17$, *Scc. sexspinosus* demonstrated changes in their behavior. On initial trials, the animals used solely direct limb-stepping patterns. As more trials were collected, *Scc. sexspinosus* used direct limb-stepping patterns and changed the direction the limb pattern was propagated from direct to retrograde within a trial (Figure 4.4C(ii),D(ii)). Interestingly, we observed that over time (i.e., minutes, from trial to trial) these centipedes would switch more rapidly (i.e., earlier in the trial) from direct to retrograde or would only use retrograde limb-stepping patterns. We hypothesize that the centipedes actively changed the locomotive strategy faster as a result of learning [217, 218]. However, trials in which potential learning occurred were excluded from the analysis. For $R_g = 0.44$, *Scc. sexspinosus* only used retrograde limb-stepping patterns (Figure 4.4C(ii),D(ii)). Interestingly, we noticed significant body undulation in *Scc. sexspinosus* for $R_g = 0.44$; however, we posited that bands of body curvature observed in experiments (Figure 4.4B(ii),B(iii)) are passive response to the structures of the rugose terrains, related to the path of travel. Further, similar to *Scd. polymorpha*, we observed interruptions in the limb-stepping pattern, related to limb substrate collisions in the horizontal plane due to height disparities between adjacent blocks (Figure 4.4C(iii),D(iii)).

4.4.2 Performance across terrains

The direction that the limbs propagate can be characterized by the leg phase shift (LPS). LPS is defined as the fraction of time over a gait cycle in which the forelimb leads the hindlimb in a pair of adjacent limbs (Figure 4.5A). A LPS < 0.5 corresponds to direct limb-stepping patterns (propagated with the direction of motion). In contrast, LPS > 0.5 corresponds to retrograde limb-stepping patterns (opposite to the direction of motion). A LPS = 0.5 corresponds to an alternating tripod gait. In hexapods, three leg pairs alternate

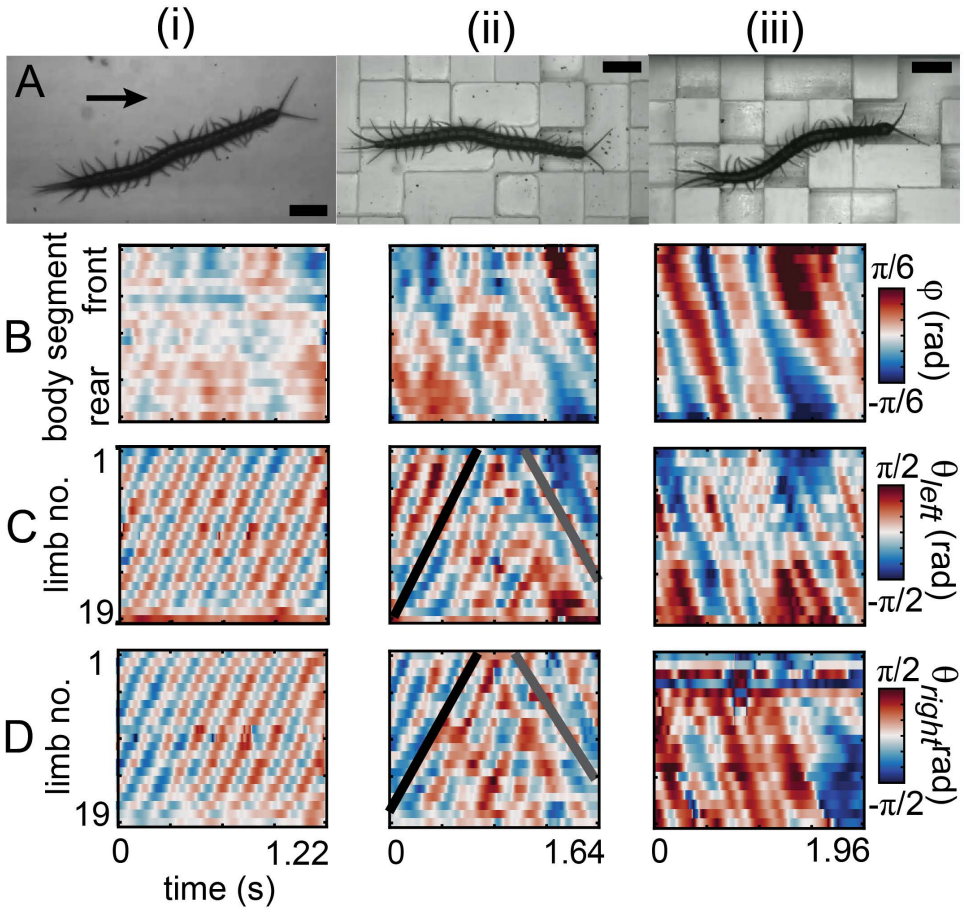

Figure 4.4: ***Scc. sexspinosus* locomoting on terrains with varying rugosity.** (A) Images of *Scc. sexspinosus* on on terrains with rugosity (i) $R_g = 0$, (ii) $R_g = 0.17$, and (iii) $R_g = 0.44$. Arrow shows the direction of motion of the animal (left to right). All scalebars correspond to 1 cm. Heat maps show the (B) body angles and limb angles on both the (C) left and (D) right side of the animal over time. Black line highlights when the animal used a direct limb-stepping pattern. Gray line highlights when the animal used a retrograde limb-stepping pattern. Limb numbers 1 to 19 indicate those from front to rear. All panels were generated from a single trial for each terrain.

ground contact, forming a tripod. In myriapods, an alternating tripod corresponds to every other leg (e.g., all even numbered legs) on the same side having the same phase. However, an alternating tripod gait has not been reported in centipedes.

We calculated the speed of both centipede species for all terrains and quantified the limb-stepping behavior by calculating the LPS. *Scd. polymorpha* achieved a speed of 0.19±0.04 body lengths per gait cycle (BL/cyc) and LPS of 0.92±0.04 on $R_g = 0$ (Figure 4.5B). Speed and LPS decreased with increasing terrain rugosity. *Scd. polymor-*

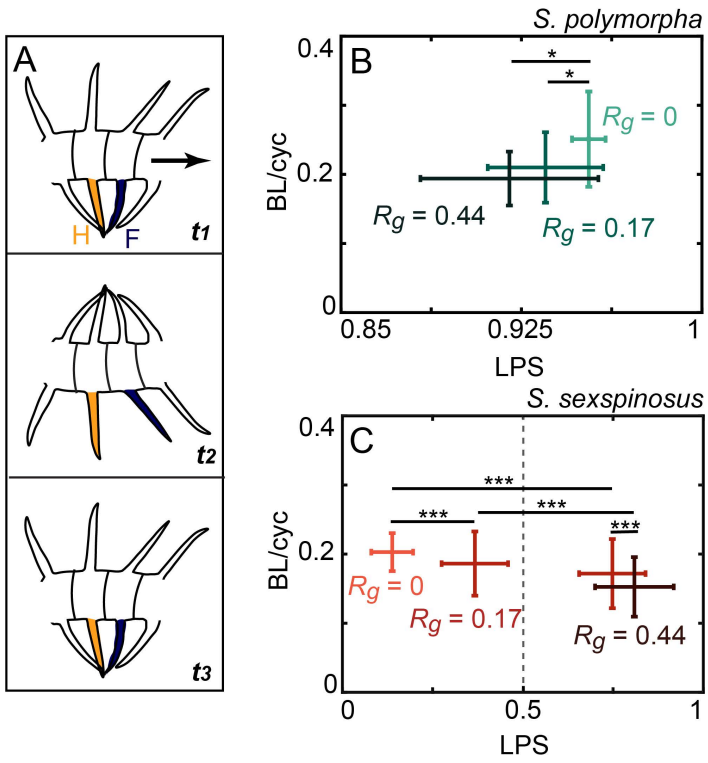

Figure 4.5: **Centipede performance as a function of average leg phase shift.** (A) Diagram of centipede segment, moving over time. Arrow shows direction of motion (left to right). Blue limb denotes forelimb, *F*, and yellow limb denotes adjacent hindlimb, *H*. Leg phase shift (LPS) corresponds to the fraction of the time a hindlimb moves in the same direction as the adjacent forelimb. (B) Displacement per gait cycle of *Scd. polymorpha* as a function of LPS on each terrain. Light green, medium green, and dark green, correspond to $R_g = 0, 0.17$, and 0.44, respectively. (C) Displacement per gait cycle of *Scc. sexspinosus* as a function of LPS on each terrain. Dashed lines corresponds to LPS = 0.5. LPS < 0.5 corresponds to direct limb-stepping patterns. LPS > 0.5 corresponds to retrograde limb-stepping pattern. Light orange, medium red, and dark red, correspond to $R_g = 0, 0.17$, and 0.44, respectively. Differences were significant at p ≤ 0.05, p ≤ 0.001 for one and three asterisks, respectively. For *Scd. polymorpha*, LPS differences were significant at p ≤ 0.05 between $R_g = 0$ and 0.44. For *Scc. sexspinosus*, LPS differences were significant at p $\leq$ 0.001 between $R_g = 0$ and 0.17 (both LPS < 0.5 and LPS > 0.5), between $R_g = 0$ and 0.44, between $R_g = 0.17$ with distinct LPS, and between $R_g = 0.17$ (LPS < 0.5) and 0.44. For *Scd. polymorpha*, five trials per animal were included in this analysis for terrains with rugosity $R_g = 0$ (N = 4), 0.17 (N = 4), and 0.44 (N = 3). For *Scc. sexspinosus*, five trials per animal (N = 4) were included in this analysis for all terrains. For $R_g = 0.17$, trials were divided by the most prominent limb-stepping pattern (i.e., used for the majority of the trial) for each animal (10 trials for direct, 10 trials for retrograde). For those trials, average LPS was calculated over the duration of the trial that the prominent limb-stepping pattern (e.g., towards the end of a trial) was observed.

pha achieved speeds of 0.21±0.05 and 0.25±0.07 BL/cyc and a LPS of 0.93±0.02 and 0.95±0.01, for $R_g = 0.17$ and 0.44, respectively. Previous studies have characterized the relationship between speed and body undulation; when traveling at high speeds, centipedes that use a retrograde limb-stepping pattern display an increase in body undulation, specifically an increase in the body wave amplitude [55, 199]. Conversely, when these centipedes travel at low speeds, there is a significant decrease in the maximum body wave amplitude, making body undulation negligible [55, 199]. Thus, lack of body undulation in *Scd. polymorpha* on the rugose terrains (Figure 4.3B(ii),B(iii)) corresponds to a decrease in speed. We note that, although on flat terrain the centipedes displayed some body undulation, centipedes were not stimulated to elicit maximum speed on any of the terrains. In other words, we allowed centipedes to move at their preferred traveling speed.

Scc. sexspinosus achieved a speed of 0.20±0.03 BL/cyc, with a LPS of 0.14±0.06 on the flat terrain (Figure 4.5C), consistent with observations of a direct limb-stepping pattern [55]. For $R_g = 0.17$, trials were categorized by LPS. *Scc. sexspinosus* had a wide distribution of LPS throughout each trial; interestingly, there were two clusters of LPS (one in the direct regime, the other in the retrograde regime) in the spectrum. When the centipede used only direct limb-stepping patterns, it achieved a speed of 0.19±0.05 BL/cyc and used a LPS of 0.37±0.09. In contrast, the animal achieved a speed of 0.17±0.05 BL/cyc and a LPS of 0.75±0.10 if it used retrograde limb-stepping patterns. Unlike with retrograde limb-stepping patterns, body undulation does not emerge in centipedes that use direct limb-stepping patterns, independent of speed [55]. In the case of *Scc. sexspinosus*, when it used retrograde limb-stepping patterns it did not exhibit body undulation. Lack of body undulation can be due to: 1) the inability of the centipede to generate and propagate traveling waves of body curvature, or 2) higher speeds not being elicited. For $R_g = 0.44$, *Scc. sexspinosus* used only retrograde limb-stepping patterns; the centipede achieved a speed of 0.15±0.04 BL/cyc and a LPS of 0.81±0.11. A retrograde limb-stepping pattern facilitates "follow the leader" between limbs; when a single limb is placed on the ground,

the rest of the limbs follow. Thus, we posit the centipede modulated the LPS to reduce the uncertainty of limb substrate placement.

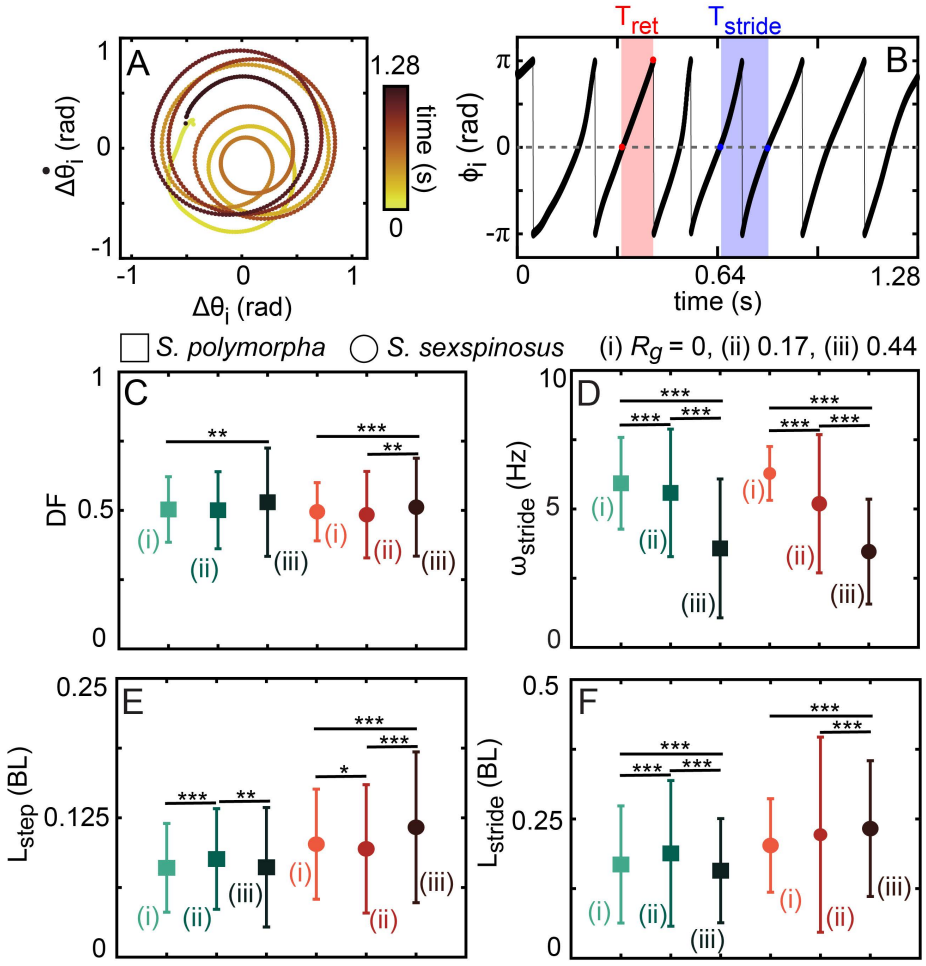

Figure 4.6: **Centipede leg parameters.** (A)$\Delta\dot{\theta}_i$ versus $\Delta\theta_i$ of a single leg of *Scd. polymorpha* on flat terrain R_g, colored by time. (B) Phase, ϕ_i, of a single leg of *Scd. polymorpha* for $R_g = 0$ over time. Red band highlights a single retraction period, T_{ret}. Blue band highlights a single stride period, T_{stride}. (C) Duty factor, (D) stride frequency (ω_{stride}), (E) step length (L_{step}), and (F) stride length (L_{stride}) for *Scd. polymorpha* and *Scc. sexspinosus* on all terrains. Green squares and orange circles correspond to *Scd. polymorpha* and *Scc. sexspinosus*, respectively. Numbering corresponds to (i) $R_g = 0$, (ii) $R_g = 0.17$, and (iii) $R_g = 0.44$. Differences were significant at p $\leq$ 0.05, p $\leq$ 0.01, p $\leq$ 0.001 for one, two and three asterisks, respectively. For *Scd. polymorpha*, five trials per animal were included in this analysis for $R_g = 0$ (N = 4), $R_g = 0.17$ (N = 4), and $R_g = 0.44$ (N = 3) terrain. For *Scc. sexspinosus*, five trials per animal (N = 4) were included for all terrains.

Phase over time for each leg (ϕ_i) was calculated to find the retraction (T_{ret}) and stride (T_{stride}) period (Figure 4.6A-B). T_{ret} and T_{stride} is the time associated with backward move-

ment of a limb during stance and the duration of a gait cycle, respectively (see Materials and Methods). These were used to calculate duty factor (DF), stride frequency (ω_{stride}), step length (L_{step}), and stride length (L_{stride}) for both *Scd. polymorpha* and *Scc. sexspinosus* across all terrains (Figure 4.6C-F).

Independent of terrain, both centipede species achieved comparable DF (Figure 4.6C). *Scd. polymorpha* used a DF of 0.50±0.12, 0.50±0.14,and 0.53±0.19, for $R_g = 0, 0.17$, and 0.44, respectively. *Scc. sexspinosus* used a DF of 0.50±0.11, 0.48±0.16, and 0.51±0.18, on $R_g = 0, 0.17$, and 0.44, respectively. This suggests small modulations to the timing between the swing and the stance are sufficient to navigate these environments, potentially due to the redundancy from their many limbs. In contrast, stride frequency (ω_{stride}) decreased with increasing terrain complexity (Figure 4.6D). However, there was comparable ω_{stride} in each terrain between centipede species. *Scd. polymorpha* used an ω_{stride} of 6.0±1.7, 5.6±2.3, and 3.6±2.5 Hz, for $R_g = 0, 0.17$, and 0.44, respectively. *Scc. sexspinosus* used an ω_{stride} of 6.3±1, 5.2±2.50, and 3.5±1.9 Hz, for $R_g = 0, 0.17$, and 0.44, respectively.

L_{step} and L_{stride} are leg parameters that can be directly impacted due to limb substrate collisions. Thus, we expected the complexity of the rugose terrains to result in modulation of L_{step} or L_{stride}. Surprisingly, there were small variations in L_{step} across the terrains (Figure 4.6E). *Scd. polymorpha* used a L_{step} of 0.08±0.04, 0.09±0.05, and 0.08±0.05 BL, for $R_g = 0, 0.17$, and 0.44, respectively. *Scc. sexspinosus* used a L_{step} of 0.10±0.05, 0.10±0.06, and 0.12±0.07 BL, for $R_g = 0, 0.17$, and 0.44, respectively. In the case of *Scc. sexspinosus*, small changes in L_{step} may be due to the animals changing the propagation direction of the limb-stepping pattern. Similarly, there were small changes in L_{stride} across the terrains, for both centipede species (Figure 4.6F). *Scd. polymorpha* used a L_{stride} of 0.17±0.11, 19±0.13, and 0.16±0.09 BL, for $R_g = 0, 0.17$ and 0.44, respectively. *Scc. sexspinosus* used a L_{stride} of 0.20±0.08, 0.22±0.18,and 0.23±0.12 BL, for $R_g = 0, 0.17$ and 0.44, respectively. Although *Scc. sexspinosus* exhibits changes in the gait, L_{step} and

L_{stride} were averaged for all trials. Averages included when the animals were using both direct and retrograde limb-stepping patterns. Therefore, some of the variance can be attributed to intervals in which these centipedes switched from direct to retrograde.

4.4.3 Passive limb mechanics

For both centipede species, we observed limb substrate collisions along the horizontal plane due to the height disparities between adjacent blocks. Instead of jamming (i.e., limbs getting stuck/caught) into a block, the centipede's limbs bent in the direction the force from the block was applied (towards the body, opposite to the direction of motion). We posit the inherent flexibility of the centipede's limbs facilitated this limb behavior to emerge passively, which we have termed "passive gliding". In previous studies [208] we found similar dynamics (i.e., passive mechanical compliance) improved locomotor performance on complex terrain of a centipede robot model without changes in the control. Thus, we hypothesize passive gliding allows centipedes to negotiate limb substrate collisions.

We identified each instance (when one or more limbs were bent due to a block at any point in time) of passive gliding for every trial of both centipede species. Figure 4.7A,C, shows examples of passive gliding for $R_g = 0.17$ for *Scd. polymorpha* and *Scc. sexspinosus*, respectively. We observed *Scc. sexspinosus* displayed a greater number of instances (27 instances) of passive gliding than *Scd. polymorpha* (19 instances). However, the number of occurrences is path dependent; different paths led to different number of occurrences of passive gliding per individual (Figure 4.7B,D). A single *Scc. sexspinosus* did not exhibit any passive gliding, while all *Scd. polymorpha* exhibited passive gliding.

Figure 4.7E,G, shows examples of passive gliding for $R_g = 0.44$ in both centipede species. On this terrain, *Scd. polymorpha* and *Scc. sexspinosus* displayed 53 and 60 instances of passive gliding, respectively. limb substrate collisions increased with terrain rugosity due to the increase of complexity (i.e., height disparities between adjacent blocks). Unlike for $R_g = 0.17$, where few limbs collided with the block, a greater number of limbs

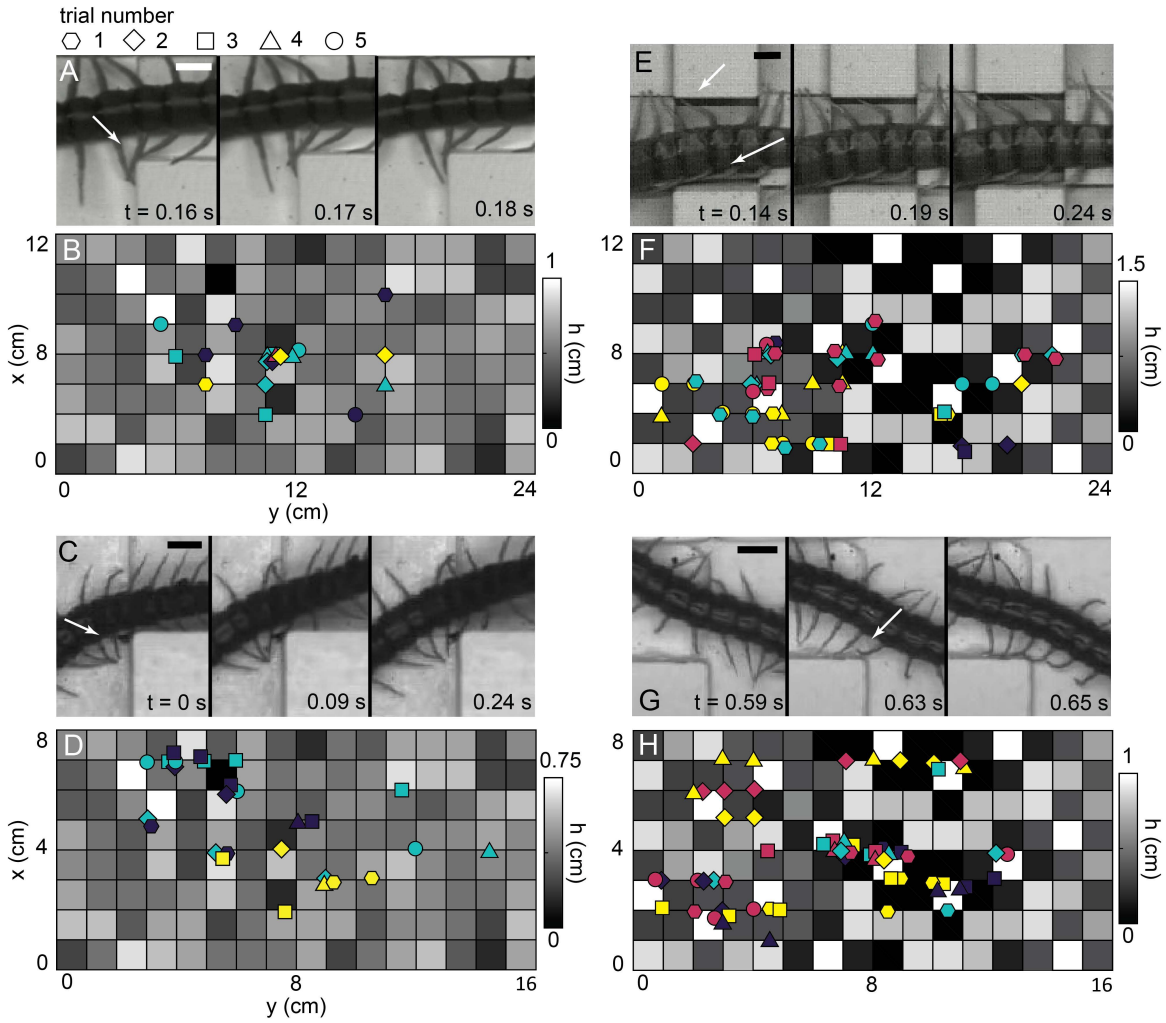

Figure 4.7: **Passive limb gliding during obstacle interference**. (A) Snapshots of passive limb gliding during limb substrate collisions and (B) locations where horizontal limb substrate collisions occurred for *Scd. polymorpha* on the less rugose ($R_g = 0.17$) terrain. Arrow highlights the limb substrate interaction. (C) Snapshots of passive limb gliding during limb substrate collisions and (D) locations where horizontal limb substrate collisions occurred for *Scc. sexspinosus* for $R_g = 0.17$. (E) Snapshots of passive limb gliding during limb substrate collisions and (F) locations where horizontal limb substrate collisions occurred for *Scd. polymorpha* on the more rugose ($R_g = 0.44$) terrain. (G) Snapshots of passive limb gliding during limb substrate collisions and (H) locations where horizontal limb substrate collisions occurred for *Scc. sexspinosus* for $R_g = 0.44$. Distinct shapes and colors correspond to individual trials and animals, respectively. All scalebars correspond to 0.75 cm and refer to terrains directly below. For *Scd. polymorpha*, five trials per animal were included in this analysis for ($R_g = 0$) (N = 4), $R_g = 0.17$ (N = 4), and $R_g = 0.44$ (N = 3). For *Scc. sexspinosus*, five trials per animal (N = 4) were included for all terrains.

exhibited passive gliding for $R_g = 0.44$ (Figure 4.7E,G). In addition, in some trials, passive gliding occurred on both sides of the body. Figure 4.7E shows an example in which limbs on both sides of the body engage in passive gliding simultaneously.

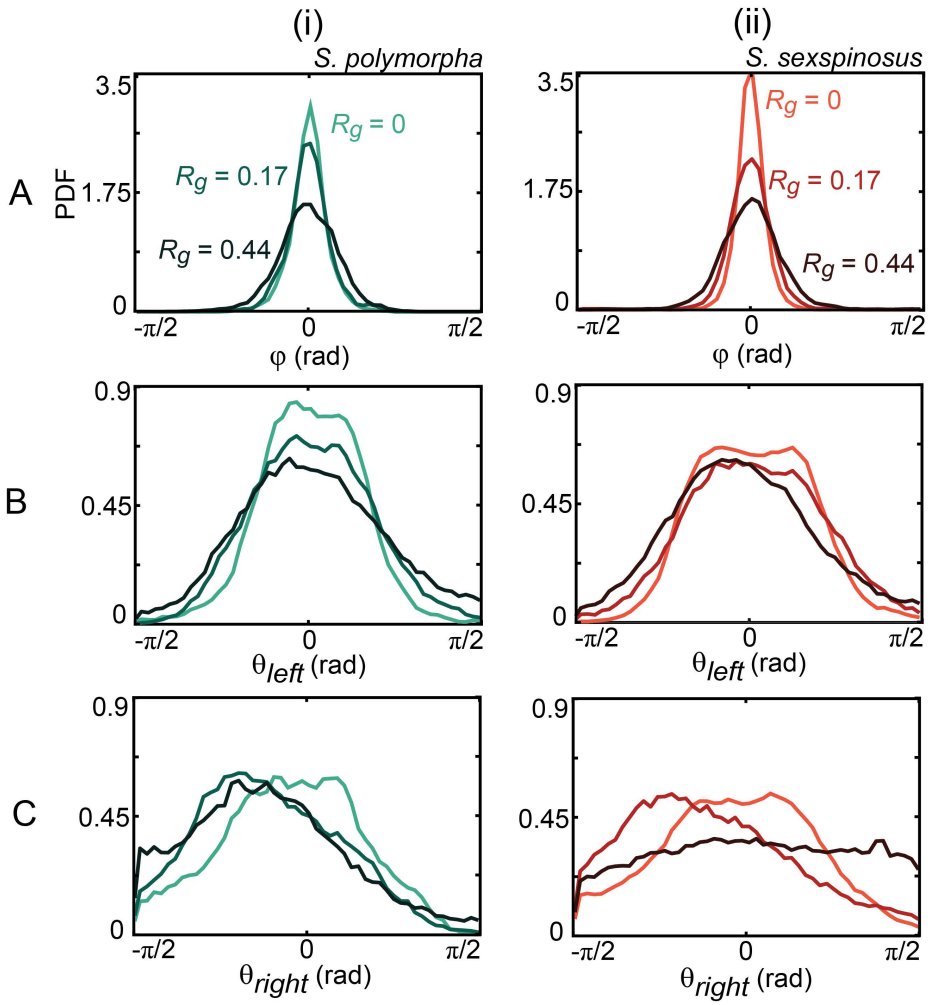

Figure 4.8: **Probability of passive limb gliding across terrains.** Probability density functions (PDF) of the (A) body angles, (B) left leg angles, and (C) right leg angles, for both (i) *Scd. polymorpha* and (ii) *Scc. sexspinosus*. For *Scd. polymorpha*, light green, medium green, and dark green, correspond to $R_g = 0, 0.17$, and 0.44, respectively. For *Scc. sexspinosus*, light orange, medium red, and dark red, correspond to $R_g = 0, 0.17$, and 0.44, respectively. For *Scd. polymorpha*, five trials per animal were included in this analysis for $R_g = 0$ (N = 4), $R_g = 0.17$ (N = 4), and $R_g = 0.14$ (N = 3) terrain. For *Scc. sexspinosus*, five trials per animal (N = 4) were included for all terrains.

We calculated the probability density function (PDF) of body and limb angles to quantify observed changes as a function of terrain. Figure 4.8A(i)-(ii) show the PDF of body

angles for *Scd. polymorpha* and *Scc. sexspinosus*, respectively. On flat terrain, PDFs are centered at 0 for both centipede species. The tails of the PDFs increase with increasing terrain complexity, corresponding to larger bends on the body. Neither of the centipede species exhibited body undulation on the rugose terrains. However, because of each terrains' complexity, there was a higher likelihood that centipedes would not travel in a straight path. Thus, bends on the body reflected in the distributions are related to movements of the centipedes when moving from one row of blocks (down or up the page) to another. PDFs for legs on the left and right side of the body are shown in Figure 4.8B(i)-C(ii) for *Scd. polymorpha* and *Scc. sexspinosus*, respectively. Shifts of the peaks of the distributions correspond to a higher likelihood of limb substrate collision with increasing terrain complexity. Due to the path dependence and passive gliding observed in the centipedes, PDFs obtained for the left and right side of the body are distinct. Thus, shifts from the peaks are more prominent for the legs on the right side of the body, corresponding to limb substrate collisions on the right side of the body.

4.5 Discussion

Results show that the centipedes' have small changes in the DF, L_{step}, L_{stride} for varying terrain rugosity, potentially due to the redundancy (i.e., many limbs and segments) in these animals [219]. For example, redundancy in the limbs may increase robustness and facilitate terrain traversal, even when a limb is compromised (e.g., damaged or lost [211]). We observed a decrease in ω_{stride} with increasing terrain complexity. However, further investigation is necessary to understand biomechanical advantages that these animals obtained with lower ω_{stride}.

We discovered that *Scd. polymorpha* and *Scc. sexspinosus* potentially leverage passive mechanics to navigate rugose terrains. When a limb collided with an obstacle, obstacle negotiation was facilitated by presumed passive limb flexion. We thus hypothesize that instead of precisely controlling every degree of freedom associated with many limbs, the

animals emergently leveraged the inherent flexibility of their limbs. Offloading the control into the mechanics is an effective strategy seen in many biological systems such as cockroaches [198, 86, 220, 221], snakes [36], spiders [86] and crabs [86], and has been successfully implemented in synthetic (robots) [86, 208, 209, 189] locomotors. Moreover, the effect of passive mechanical elements for multi-legged systems has been previously studied on myriapod robophysical models [208, 209]. Flexible passive components facilitated complex terrain traversal of the robot, whereas rigid components achieved limited performance [208].

We note that animals do not rely solely on passive body and/or limb mechanics for complex terrain traversal. Extensive research has been done in arthropods that use sensory modulation or neural feedback for stability upon external perturbations (i.e., reflexes) during quasi-static motion [222, 223, 224]. Yet, rapid running behaviors may limit reflexes, due to the lack of time to adapt to perturbations [221, 225, 226]. It is hypothesized that control (whether preflexive or reflexive) depends on the context of the animal for robust locomotion [226]. Individual control of the limb dynamics may emerge during slow walking behaviors, as seen in other arthropods [227, 228]. However, unlike in arthropods with few leg pairs, the presence of redundancy in centipedes potentially reduces the need for reflexive control. That is, even if some legs fail to make proper limb substrate contact, the centipede's many limbs can offer other points of support and stability.

We posit these strategies (passive mechanics and redundancy) are advantageous in these centipedes' natural environments. *Scd. polymorpha* is a desert dwelling centipede whereas *Scc. sexspinosus* can be found in forests within leaf litter, detritus, and under rotting logs. Both of these centipedes must contend with heterogeneities and height disparities inherent of the many materials in their surroundings.

It is commonly accepted that centipedes in the order Scolopendromorpha, Geophilomorpha, and Craterostigmorpha use retrograde limb-stepping patterns, while those in the order Lithobiomorpha and Scutigeromorpha use direct limb-stepping patterns (as character-

ized by Manton [20]). In addition, it is commonly accepted that the direction in which the limb-stepping pattern is propagated is fixed (the "one-species-one wave hypothesis" [63]). *Scc. sexspinosus* exhibited behaviors contrary to both of these. While *Scc. sexspinosus* is of the order Scolopendromorpha (Cryptopidae family), instead of retrograde it uses direct limb-stepping patterns on flat solid surfaces. Moreover, when locomoting on rugose terrains, *Scc. sexspinosus* exhibited changes in the LPS corresponding to a change of limb-stepping pattern (i.e., change in gait). This change in LPS is not unique to *Scc. sexspinosus* or centipedes of the order Scolopendromorpha; previous studies have found changes in the limb-stepping pattern with changes in the substrate [200, 67, 63, 229] in different centipede species. Therefore, further investigation of centipede locomotion is necessary to evaluate and advance understanding across these orders.

When presented with a terrain with height disparities, *Scc. sexpinosus* modulated the limb-stepping pattern. We observed comparable performance independent of the direction that the limb-stepping pattern was propagated (for $R_g = 0.17$ terrain). However, why this is a desirable strategy for this centipede remains unknown. We posit such a strategy increases the probability of finding a secure foothold. By using a retrograde limb-stepping pattern, the centipede can place a limb on the terrain and posterior limbs follow. Thus, the uncertainty associated with a direct limb-stepping pattern is reduced by switching to a retrograde pattern. Further investigation is necessary to understand the biomechanical advantage in this transition. Moreover, it is important to note that while *Scc. sexpinosus* used direct limb-stepping patterns on flat surfaces, that is not the centipede's natural environment. Therefore, the limb-stepping patterns these centipedes use in nature may be retrograde and not direct.

The kinematic analysis of these experiments was constrained to two dimensions (along the long and short axis of the centipede). However, sagittal movement along the height of surface (out/into the page) could play an important role. In flat terrain, these centipedes exhibit lifting of the body during locomotion. In rugose terrains, these animals may fall

into cavities formed by the blocks where lifting of the body to continue terrain traversal is essential. In other instances, centipedes have segments of the body suspended in air while crossing large gaps. At those instances, it is possible the limb dynamics may change (i.e., from periodic to no leg movement when crossing gaps [183, 213]) depending on the local surroundings of each body segment. Further examination is required to understand contributions in three dimensions in biological centipedes. Nevertheless, previous studies on a centipede robot [208] shows passive elements facilitated passive dorso-ventral flexion, augmenting the capabilities of the robot.

4.6 Conclusion

We performed, to the best of our knowledge, the first experiments with myriapods on terrains with features modeling natural habitats and terradynamic complexity. We explored the effects of terrain complexity on body and leg dynamics on two centipede species, *Scd. polymorpha* and *Scc. sexspinosus*. Both of the centipede species studied were from distinct environments and differ morphologically. Yet, these animals leveraged their morphology and physiology to traverse complex terrains. We observed these animals used passive gliding of the limbs during limb substrate interactions, potentially minimizing gait perturbation and facilitating traversal. Further, on the rugose terrains, *Scc. sexspinosus* exhibited changes in the LPS corresponding to a change in the propagation direction of the limb-stepping pattern (i.e., from direct to retrograde). We note that the results presented here correspond to a relatively small sample size (N = 4) for both centipede species. However, our results are general and repeatable even when centipedes were not in optimal conditions (i.e., missing limbs). That is, we observed the behaviors presented here in trials with other individuals that did not meet the necessary criteria to be included in the results discussed.

In *Scc. sexspinosus*, active changes in the gait may reflect the plasticity of these animals in response to changes in the environment. This may be due to selective pressures related to the variability of the composition of this centipede's environment. Comparable loco-

motive performance between centipede species and previous robotic studies [208] suggests that changes in gait do not improve locomotor performance. However, both our results and previous studies [200, 67, 63, 229] suggest that gait selection is coupled to the centipede's immediate surroundings. We posit a retrograde limb-stepping pattern increases the probability of secure footholds and reduces the force on the limbs upon a limb substrate collision (due to passive limb gliding) in rugose terrains.

Future comparative work could extend to other centipedes species to study their locomotive strategies in rugose terrains. This could offer insight to the environmental information these animals use to select gaits. In addition, three dimensional kinematic analysis may provide insight into the observed lifting of the body during locomotion and the effects during complex terrain traversal. Moreover, future work could explore the locomotive performance as a function of the number of leg pairs on rugose terrains with not only live animals but also robophysical models, useful as scientific models and in tasks such as search and rescue [208, 230].

4.7 Contributions

The contributions for the project are detailed as follows:

Eva Erickson performed animal experiments and tracking on all terrains. Daniel Soto designed and 3D printed each rugose terrain. Kelimar Diaz provided experimental guidance, and analyzed and processed the data. Kelimar Diaz, Eva Erickson, Baxi Chong, and Daniel I. Goldman conceived the study and interpreted the results. Kelimar Diaz wrote the original manuscript [101]. Daniel I. Goldman supervised the project, provided comments on and modified the original manuscript [101].

CHAPTER 5

WATER SURFACE SWIMMING DYNAMICS IN LIGHTWEIGHT CENTIPEDES

5.1 Summary

While locomotion on the surface of water is ubiquitous, previous studies have focused on discrete environmental contact, where limb surface interactions lead to propulsion. In contrast, less is known propulsion via continuous contact (i.e., body surface interactions). Here, we present a centipede (*Li. forficatus*) that locomotes at the interface via body surface interactions. This centipede does not predominantly use its 14 pairs of legs to locomote, rather it exhibits tail-to-head (direct) body waves to swim across the surface. Its low mass and body-fluid contact yield locomotion dynamics in which fluid wave drag forces dominate inertia. We posit direct waves lead to non-inertial forward motion due to the animal's experienced drag anisotropy (ratio of normal to tangential forces). Inspired by hispid flagella in microorganisms in viscous fluid, we posit forward motion using direct waves is achieved by modulation of the centipede's ratio of local normal to tangential forces (drag anisotropy, less than one) due to its morphology. Thus, we modeled this centipede's locomotion using surface wave RFT with experimentally resolved drag force relations of a centipede segment (slender body, extended limbs). Surface wave RFT predictions capture the animal's swimming performance and shows the locomotor strategy facilitates high performance, and potentially simplifying the animal's neuromechanical control.

This chapter's contents are adapted from a first authored paper submitted 2022 in Physical Review Letters [102] by Kelimar Diaz, Baxi Chong, Steven W. Tarr, Eva Erickson, and Daniel I. Goldman

5.2 Introduction

Locomotion at the water surface is a common behavior across scales [186]. Research on surface swimmers has focused on animals using limb surface interactions for propulsion (e.g., arthropods [231, 232, 233, 234, 235, 236], lizards [237, 238]). Inspired by the diverse water-running strategies, researchers have developed cm-scale robots that model limb surface interactions comparable to their biological counterparts [231, 239, 240, 241]. Yet, locomotion at the interface is not solely achieved via limb surface interactions. Various animals (e.g., waterlily leaf beetle larva, salamanders, geckos) locomote at the water surface using primarily body surface interactions [232, 31, 242]. However, these studies have been limited to animals possessing two to four leg pairs; the swimming dynamics of many-legged animals are less studied. Particularly, centipedes possess many limbs and inhabit diverse environments. Studies on centipedes have explored limb and body dynamics [55, 200, 20, 21, 67, 67, 63, 101] on solid surfaces. Studies of centipedes on fluids [229] have been limited to subsurface dynamics.

Arthropods with few limbs are capable of supporting their body at the interface for propulsion. In contrast, multi-legged systems potentially rely on continuous contact due to their multi-segmented, elongated bodies. Animals that rely on body surface interactions for locomotion experience forces on their body that depend on the physical properties of the environment, the body orientation (angle of attack), and the instantaneous velocity. To model swimming in bulk fluids, Resistive Force Theory (RFT) has been extensively used since the mid-20th century due to its simple approximations in comparison to complex hydrodynamics in the presence of moving boundaries [73, 79]. That is, RFT integrates the experienced thrust and drag on infinitesimal body segments of slender objects, assuming each hydrodynamic field is decoupled from other elements. Previous studies have used RFT to model locomotion in highly damped regimes, where viscous or frictional forces dominate over inertial forces [71, 75, 76, 77, 78, 79, 35, 37, 243], and thus the integral

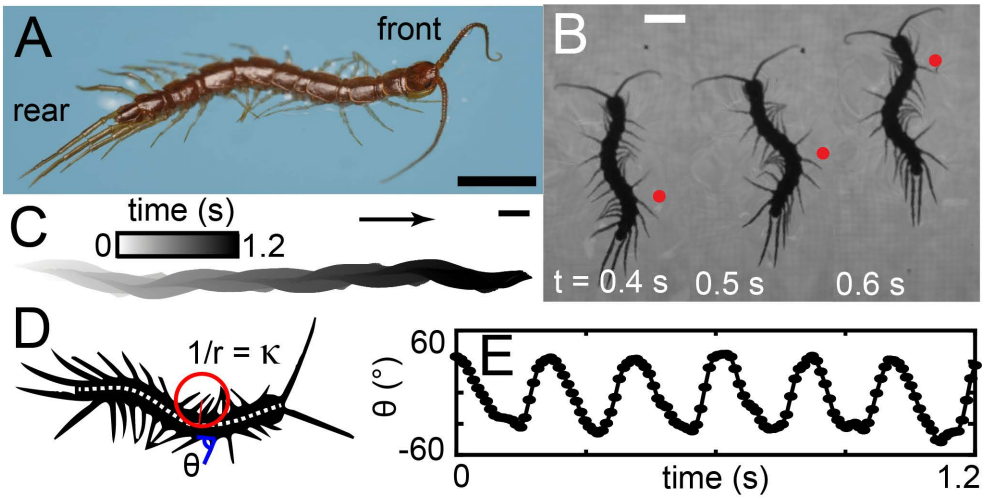

Figure 5.1: **Swimming dynamics of *Lithobious forficatus*.** (A) Photo of *Li. forficatus* on the surface of water (image credit: Kenneth Wang). (B) Snapshots of *Li. forficatus* swimming behavior. Red circles highlight body segments with large body curvature, propagated towards the head. (C) Centipede swimming trajectory (body midline), colored by time. (D) Diagram of leg angles (θ) and body curvature (κ) calculations. θ was obtained by finding the angle between the leg and the local body segment. κ was determined by fitting a circle at each point (s) along the centipede's body midline. (E) θ over time for the 7th leg (left side of the body). All scalebars correspond to 0.5 cm.

of stresses is equal to zero. Further, RFT can be extended to model locomotion of slender bodies with rigid components perpendicular to each element (i.e., microorganisms with hispid flagella [70, 66, 243]).

Here, we perform the first study of a water surface swimming centipede, *Lithobious forficatus*, and discover that its propulsion is dominated not by its 28 limbs (14 limb pairs) but by surface waves generated by rear-to-front body undulation (Figure 5.1A-B). A Schlieren method used to reconstruct the water surface indicates that the animal propels via continuous emission of surface waves. Inspired by similarities of the swimming dynamics to those of animals in highly damped regimes (e.g., low Reynolds fluids [71, 73, 75, 76, 77] and granular frictional fluids [79, 78, 35, 37]) we model the locomotion using RFT with empirically measured drag force relations of a slender body with extended limbs. The surface wave RFT calculations capture swimming performance and suggest that the animals generate body waves which achieve high performance without introducing potentially un-

desirable limb-body collisions. Further, RFT shows addition of body waves to the limb dynamics may be advantageous to reduce the neuromechanical complexity associated with multi-terrain traversal.

5.3 Body dynamics in centipede surface self-propulsion

We performed the first study of a water swimming centipede using the environment generalist *Lithobious forficatus* (length = 2.3±0.3 cm, 16 segments, and 14 leg pairs, N = 8, n = 32 trials, subsection 5.9.1). Experiments consisted of placing the centipedes on a water-filled tank (128x48.5x32 cm, 4cm deep, 25-26°C) and recording their kinematics using a high speed camera (AOS, S-motion) positioned over the tank (Figure 5.4A). When placed on the water surface, centipedes used body undulation for propulsion (Figure 5.1B). Surprisingly, the direction of propagation of the body wave was the same as the direction of motion (a direct wave, Figure 5.1B-C,F).

The propagation of direct body waves was unexpected for several reasons. First, other swimming macroscopic undulators (e.g., snakes, eels, amphibious centipedes [229]) propagate the body wave against the direction of motion (retrograde). Second, centipedes in the order Lithobiomorpha are thought unable to generate body undulation [20]. Further, centipede gaits and body dynamics are thought to be fixed (i.e., the "one-species one-wave hypothesis" [63]). However, as observed in *Li. forficatus* and other centipede studies ([229, 63, 67, 101]), these animals can exhibit distinct behaviors upon external perturbations.

Unlike in amphibious centipedes [229], we did not observe changes in the limb dynamics on solid or fluid surfaces. Instead, the limbs exhibited a direct stepping pattern. During swimming, the legs oscillated using a maximum leg amplitude (θ_{max}) of 34.2±7.5°. However, without body undulation, displacement was negligible. Using direct body waves, the centipedes achieved swimming speeds of 0.22±0.03 body lengths per gait cycle (BL/cyc), with a maximum amplitude of 3.9±1.5 cm^{-1} and a spatial frequency of 1.3±0.23. In addition, we digitized the body midlines (using custom MATLAB code) and performed

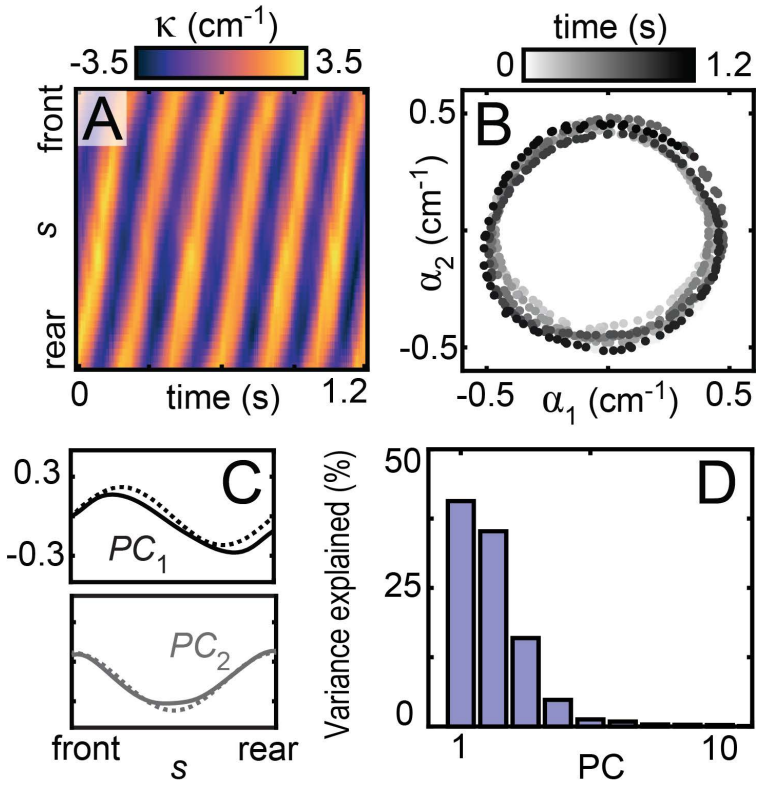

Figure 5.2: **Low dimensional representation of *Lithobious forficatus* swimming dynamics.** (A) Space-time heatmap of κ. (B) PCA of κ for centipedes swimming (n = 8, N = 32). Dashed curves correspond to fits (Fit for $PC1 = 0.22\sin(s)$, fit for $PC2 = 0.22\cos(s) - 0.15$) (C) Projection of PC_1 and PC_2 amplitudes (α_1, α_2, respectively) colored by time. (D) Variance explained as a function of PC. First two components (PC_1, PC_2) captured 75.9% of the variance. All scalebars correspond to 0.5 cm.

principal component analysis (PCA) (inspired by [8, 36]) on the body curvature (κ) to find a low-dimensional representation of the animal's body shapes. We found that two principal components (PCs) captured most of the variance of the shapes (75.9%) and were well fit by a sine and a cosine, corresponding to a wave of curvature traveling up the body (towards the head) (Figure 5.2). Furthermore, when the animal stopped undulating its "coasting" displacement was negligible (0.05 ± 0.02 BL). This suggests that these animals locomote in a highly dissipative regime, where displacement relies solely on internal shape changes, analogous to the dynamics of microorganisms and sandswimmers. We note that these centipedes are lightweight (mass 0.12 ± 0.03 g) and currents generated by air can displace the animals when they are not generating body undulation. However, the animals do not

generate persistent flows that could influence propulsion.

5.4 Surface waves

In highly damped regimes, locomotors generate the appropriate reaction forces to overcome damping from viscous or frictional drag forces [71, 75, 76, 77, 78, 79, 35, 37, 243]. In the surface swimming centipede, as noted above, no persistent flows were generated and air resistance was negligible. However, we observed that the centipedes emitted waves during propulsion and thus posited that the animals locomote such that propulsion is dominated by surface wave drag, instead of viscous drag. Because little work has been done to study such a locomotor regime, we next sought to quantitatively measure the emerging surface waves to gain insight into the propulsion and dissipation mechanisms.

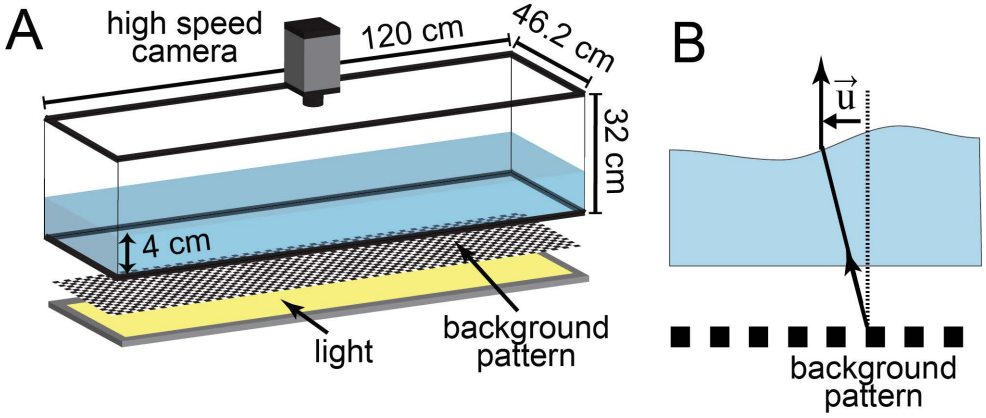

Figure 5.3: **Surface wave reconstruction apparatus.** (A) Experimental apparatus for wave reconstruction. (B) Schematic of the synthetic Schlieren imaging scheme. Changes in the original background image are denoted by $\vec{u}$ [244].

Surface waves generated by *Li. forficatus* during swimming were reconstructed using a synthetic[1] (Figure 5.3A-B) Schlieren imaging technique known as Fast Checkerboard Demodulation [244, 246] (see subsection 5.9.3). Wave reconstruction resulting in measured wave height versus time revealed transient and periodic dynamics (Figure 5.4A,C). Transient motion of the wave heights occurred when the centipede's shape changed from

[1]Traditional Schlieren requires the use of aligned masks for wave reconstruction. However, the accuracy of the alignment is critical and non-trivial (see [245])

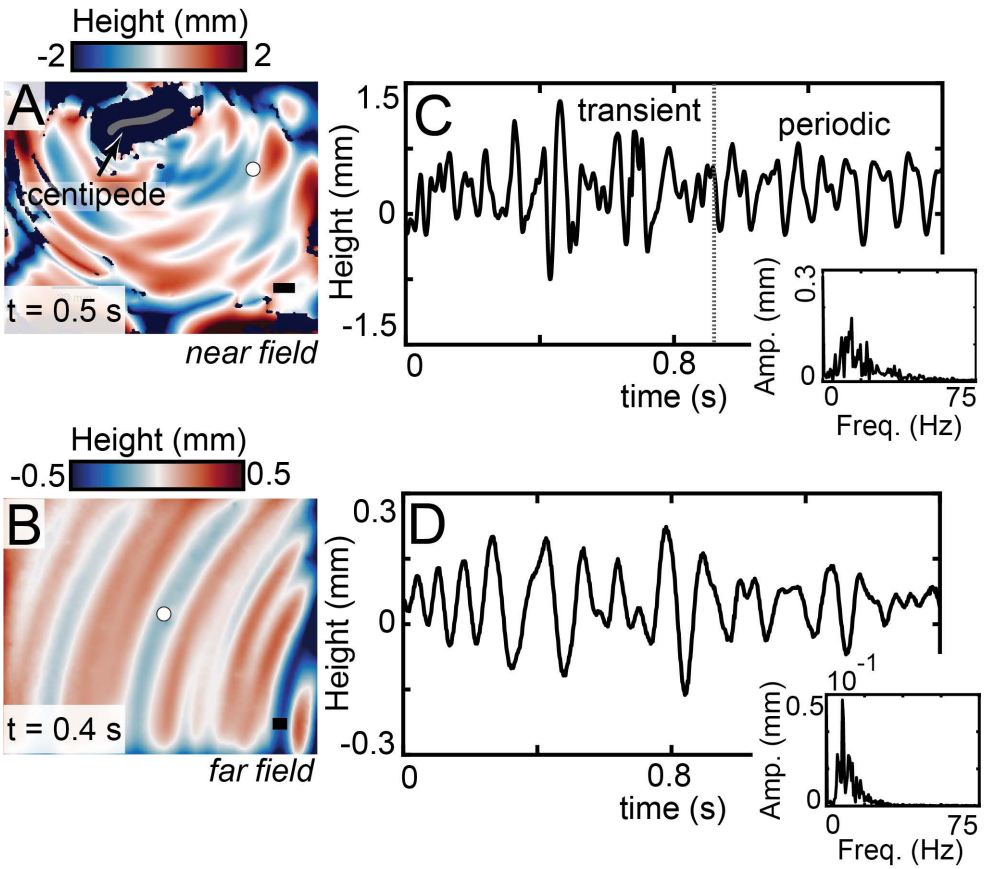

Figure 5.4: **Surface wave reconstruction during centipede swimming.** Snapshots of reconstruction of surface waves generated by *Li. forficatus* at the (A) near field and (B) far field. Grey and dark blue region correspond to masks for the centipede body a legs, respectively. Dark blue regions that are not in contact with the centipede body mask correspond to areas where the reconstruction criteria was not met. Wave surface height over time for a selected region (white circle in A,B) at the (C) near field (D) far field. Insets show single sided amplitude spectrum of surface wave heights.

a straight to undulating body associated with changes in the gait (during startup, presumed to be from limb to body-dominated). Periodic motion of the wave heights occurred when the centipede constantly propagated body waves. Constant self-deformation for propulsion is characteristic of locomotion in non-inertial regimes [36, 37, 35] such that coasting or gliding phases do not occur. In terrestrial and low Reynolds number regimes, dissipation is due to frictional and viscous forces. We hypothesize dissipation occurs in this centipede via the generation of fluid surface waves which carry energy away to the boundary. The transition from transient to periodic is characteristic of the shape changes in the animal and

an increasing distance from the point where wave heights were measured. In the far field, we observe changes in the wave heights that correspond to a periodic phase and dissipation (Figure 5.4B,D).

5.5 Drag measurements

RFT allows predictions of drag-based thrust in self-deforming locomotors [75, 76, 77, 78, 79, 35, 37]. In non-inertial systems, the key insight is that the direction of motion and speed of an undulator are governed by the ratio of normal (F_n) to tangential (F_t) forces experienced by each presumed-independently translating element. When this drag anisotropy (F_n/F_t) is greater than one for all elements, retrograde waves produce forward propulsion [75, 76, 77, 78, 79, 35, 37]. RFT can be extended to objects that have rigid components perpendicular to the object's surface, as in hispid flagella in microorganisms [66, 243]. This flagellum's morphology creates an effective F_n/F_t less than one over the length of the flagellum, resulting in forward displacement using direct waves [69, 70, 66]. We posit that because the flagella [70, 66, 243] and the swimming centipede share similar morphology (i.e., extended components), have comparable wave dynamics (i.e., direct waves), and operate in non-inertial regimes, the centipedes experience an effective $F_n/F_t < 1$ and thus their locomotion can be modeled using RFT.

Because RFT requires inputs from drag forces and these had not been previously made at the air-water interface, we sought to obtain the appropriate force relations. Drag measurements were performed with an H-shaped resin printed segment (length = 12 mm, width and height = 2 mm, leg thickness = 0.5 mm) modeling the slender body with two leg pairs to obtain steady-state drag force (F), and resolve F_n and F_t. Because the force magnitudes were small, we developed a reflection-based drag measurement apparatus (Figure 5.5A, see subsection 5.9.2). The drag apparatus was attached to a robot arm (Denso VS087) and translated at constant speed (v_d) for different attack angles (β_d). F was defined as the force obtained from 51 to 56 cm drag distance. Although the centipedes oscillate their limbs dur-

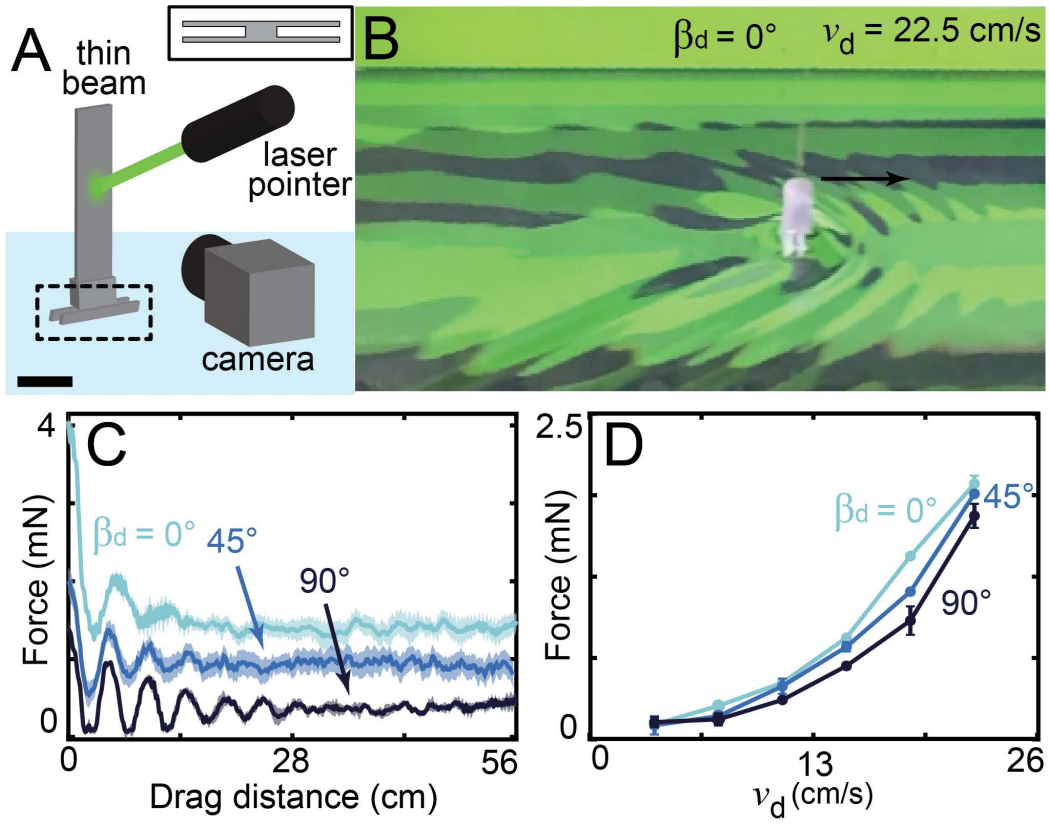

Figure 5.5: **Water surface drag measurements.** (A) Experimental apparatus for drag measurements. Dashed square highlights model segment. Inset shows top down view of model segment. Scalebar corresponds to 1 cm. (B) Snapshot of surface waves generated by model segment dragged at the interface for $\beta_d = 0°$ at $v_d = 22.5$ cm/s. Arrow shows direction of drag. Surface waves were not obtained from Schlieren reconstruction; a horizontal line background pattern with high contrasting colors was used to visualize surface waves [247]. (C) Average drag force collected at v_d = 11.25 cm/s for β_d = 0° (light blue), 45° (medium blue), and 90° (dark blue). (D) Average steady state force as a function of v_d for β_d = 0°, 45°, and 90°.

ing swimming (θ_{max} = 34.2±7.5°), the model segment had limbs oriented perpendicular to the body (θ_{max} = 0°), corresponding to the limb's time-average position.

Forces during drag for select β at v_d = 11.25 cm/s are shown in Figure 5.5C. Average F decreased with increasing β_d, and increased quadratically with v_d (Figure 5.5D). We decomposed F into contributions along the normal and tangential directions (F_n, F_t) of the model segment (Figure 5.6A-B). F_n and F_t were well-fit by a sine and a cosine function, respectively (Figure 5.12) and decreased with decreasing v_d. For most conditions, F_n/F_t increased with increasing β_d for all v_d (Figure 5.6C-D). Although at β_d = 60° F_n/F_t ap-

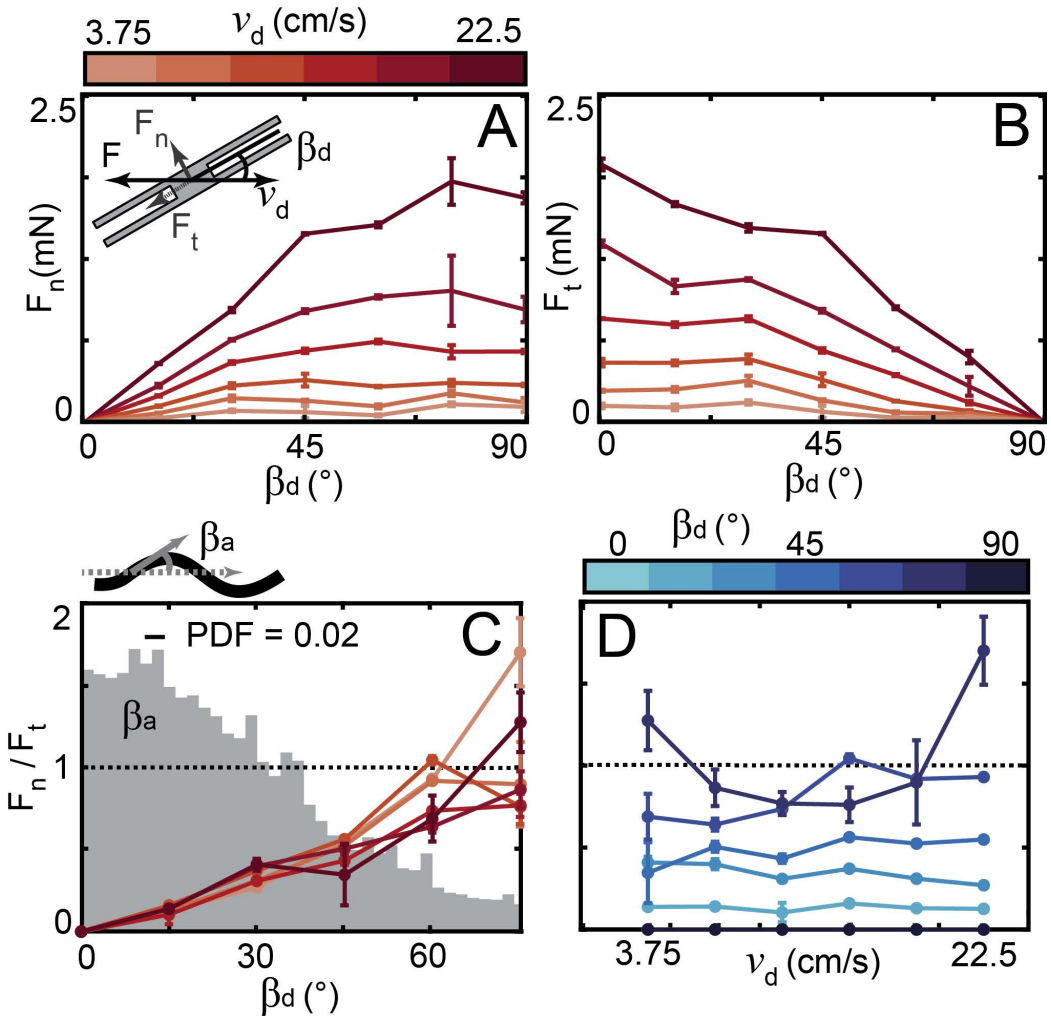

Figure 5.6: **Force decomposition and drag anisotropy for surface wave drag.** Force contributions along the (A) normal and (B) tangential direction of the dragged object. Inset in A shows to top view of the model centipede segment moving at angle β_d with constant v_d. (C) F_n/F_t as a function of β_d for varying v_d. Solid gray area shows probability distribution function (PDF) of the angle of attack (β_a) measured in the swimming centipedes. β_a is defined as the angle between a local tangent angle and the average direction of motion (inset). (D) F_n/F_t as a function of v_d for varying β_d. Black horizontal dashed lines correspond to $F_n/F_t = 1$.

proached one, the centipedes exhibit attack angles (β_a) primarily from 0° to 45°. Further, F_n/F_t was insensitive to v_d. The insensitivity of F_n/F_t to v_d suggests locomotor performance is primarily dependent on the self-deformation pattern.

5.6 Surface wave Resistive Force Theory

We used RFT to obtain theoretical predictions on swimming performance (Figure 5.7). Experimentally obtained F_n and F_t were fitted as a function of β_d and v_d in the RFT model (Figure 5.12). Specifically, we fit the magnitude of reaction force, defined as $F_t(\beta_d = 0)$, as a quadratic function of v_d (Figure 5.5). Then we fit the normalized reaction force, $F_t/F_t(\beta_d = 0)$ and $F_n/F_t(\beta_d = 0)$ as a sinusoidal function of β_d:

$$\begin{aligned} F_t &= C_1 v_d^2 \cos(\beta_d), \\ F_n &= C_2 v_d^2 \sin(\beta_d). \end{aligned} \tag{5.1}$$

As stated above, RFT assumes that forces along a deforming body are decoupled. Therefore, the swimmer can be divided into 14 independent segments. Further, in dissipation-dominated environments where inertial forces are negligible, the net force on a body is zero at every moment in time, giving

$$\boldsymbol{F} = \sum_{i=1}^{14} (\boldsymbol{F}_n^{[i]} + \boldsymbol{F}_t^{[i]}) = 0, \tag{5.2}$$

where $\boldsymbol{F}_n^{[i]}$ and $\boldsymbol{F}_t^{[i]}$ are normal and tangential force on i-th element, respectively. We calculate BL/cyc as a function of mean relative curvature ($\kappa_m \lambda_s$, Figure 5.7). We hypothesize the animals preferentially use direct body waves, requiring no modulation of the limb-stepping pattern for propulsion. However, other centipede species modulate their body [229] and limb [67, 63, 101] dynamics upon changes in their environment. Thus, as observed in amphibious centipedes [229], we extended the predictions to the case where the centipede uses a retrograde body wave (the chirality of the PC projections, Figure 5.7B) with limbs folded towards the body. For direct waves, we assume forces act on the limbs (due to extended limbs). For retrograde waves, we assume forces act on the body segments (Figure 5.7C(i)-(ii)). Further, we compared across experimentally resolved and different F_n/F_t and limb

posturing for both direct and retrograde waves in simulations. Direct waves with folded limbs and retrograde waves with extended limbs lead to backward motion, and thus were not included in the comparison (Figure 5.13).

For direct waves, we obtained good agreement using experimentally resolved forces ($F_n/F_t = 0.75$) between RFT predictions and the animal's performance (BL/cyc = 0.22 ± 0.03, $\kappa_m/\lambda_s = 8.54 \pm 1.76$) (Figure 5.7D). This suggests that, as hypothesized, $F_n/F_t \leq 1$ emerges due to the centipede's morphology (i.e., limbs oriented perpendicular to the body). If *Li. forficatus* changed its body profile during swimming, the animal would have achieved backward displacement using a direct body wave (Figure 5.13). Thus, while the limbs did not contribute to propulsion, they modulated the animal's drag anisotropy ratio. Further, for experimentally obtained and varied F_n/F_t, RFT predicts increasing BL/cyc with increasing κ_m/λ_s, decreasing at approximately $\kappa_m\lambda_s$ = 11.

For theoretical retrograde waves with folded limbs, performance also increased with increasing $\kappa_m\lambda_s$, decreasing at approximately $\kappa_m\lambda_s$ = 10. However, independent of F_n/F_t, a direct wave with extended limbs achieved greater or comparable performance. Thus, the centipedes use the behavior that guarantees a high swimming performance, potentially desirable to contend with external perturbations (e.g., high waters [248]). Moreover, using direct body waves may simplify the animal's neuromechanical control. Specifically, forward motion using retrograde waves requires a change in both the limb behavior and the body wave propagation direction. In contrast, a direct limb-stepping pattern requires only the addition of direct body waves for propulsion.

While drag measurements were performed for the case without limb oscillation ($\theta_{max} = 0°$), the centipedes oscillate their limbs with $\theta_{max} = 34.2 \pm 7.5°$. This affects at what $\kappa_m\lambda_s$ limb-limb (*L-L*) and limb-body (*L-B*) intersections occur (Figure 5.7D). When $\theta_{max} = 0°$, *L-L* and *L-B* intersections occurred at $\kappa_m\lambda_s \geq$ 5.9 and 11.3, respectively. In contrast, when $\theta_{max} = 34°$, *L-L* and *L-B* intersections occurred at $\kappa_m\lambda_s \geq$ 8.7 and 11.5, respectively. While limb oscillations may not contribute to propulsion, $\theta_{max} = 34°$ facilitates greater

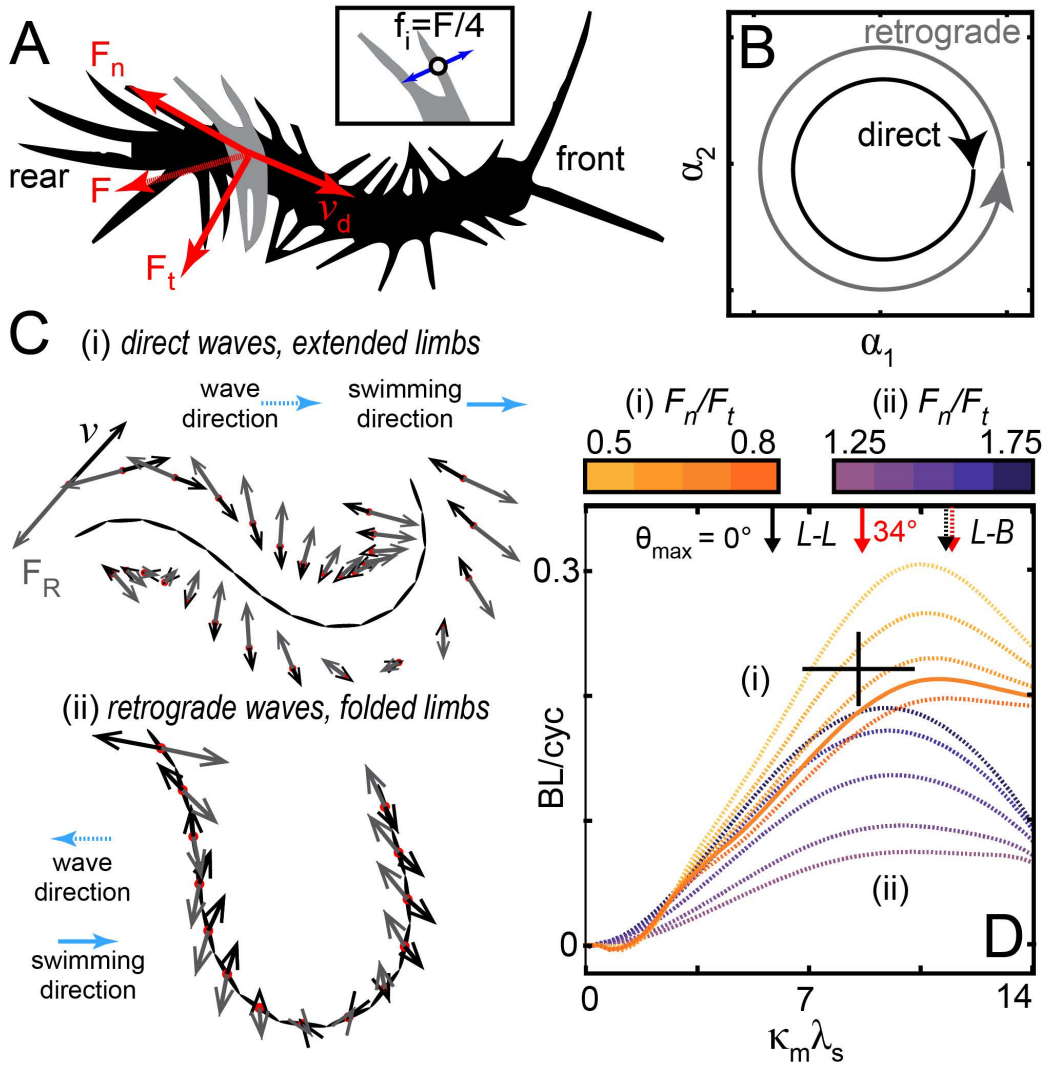

Figure 5.7: **Resistive Force Theory predictions.** (A) Diagram of centipede and forces (red arrows, v_d, F_n, F_t, F) acting on a segment (gray shaded region). Inset shows forces (blue arrows, f_i) acting on the mid-point (white circle) of each limb (i). (B) Diagram of projections of PCs. Black and gray curves (offset for clarity) correspond to a clockwise (direct) and counter-clockwise (retrograde) trajectory, respectively. (C) Force diagrams obtained from RFT for (i) direct waves with extended limbs and (ii) retrograde waves with folded limbs. Black and gray arrows correspond to velocity (v) and reaction forces (F_R), respectively. Solid and dashed blue arrows correspond to the swimming direction (direction of motion) and the wave direction (body wave propagation), respectively. (D) RFT prediction of BL/cyc with $\kappa_m \lambda_s$ for C(i) (orange) and C(ii) (purple). Solid orange curve corresponds to experimentally obtained $F_n/F_t = 0.75$. Black cross corresponds to animal performance. Arrows highlight $\kappa_m \lambda_s$ values where *L-L* (black) and *L-B* (red), for $\theta_{max} = 0°$ (solid) and 34°(dashed).

body bends and reduces emergent collisions. We observed *L-L* intersections in the centipedes primarily occurring at the limb tip. *L-L* intersections were accompanied by local deformation of the limb shape (i.e., limb bending). Further, no *L-B* intersection was observed in the centipedes. We posit limb oscillations allow the animals to function at the limit of achievable body bends, without introducing *L-B* collisions, detrimental for propulsion.

Although an RFT framework has not been previously utilized for locomotion at the interface, recent work has demonstrated that the effectiveness of RFT depends on the governing equations of the medium [74]. When the governing partial differential equations (PDEs) are hyperbolic (e.g., granular media [78, 79, 35, 37]), stresses are localized and can be attributed to the motion of specific body elements [74]. In contrast, when the PDEs are elliptic (e.g., viscous fluids), the stresses in any segment can depend on the entire boundary [74] and accurate modeling of in locomotion must be augmented by more sophisticated approaches [249]. The fact that the RFT approach functions well in the centipede surface swimming is in accord with the hyperbolic character of equations that describe surface waves [250].

5.7 Conclusion

We performed the first centipede locomotion experiments and drag measurements at the air-water interface. We measured the body kinematics of *Li. forficatus* swimming at the surface. Specifically, we discovered this environment generalist centipede uses direct body waves for propulsion. We posit the centipede's ability to generate motion via direct body waves emerged due to selective pressures from habitats (e.g., floodplains) where they must contend with high waters to survive [248]. Inspired by RFT used to model hispid flagella in microorganisms, we hypothesized centipedes generated motion using direct waves due to their experienced drag anisotropy ($F_n/F_t < 1$) resulting from their splayed limbs. We performed water surface drag experiments and found that for $F_n/F_t \leq 1$ for the centipede's

angles of attack. We developed new surface wave RFT at the interface, using experimentally measured empirical force relations. Surface wave RFT predictions in which wave drag dominates inertia captured swimming speed and revealed that direct waves with extended limbs yields comparable or greater performance to retrograde waves with folded limbs (observed in amphibious centipedes [229]). We posit the addition of direct body waves to the limb-stepping pattern simplifies the animal's neuromechanical control when contending with multiple environments. We expect future multilegged robots with variable limb orientation can use principles found here to modulate F_n/F_t and maneuver across both terrestrial and fluid environments, augmenting the navigation capabilities of existing multilegged robots in diverse natural terrains [208, 214].

5.8 Contributions

The contributions for the project are detailed as follows:

Kelimar Diaz performed animal experiments and tracking, designed and performed drag experiments, analyzed and processed the data. Steven Tarr assisted animal experiments and performed surface wave reconstruction. Baxi Chong performed RFT simulations. Kelimar Diaz, Steven Tarr, Baxi Chong, and Daniel I. Goldman conceived the study and interpreted the results. Kelimar Diaz, Steven Tarr, and Baxi Chong co-wrote the original manuscript [102]. Daniel I. Goldman supervised the project, provided comments on and modified the original manuscript [102].

5.9 Appendix

5.9.1 Animals

Centipedes were wild caught from Cuyahoga County, Ohio. Each centipede was individually housed in a plastic container on a 12 hr:12 hr L:D photoperiod at room temperature (20-22° C). Centipedes were provided a source of water and fed mealworms biweekly.

5.9.2 Reflection based drag measurement apparatus

The drag apparatus consisted of a model segment, a laser, and a camera (Figure 5.8). The model centipede segment was attached to a thin beam (0.25 mm thick aluminum, McMaster-Carr, 9708K51). The laser was reflected off the thin beam and a camera (Basler, acA1300-200um) recorded the laser spot to obtain beam deflection. The centroid of the laser was obtained by finding the global maximum pixel intensity for each frame using a custom MATLAB code (Figure 5.10A). Steady state force was resolved from laser centroid displacement by calibrating the beam to objects of known mass (0.01 g, 0.05 g, and 0.1 g, Figure 5.9. Figure 5.9B) shows example drag measurement obtained from apparatus for $\beta_d = 60^\circ$ at $v_d = 11.25$cm/s. Example trials for all β_d and varying v_d can be found in Figure 5.11.

5.9.3 Synthetic Schlieren imaging

Before starting the experiments, we captured a reference image of the background pattern (checkerboard) as seen through a still free (i.e., unperturbed) surface with the high speed camera. During experiments, surface waves created by the swimming centipedes appeared as a distortion field $\vec{u}$ applied to the checkerboard. We compared the spatial Fourier transform of the distorted checkerboard to that of the reference image to find how the carrier peaks were modulated. When the free surface curvature had focal length greater than the distance to the background pattern (i.e., the invertibility condition is met [244]) we filtered the modulated signal to extract $\vec{u}(\vec{r}, t)$, which is proportional to the gradient of the free surface height. Moisy and colleagues [244] quantify this invertibility condition as follows:

$$h_p < h_{p,c} = \frac{\lambda^2}{4\pi^2 \alpha \eta_0}, \tag{5.3}$$

where h_p is the effective surface-pattern distance, $h_{p,c}$ is the free surface focal length, λ is the wavelength, α is the ratio of indices of refraction given by $1 - n_{air}/n_{fluid}$, and η_0

is the wave amplitude [244]. Further, We adapted the open-source code in [246] for use with our apparatus (Figure 5.4A), incorporating both a scale factor to account for additional interfaces between the background pattern and the fluid free surface [244].

Quantitatively identifying where the invertibility condition fails requires knowledge of wave properties that are not known a priori and cannot be reliably obtained from the reconstruction itself. However, we note that failed reconstruction surface height data typically is highly discontinuous, both with itself and with successfully reconstructed surface heights. We used this characteristic to estimate regions where the reconstruction failed per video frame with an autocorrelation method described by the following steps:

1. Perform a 2D spatially-moving variance with square kernel given by the 8-way nearest pixel neighbors.
2. Compare the moving variance to a threshold value. We obtained our threshold through trial-and-error but postulate that it is related to the effective distance between the free surface and background pattern.
3. Convert any pixels for which the variance exceeds the threshold to a mask.
4. Perform minor cleanup on the mask using morphological operations. The result is an estimate of all failed surface reconstructions in the frame.

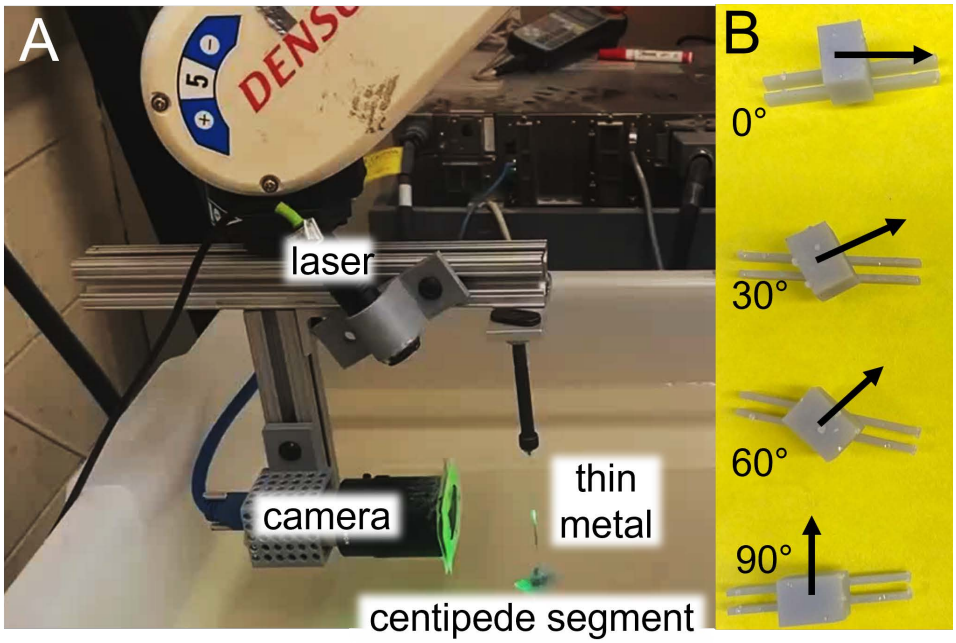

Figure 5.8: **Reflection based drag measurement apparatus.** (A) Image of experimental apparatus, consisting of a thin metal beam, a laser, and a camera. (B) Resin printed centipede segments for (from top to bottom) $\beta_d = 90, 60, 30,$ and $0°$.

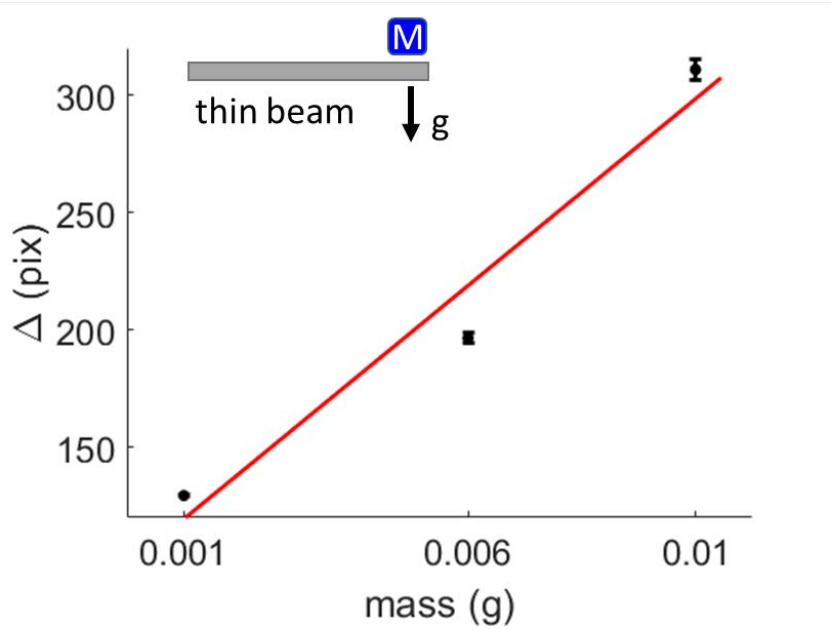

Figure 5.9: **Beam calibration to obtain forces.** Pixel displacement as a function of mass. The thin metal beam was placed horizontally and calibrated with objects of known mass (M) to resolves forces from laser spot displacement (inset). Points were well fit (red line) by a linear function ($y = mx + b$, $R^2 = 0.96$), where the slope ($m = 19,890$) corresponds to the calibration factor.

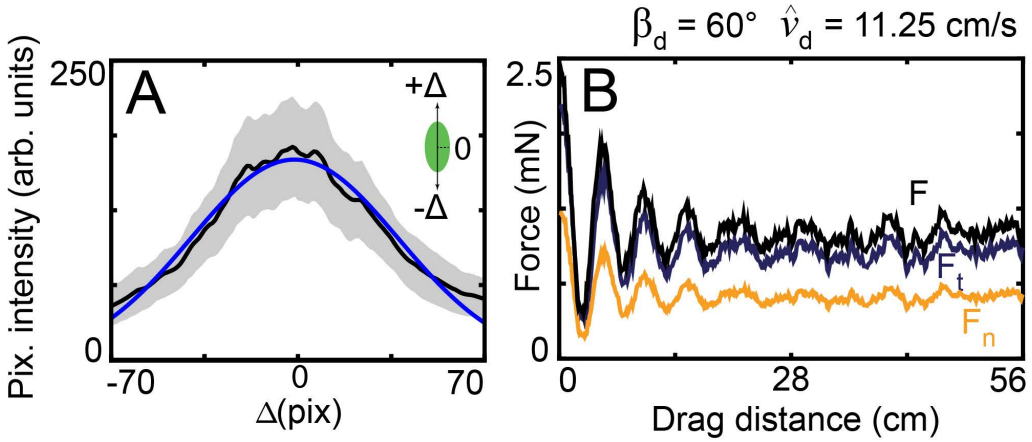

Figure 5.10: **Raw data obtained from drag measurements.** (A) Measured pixel intensity along the long axis of the laser spot. Blue curve corresponds to a fitted Gaussian. (B) Raw force measurement (black) obtained from drag experiments for $\beta_d = 60°$ at v_d = 11.25 cm/s. Yellow and blue line correspond to forces along the normal and tangential direction of the model centipede segment, respectively.

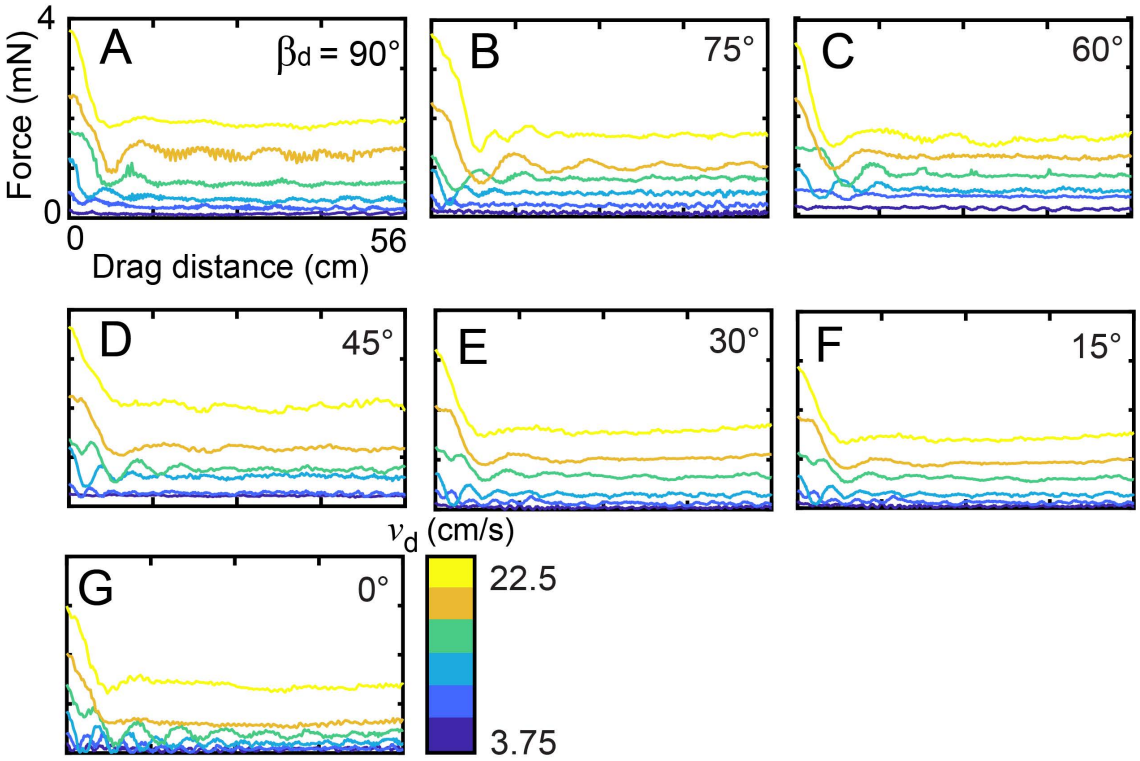

Figure 5.11: **Raw experimentally obtained drag forces.** Example drag measurement obtained from experiments for $\beta_d =$ A) 90°, B) 75°, C) 60°, D) 45°, E) 30°, F) 15°, and G) 0° with varying v_d. Colors corresponds to v_d. All axis are equal.

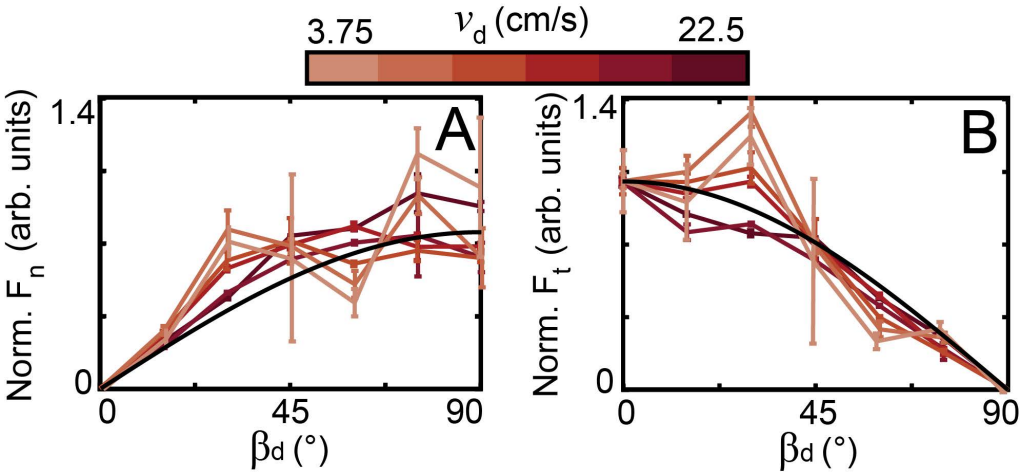

Figure 5.12: **Force decomposition fits.** Normalized (by $F_t(\beta_d = 0)$) (A) F_n and (B) F_t as a function of β_d for varying v_d. Solid black lines correspond to sine and cosine fits for Fn and F_t, respectively.

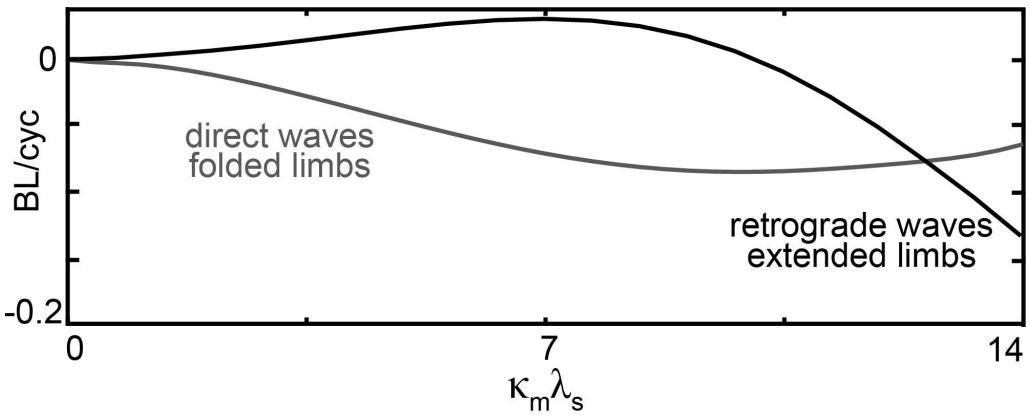

Figure 5.13: **Surface wave RFT for varied limb posturing.** RFT predictions of swimming performance for direct waves with folded limbs (gray line) and retrograde waves with extended limbs (black line).

CHAPTER 6
CONCLUSION AND FUTURE WORK

6.1 Conclusion

In this dissertation, we studied undulatory locomotion in three distinct systems unified by high damping. For each of these systems, the ability to exhibit a behavior (i.e., forward motion and turning) depends on the proper coordination of the body segments and/or appendages. Using a combination of experiments, theoretical models, and robophysical modeling, we broadened our understanding across all of these systems.

In Chapter 2, we extended dimensionality reduction techniques and a geometric framework (in collaboration with Baxi Chong) to turning behaviors (i.e., small-angled turns, omega turns) in *Cae. elegas* laboratory environments (agar and fluid). On agar, we found that turning behaviors can be described as a single behavior; these are controlled by a superposition of two traveling waves, a turning and traveling wave, where modulations of the amplitude of the turning wave lead to different turning rates and consequently turning behaviors. In fluids, dimensionality reduction did not capture superimposed traveling waves, due to indistinguishable spatial frequencies between the turning and the forward wave. However, a single traveling wave with both amplitude and phase modulation are sufficient to model the animal's turning behaviors. Our work suggests that the underlying neural dynamics involve the superposition of muscular excitation waves from independent oscillatory neural circuits in *Cae. elegans*.

In Chapter 3, we studied quadriflagellate gait coordination and hydrodynamic performance. To the best of our knowledge, we developed the first free self-propelling, macroscopic robophysical model of a quadriflagellate algae swimming in a low Reynolds environments. Then, we prescribed gaits observed in distinct alga species - the pronk, the

trot, and the gallop (clockwise and counterclockwise in our robot). Further, we varied the relative orientation of the flagella. We found that hydrodynamic performance (in terms of body length per gait cycle) was sensitive to both appendage orientation and swimming gait. In addition, we captured what we observed in the algae, the trot gait achieved the greatest hydrodynamic performance by having a greater resistance backward displacement during the recovery stroke. We posit that distinct gaits arose in each algae species due to selective pressures (e.g., availability of nutrients), where distinct locomotive strategies are advantageous for specific ecology.

In Chapter 4, we performed a comparative study of centipedes with distinct limb and body dynamics, *Scd. polymorpha* and *Scc. sexspinosus*, locomoting on model rugose terrains. Experiments revealed that both centipede species potentially leveraged the inherent physiology of their limbs to negotiate limb-terrain collisions. For *Scc. sexspinosus*, we found that this animal changed its limb-stepping pattern with terrain rugosity; when this centipede locomoted on the rugose terrains in changed the direction the limb-stepping pattern was propagated from direct (with the direction of motion) to retrograde (opposite to the direction of motion). We hypothesize that gait change allowed the centipede to reduce the uncertainty in finding a secure foothold.

In Chapter 5, we studied the swimming dynamics of a surface swimming centipede, *Li. forficatus*. We found that, instead of using primarily its limbs, this centipede relied on direct body waves (with the direction of motion, towards the head) to generate self-propulsion. We sought to understand how this animal achieved forward propulsion with the use of direct body undulation. A surface wave reconstruction technique revealed that the centipede emitted waves during locomotion, which we posit carried dissipated energy from the system. Inspired by hispid flagella in microorganisms, we adopted a surface wave RFT approach and performed the first drag measurements at the air-water interface. Experiments revealed that the animal's morphology modulates the forces that a segment experiences; due to the extended limbs drag forces in the forward/backward direction (normal forces) were greater

then those in the lateral direction (tangential forces), enabling forward motion with direct waves. We developed a surface wave RFT using experimentally resolved forces and found that theoretical predictions captured the centipede's performance. Further, surface wave RFT showed that the animals are using the strategy that achieves the greatest swimming speed, while reducing the complexity of the neuromechanical control.

6.2 Future Work

6.2.1 *Cae. elegans* turning strategies in model complex terrains

In Chapter 2, we present a study of worm turning in homogeneous laboratory environments. We hypothesize that the ability to vary turning rate via amplitude modulation is a robust strategy for complex, heterogeneous environments. Future work can explore turning in various laboratory model heterogeneous environments such as lattices. Preliminary experiments in lattices suggest that, omega turns in particular, are may be advantageous in confined spaces where collisions might be undesirable. Moreover, inspired by our observation in *Cae. elegans* (superimposed forward and turning wave), previous work has shown that in robophysical models omega turns are robust to various external perturbations [117]. However, further investigation is required to understand how do these worms maneuver and turn in other heterogeneous environments (e.g., models of rotten fruits, fluids of various viscosities, wet granular media), providing insight to how these animals navigate their natural environments.

6.2.2 Fluid flow as a function of swimming gait

In Chapter 3, we show that distinct gaits can lead to different performance on algae species that are closely related and/or share similar morphology. The respective gait of each species potentially arose from selective pressures related to their environments. Thus, we posit that species that use the trot gait rely more on phototaxis for photosynthesis, whereas the species that use the pronk and the gallop rely on mixing the surrounding media for nutrient

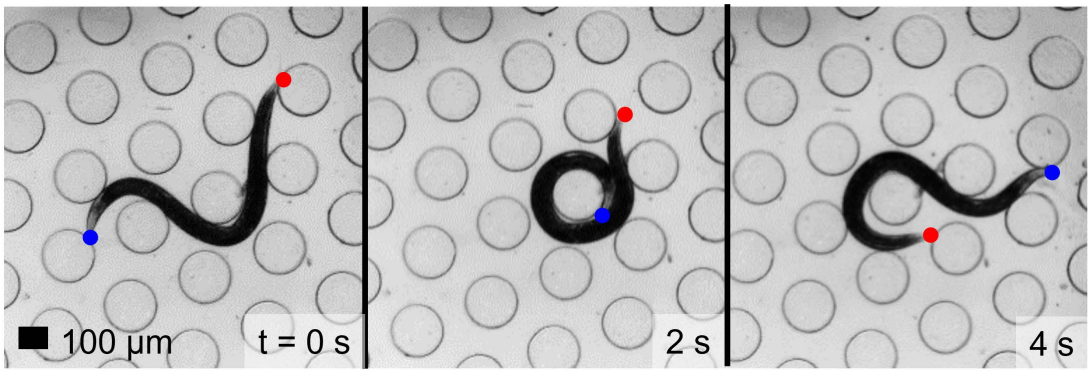

Figure 6.1: **Omega turns in heterogeneous terrains.** *Cae. elegans* performing an omega turn in a dense lattice. Blue and red circle highlight the head and tail, respectively.

acquisition.

Future work can study how flow fields arise from distinct gaits in three dimensions. Using three dimensional Particle Image Velocimetry (PIV) [251] can lead to insightful studies, extending from the currently developed robophysical model. We hypothesize that a trotting gait will have flows that generate thrust opposite to the direction of motion. Moreover, we hypothesize that both a pronking and galloping gait flows will lead to a combination of similar thrust generation (as there is forward progression) with additional vortex-like structures that moves particles towards the cell body. Preliminary experiments (performed by Ellen Liu) in a biflagellate robophysical model show that symmetric and asymmetric gaits lead to distinct fluid flows.

6.2.3 Three dimensional motion of centipede

In Chapter 4, we performed a comparative study of two centipede species traversing rugose terrains. As discussed, we observed three dimensional contributions on, not only the rugose terrains but also, flat, homogeneous terrain (Figure 6.2). Three dimensional motion of the centipedes is reminiscent of the sidewinders (*Cr. cerastes* [51, 40]) vertical wave, where presumably the limbs move the body up and down during locomotion. Thus, future work can study three dimensional locomotion of centipedes a behavior that might be general

across order but, to the best of our knowledge, has not been previously discovered.

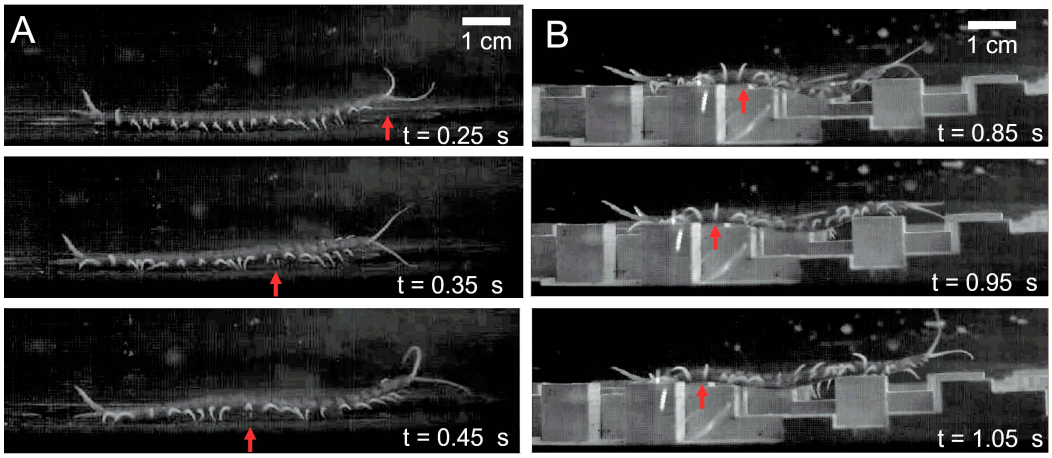

Figure 6.2: **Three dimensional motion of centipedes.** Example vertical lifting of *Scd. polymorpha* on (A) flat and (B) less rugose terrain. Red arrows denote segments that show pronounced lifting. Centipede moves from left to right.

6.2.4 Physics of surface wave-drag

In Chapter 5, we report a surface swimmer (*Li. forficatus*) that can achieve a drag anisotropy less than one due to its morphology (slender body and extended limbs). We posit the centipede locomotes in a wave-drag dominated regime, instead of viscous or friction dominated. Further, the effectiveness of RFT, as discussed, suggests the force flow/fields are hyperlocalized (i.e., independent for each segment). However, we do not fully understand the physics of this wave-drag dominated regime, in which we posit damping emerges from energy being carried away by the surface waves towards the boundary. Future work can develop a cm-scale robophysical model and fully develop a surface wave-drag RFT framework. Further, extended drag experiments varying parameters such as leg length and number of leg pairs may elucidate some of the unknowns at the air-water interface.

REFERENCES

[1] R. Alexander, *Principles of animal locomotion*. Princeton University Press, 2003.

[2] N. Cohen and J. H. Boyle, "Swimming at low Reynolds number: A beginners guide to undulatory locomotion," *Contemporary Physics*, vol. 51, no. 2, pp. 103–123, Mar. 2010.

[3] D. Woolley and G. Vernon, "A study of helical and planar waves on sea urchin sperm flagella, with a theory of how they are generated," *Journal of Experimental Biology*, vol. 204, no. 7, pp. 1333–1345, 2001.

[4] K. Y. Wan, "Synchrony and symmetry-breaking in active flagellar coordination," *Philosophical Transactions of the Royal Society B-biological Sciences*, vol. 375, no. 1792, p. 20 190 393, Feb. 2020.

[5] S. Berri, J. Boyle, M. Tassieri, I. Hope, and N. Cohen, "Forward locomotion of the nematode c. elegans is achieved through modulation of a single gait," *HFSP journal*, vol. 3, no. 3, pp. 186–193, 2009.

[6] L. Frézal and M. Félix, "The natural history of model organisms: C. elegans outside the petri dish," *elife*, vol. 4, e05849, 2015.

[7] C. Fang-Yen *et al.*, "Biomechanical analysis of gait adaptation in the nematode caenorhabditis elegans," *Proceedings of the National Academy of Sciences*, vol. 107, no. 47, pp. 20 323–20 328, 2010.

[8] G. Stephens, B. Johnson-Kerner, W. Bialek, and W. Ryu, "Dimensionality and dynamics in the behavior of *C. elegans*," *PLoS computational biology*, vol. 4, no. 4, e1000028, 2008.

[9] S. Park, H. Hwang, S. Nam, F. Martinez, R. Austin, and W. Ryu, "Enhanced caenorhabditis elegans locomotion in a structured microfluidic environment," *PloS one*, vol. 3, no. 6, e2550, 2008.

[10] T. Majmudar, E. Keaveny, J. Zhang, and M. Shelley, "Experiments and theory of undulatory locomotion in a simple structured medium," *Journal of the Royal Society Interface*, vol. 9, no. 73, pp. 1809–1823, 2012.

[11] E. Tytell and G. Lauder, "The hydrodynamics of eel swimming: I. wake structure," *Journal of Experimental Biology*, vol. 207, no. 11, pp. 1825–1841, 2004.

[12] E. Tytell, C. Hsu, T. Williams, A. Cohen, and L. Fauci, "Interactions between internal forces, body stiffness, and fluid environment in a neuromechanical model of

lamprey swimming," *Proceedings of the National Academy of Sciences*, vol. 107, no. 46, pp. 19 832–19 837, 2010.

[13] M. Sfakiotakis, D. Lane, and J. Davies, "Review of fish swimming modes for aquatic locomotion," *IEEE Journal of oceanic engineering*, vol. 24, no. 2, pp. 237–252, 1999.

[14] P. Moreno-Colom, S. Ten, J. Raga, and F. Aznar, "Spatial distribution and aggregation of xenobalanus globicipitis on the flukes of striped dolphins, stenella coeruleoalba: An indicator of host hydrodynamics?" *Marine Mammal Science*, vol. 36, no. 3, pp. 897–914, 2020.

[15] B. Chong, T. Wang, E. Erickson, P. Bergmann, and D. Goldman, "Coordinating tiny limbs and long bodies: Geometric mechanics of lizard terrestrial swimming," *Proceedings of the National Academy of Sciences*, vol. 119, no. 27, e2118456119, 2022.

[16] S. Daan and T. Belterman, "Lateral bending in locomotion of some lower tetrapods. i.. 2.," *Proceedings Of The Koninklijke Nederlandse Akademie Van Wetenschappen Series C-Biological And Medical Sciences*, vol. 71, no. 3, pp. 245–+, 1968.

[17] J. Edwards, "The evolution of terrestrial locomotion," in *Major patterns in vertebrate evolution*, Springer, 1977, pp. 553–577.

[18] R. Ritter, "Lateral bending during lizard locomotion," *Journal of Experimental Biology*, vol. 173, no. 1, pp. 1–10, 1992.

[19] S. Reilly and M. Delancey, "Sprawling locomotion in the lizard sceloporus clarkii: The effects of speed on gait, hindlimb kinematics, and axial bending during walking," *Journal of Zoology*, vol. 243, no. 2, pp. 417–433, 1997.

[20] S. Manton, *The Arthropoda: habits, functional morphology and evolution*. 1977.

[21] B. Anderson, J. Shultz, and B. Jayne, "Axial kinematics and muscle activity during terrestrial locomotion of the centipede scolopendra heros," *The Journal of experimental biology*, vol. 198, no. 5, pp. 1185–1195, 1995.

[22] D. Murphy, D. Webster, S. Kawaguchi, R. King, and J. Yen, "Metachronal swimming in antarctic krill: Gait kinematics and system design," *Marine biology*, vol. 158, no. 11, pp. 2541–2554, 2011.

[23] M. Byron *et al.*, "Metachronal motion across scales: Current challenges and future directions," *Integrative and comparative biology*, vol. 61, no. 5, pp. 1674–1688, 2021.

[24] A. Garcia, G. Krummel, and S. Priya, "Fundamental understanding of millipede morphology and locomotion dynamics," *Bioinspiration & Biomimetics*, vol. 16, no. 2, p. 026 003, 2020.

[25] S. Manton, "The evolution of arthropodan locomotory mechanisms.—part 4. the structure, habits and evolution of the diplopoda," *Zoological Journal of the Linnean Society*, vol. 42, no. 286, pp. 299–368, 1954.

[26] K. Y. Wan and R. E. Goldstein, "Coordinated beating of algal flagella is mediated by basal coupling," *Proceedings of the National Academy of Sciences of the United States of America*, vol. 113, no. 20, E2784–E2793, May 2016.

[27] G. Lauder, E. Anderson, J. Tangorra, and P. Madden, "Fish biorobotics: Kinematics and hydrodynamics of self-propulsion," *Journal of experimental biology*, vol. 210, no. 16, pp. 2767–2780, 2007.

[28] K. Y. Wan and R. E. Goldstein, "Time Irreversibility and Criticality in the Motility of a Flagellate Microorganism," *Physical Review Letters*, vol. 121, no. 5, p. 058 103, Aug. 2018.

[29] M. Sfakiotakis, D. Lane, and J. Davies, "Review of fish swimming modes for aquatic locomotion," *IEEE Journal of oceanic engineering*, vol. 24, no. 2, pp. 237–252, 1999.

[30] R. Tyson, C. E. Jordan, and J. Hebert, "Modelling anguilliform swimming at intermediate reynolds number: A review and a novel extension of immersed boundary method applications," *Computer methods in applied mechanics and engineering*, vol. 197, no. 25-28, pp. 2105–2118, 2008.

[31] A. Ijspeert, A. Crespi, D. Ryczko, and J. Cabelguen, "From swimming to walking with a salamander robot driven by a spinal cord model," *science*, vol. 315, no. 5817, pp. 1416–1420, 2007.

[32] G. Lauder and E. Tytell, "Hydrodynamics of undulatory propulsion," *Fish physiology*, vol. 23, pp. 425–468, 2005.

[33] G. Lauder, P. Madden, R. Mittal, H. Dong, and M. Bozkurttas, "Locomotion with flexible propulsors: I. experimental analysis of pectoral fin swimming in sunfish," *Bioinspiration & biomimetics*, vol. 1, no. 4, S25, 2006.

[34] B. Jayne, "Muscular mechanisms of snake locomotion: An electromyographic study of the sidewinding and concertina modes of crotalus cerastes, nerodia fasciata and elaphe obsoleta," *Journal of Experimental Biology*, vol. 140, no. 1, pp. 1–33, 1988.

[35] S. Sharpe *et al.*, "Locomotor benefits of being a slender and slick sand swimmer," *Journal of Experimental Biology*, vol. 218, no. 3, pp. 440–450, 2015.

[36] P. Schiebel, J. Rieser, A. Hubbard, L. Chen, D. Rocklin, and D. Goldman, "Mechanical diffraction reveals the role of passive dynamics in a slithering snake," *Proceedings of the National Academy of Sciences*, vol. 116, no. 11, pp. 4798–4803, 2019.

[37] P. Schiebel *et al.*, "Mitigating memory effects during undulatory locomotion on hysteretic materials," *Elife*, vol. 9, e51412, 2020.

[38] P. Schiebel, A. Hubbard, and D. Goldman, "Comparative study of snake lateral undulation kinematics in model heterogeneous terrain," *Integrative and Comparative Biology*, 2020.

[39] J. Rieser *et al.*, "Geometric phase and dimensionality reduction in locomoting living systems," *arXiv preprint arXiv:1906.11374*, 2019.

[40] H. C. Astley *et al.*, "Surprising simplicities and syntheses in limbless self-propulsion in sand," *The Journal of Experimental Biology*, vol. 223, no. 5, jeb103564, Mar. 2020.

[41] J. Gray, "The movement of sea-urchin spermatozoa," *Journal of Experimental Biology*, vol. 32, no. 4, pp. 775–801, 1955.

[42] E. Gillies, R. Cannon, R. Green, and A. Pacey, "Hydrodynamic propulsion of human sperm," *Journal of Fluid Mechanics*, vol. 625, pp. 445–474, 2009.

[43] K. Diaz, T. L. Robinson, Y. O. Aydin, E. Aydin, D. I. Goldman, and K. Y. Wan, "A minimal robophysical model of quadriflagellate self-propulsion," *Bioinspiration & Biomimetics*, vol. 16, no. 6, p. 066 001, 2021.

[44] K. Y. Wan and G. Jékely, "Origins of eukaryotic excitability," *Philosophical Transactions of the Royal Society B-biological Sciences*, vol. 376, p. 20 190 758, 2021.

[45] K. Ehlers, A. Samuel, H. Berg, and R. Montgomery, "Do cyanobacteria swim using traveling surface waves?" *Proceedings of the National Academy of Sciences*, vol. 93, no. 16, pp. 8340–8343, 1996.

[46] P. I. Server, *Cyanothece*, [Online; accessed November 11, 2022], 2005.

[47] T. Zhang and D. I. Goldman, "The effectiveness of resistive force theory in granular locomotion," *Physics of Fluids*, vol. 26, no. 10, p. 101 308, Oct. 2014.

[48] J. Tomie, D. Cairns, and S. Courtenay, "How american eels anguilla rostrata construct and respire in burrows," *Aquatic Biology*, vol. 19, no. 3, pp. 287–296, 2013.

[49] G. Gillis, "Environmental effects on undulatory locomotion in the american eel anguilla rostrata: Kinematics in water and on land," *Journal of Experimental Biology*, vol. 201, no. 7, pp. 949–961, 1998.

[50] J. Videler and P. Kamermans, "Differences between upstroke and downstroke in swimming dolphins," *Journal of Experimental Biology*, vol. 119, no. 1, pp. 265–274, 1985.

[51] H. Astley *et al.*, "Modulation of orthogonal body waves enables high maneuverability in sidewinding locomotion," *Proceedings of the National Academy of Sciences*, vol. 112, no. 19, pp. 6200–6205, 2015.

[52] B. Jayne, "Swimming in constricting (elaphe g. guttata) and nonconstricting (nerodia fasciata pictiventris) colubrid snakes," *Copeia*, pp. 195–208, 1985.

[53] K. Kelley, S. Arnold, and J. Gladstone, "The effects of substrate and vertebral number on locomotion in the garter snake thamnophis elegans," *Functional Ecology*, vol. 11, no. 2, pp. 189–198, 1997.

[54] C. Gans, "Tetrapod limblessness: Evolution and functional corollaries," *American Zoologist*, vol. 15, no. 2, pp. 455–467, 1975.

[55] S. Manton, "The evolution of arthopodan locomotory mechanisms - part 3. the locomotion of *Chilopoda* and *Pauropoda*.," *Zoological Journal of the Linnean Society*, vol. 42, no. 284, pp. 118–167, 1952.

[56] M. Ford, H. Lai, M. Samaee, and A. Santhanakrishnan, "Hydrodynamics of metachronal paddling: Effects of varying reynolds number and phase lag," *Royal Society open science*, vol. 6, no. 10, p. 191 387, 2019.

[57] S. Alben, K. Spears, S. Garth, D. Murphy, and J. Yen, "Coordination of multiple appendages in drag-based swimming," *Journal of The Royal Society Interface*, vol. 7, no. 52, pp. 1545–1557, 2010.

[58] M. Ford and A. Santhanakrishnan, "On the role of phase lag in multi-appendage metachronal swimming of euphausiids," *Bioinspiration & Biomimetics*, vol. 16, no. 6, p. 066 007, 2021.

[59] S. Khaderi, J. Den Toonder, and P. Onck, "Fluid flow due to collective non-reciprocal motion of symmetrically-beating artificial cilia," *Biomicrofluidics*, vol. 6, no. 1, p. 014 106, 2012.

[60] Y. Ding, J. Nawroth, M. McFall-Ngai, and E. Kanso, "Mixing and transport by ciliary carpets: A numerical study," *Journal of Fluid Mechanics*, vol. 743, pp. 124–140, 2014.

[61] E. Milana *et al.*, "Metachronal patterns in artificial cilia for low reynolds number fluid propulsion," *Science advances*, vol. 6, no. 49, eabd2508, 2020.

[62] T. E.R. and J. H.D., *Crawling and burrowing Mechanics and Energetics of Animal Locomotion*, A. R.M. and G. G., Eds. London: Chapman and Hall, 1977, pp. 204–221.

[63] S. Kuroda, N. Uchida, and T. Nakagaki, "Gait switching with phase reversal of locomotory waves in the centipede scolopocryptops rubiginosus," *Bioinspiration & Biomimetics*, vol. 17, no. 2, p. 026 005, 2022.

[64] F. Rost, L. Brusch, and A. Oates, "Modelling and analysis of chevron formation in the fish myotome," Ph.D. dissertation, Diplomarbeit. Dresden: Technische Universität Dresden. 72 pp. DOI: 10.5281 …, 2010.

[65] W. Mosauer, "On the locomotion of snakes," *Science*, vol. 76, no. 1982, pp. 583–585, 1932.

[66] M. Holwill and P. Peters, "Dynamics of the hispid flagellum of ochromonas danica: The role of mastigonemes," *Journal of Cell Biology*, vol. 62, no. 2, pp. 322–328, 1974.

[67] S. Kuroda, I. Kunita, Y. Tanaka, A. Ishiguro, R. Kobayashi, and T. Nakagaki, "Common mechanics of mode switching in locomotion of limbless and legged animals," *Journal of the Royal Society interface*, vol. 11, no. 95, p. 20 140 205, 2014.

[68] G. La Spina, M. Sfakiotakis, D. Tsakiris, A. Menciassi, and P. Dario, "Polychaete-like undulatory robotic locomotion in unstructured substrates," *IEEE Transactions on Robotics*, vol. 23, no. 6, pp. 1200–1212, 2007.

[69] T. Jahn, M. Lanoman, and J. Fonseca, "The mechanism of locomotion of flagellates. ii. function of the mastigonemes of ochromonas," *The Journal of Protozoology*, vol. 11, no. 3, pp. 291–296, 1964.

[70] M. Holwill and M. Sleigh, "Propulsion by hispid flagella," *Journal of Experimental Biology*, vol. 47, no. 2, pp. 267–276, 1967.

[71] J. Gray and G. Hancock, "The propulsion of sea-urchin spermatozoa," *Journal of Experimental Biology*, vol. 32, no. 4, pp. 802–814, 1955.

[72] E. M. Purcell, "Life At Low Reynolds-number," *American Journal of Physics*, vol. 45, no. 1, pp. 3–11, 1977.

[73] R. Johnson and C. Brokaw, "Flagellar hydrodynamics. a comparison between resistive-force theory and slender-body theory," *Biophysical journal*, vol. 25, no. 1, pp. 113–127, 1979.

[74] H. Askari and K. Kamrin, "Intrusion rheology in grains and other flowable materials," *Nature materials*, vol. 15, no. 12, pp. 1274–1279, 2016.

[75] L. Becker, S. Koehler, and H. Stone, "On self-propulsion of micro-machines at low reynolds number: Purcell's three-link swimmer," *Journal of fluid mechanics*, vol. 490, pp. 15–35, 2003.

[76] J. Avron, O. Gat, and O. Kenneth, "Optimal swimming at low reynolds numbers," *Physical review letters*, vol. 93, no. 18, p. 186 001, 2004.

[77] D. Crowdy, S. Lee, O. Samson, E. Lauga, and A. Hosoi, "A two-dimensional model of low-reynolds number swimming beneath a free surface," *Journal of Fluid Mechanics*, vol. 681, pp. 24–47, 2011.

[78] R. Maladen, Y. Ding, C. Li, and D. Goldman, "Undulatory swimming in sand: Subsurface locomotion of the sandfish lizard," *science*, vol. 325, no. 5938, pp. 314–318, 2009.

[79] C. Li, T. Zhang, and D. Goldman, "A terradynamics of legged locomotion on granular media," *Science*, vol. 339, no. 6126, pp. 1408–1412, 2013.

[80] K. Autumn *et al.*, "Adhesive force of a single gecko foot-hair," *Nature*, vol. 405, no. 6787, pp. 681–685, 2000.

[81] Y. Tian *et al.*, "Adhesion and friction in gecko toe attachment and detachment," *Proceedings of the National Academy of Sciences*, vol. 103, no. 51, pp. 19 320–19 325, 2006.

[82] D. Santos, M. Spenko, A. Parness, S. Kim, and M. Cutkosky, "Directional adhesion for climbing: Theoretical and practical considerations," *Journal of Adhesion Science and Technology*, vol. 21, no. 12-13, pp. 1317–1341, 2007.

[83] T. Libby *et al.*, "Tail-assisted pitch control in lizards, robots and dinosaurs," *Nature*, vol. 481, no. 7380, pp. 181–184, 2012.

[84] K. Autumn *et al.*, "Evidence for van der waals adhesion in gecko setae," *Proceedings of the National Academy of Sciences*, vol. 99, no. 19, pp. 12 252–12 256, 2002.

[85] S. Kim, M. Spenko, S. Trujillo, V. Heyneman B.and Mattoli, and M. Cutkosky, "Whole body adhesion: Hierarchical, directional and distributed control of adhesive forces for a climbing robot," in *Proceedings 2007 IEEE International Conference on Robotics and Automation*, IEEE, 2007, pp. 1268–1273.

[86] J. Spagna, D. Goldman, P. Lin, D. Koditschek, and R. Full, "Distributed mechanical feedback in arthropods and robots simplifies control of rapid running on challenging terrain," *Bioinspiration & biomimetics*, vol. 2, no. 1, p. 9, 2007.

[87] A. Jusufi, D. Kawano, T. Libby, and R. Full, "Righting and turning in mid-air using appendage inertia: Reptile tails, analytical models and bio-inspired robots," *Bioinspiration & biomimetics*, vol. 5, no. 4, p. 045 001, 2010.

[88] J. Aguilar *et al.*, "A review on locomotion robophysics: The study of movement at the intersection of robotics, soft matter and dynamical systems," *Reports on Progress in Physics*, vol. 79, no. 11, p. 110 001, Nov. 2016.

[89] E. Standen and G. Lauder, "Dorsal and anal fin function in bluegill sunfish lepomis macrochirus: Three-dimensional kinematics during propulsion and maneuvering," *Journal of Experimental Biology*, vol. 208, no. 14, pp. 2753–2763, 2005.

[90] R. Mittal, H. Dong, M. Bozkurttas, G. Lauder, and P. Madden, "Locomotion with flexible propulsors: Ii. computational modeling of pectoral fin swimming in sunfish," *Bioinspiration & biomimetics*, vol. 1, no. 4, S35, 2006.

[91] T. Pereira, J. Shaevitz, and M. Murthy, "Quantifying behavior to understand the brain," *Nature neuroscience*, vol. 23, no. 12, pp. 1537–1549, 2020.

[92] D. Winter, *Biomechanics and motor control of human movement*. John Wiley & Sons, 2009.

[93] O. Maghsoudi, A. Tabrizi, B. Robertson, and A. Spence, "Superpixels based marker tracking vs. hue thresholding in rodent biomechanics application," in *2017 51st Asilomar Conference on Signals, Systems, and Computers*, IEEE, 2017, pp. 209–213.

[94] T. Nath, A. Mathis, A. Chen, A. Patel, M. Bethge, and M. Mathis, "Using deeplabcut for 3d markerless pose estimation across species and behaviors," *Nature protocols*, vol. 14, no. 7, pp. 2152–2176, 2019.

[95] A. Mathis *et al.*, "Deeplabcut: Markerless pose estimation of user-defined body parts with deep learning," *Nature neuroscience*, vol. 21, no. 9, pp. 1281–1289, 2018.

[96] N. Steinmetz, P. Zatka-Haas, M. Carandini, and K. Harris, "Distributed coding of choice, action and engagement across the mouse brain," *Nature*, vol. 576, no. 7786, pp. 266–273, 2019.

[97] A. Del Vecchio *et al.*, "Spinal motoneurons of the human newborn are highly synchronized during leg movements," *Science advances*, vol. 6, no. 47, eabc3916, 2020.

[98] W. Zhang and M. Yartsev, "Correlated neural activity across the brains of socially interacting bats," *Cell*, vol. 178, no. 2, pp. 413–428, 2019.

[99] C. Fang, T. Zhang, H. Zheng, J. Huang, and K. Cuan, "Pose estimation and behavior classification of broiler chickens based on deep neural networks," *Computers and Electronics in Agriculture*, vol. 180, p. 105 863, 2021.

[100] C. Ebbesen and R. Froemke, "Body language signals for rodent social communication," *Current Opinion in Neurobiology*, vol. 68, pp. 91–106, 2021.

[101] K. Diaz, E. Erickson, B. Chong, D. Soto, and D. Goldman, "Active and passive mechanics for rough terrain traversal in centipedes," *bioRxiv*, 2022.

[102] K. Diaz, B. Chong, S. Tarr, E. Erickson, and D. I. Goldman, "Water surface swimming dynamics in lightweight centipedes," *arXiv preprint arXiv:2210.09570*, 2022.

[103] J. Denham, T. Ranner, and N. Cohen, "Signatures of proprioceptive control in caenorhabditis elegans locomotion," *Philosophical Transactions of the Royal Society B: Biological Sciences*, vol. 373, no. 1758, p. 20 180 208, 2018.

[104] C. Johnson, T. Lewis, and R. Guy, "Neuromechanical mechanisms of gait adaptation in c. elegans: Relative roles of neural and mechanical coupling," *SIAM Journal on Applied Dynamical Systems*, vol. 20, no. 2, pp. 1022–1052, 2021.

[105] N. Croll, "Components and patterns in the behaviour of the nematode caenorhabditis elegans," *Journal of zoology*, vol. 176, no. 2, pp. 159–176, 1975.

[106] L. Salvador, F. Bartumeus, S. Levin, and W. Ryu, "Mechanistic analysis of the search behaviour of caenorhabditis elegans," *Journal of The Royal Society Interface*, vol. 11, no. 92, p. 20 131 092, 2014.

[107] O. Broekmans, J. Rodgers, W. Ryu, and G. Stephens, "Resolving coiled shapes reveals new reorientation behaviors in c. elegans," *Elife*, vol. 5, e17227, 2016.

[108] A. Mohammadi, J. Byrne Rodgers, I. Kotera, and W. Ryu, "Behavioral response of caenorhabditis elegansto localized thermal stimuli," *BMC neuroscience*, vol. 14, no. 1, pp. 1–12, 2013.

[109] A. Shapere and F. Wilczek, *Geometric phases in physics*. World scientific, 1989, vol. 5.

[110] B. Chong *et al.*, "Coordination of lateral body bending and leg movements for sprawled posture quadrupedal locomotion," *The International Journal of Robotics Research*, vol. 40, no. 4-5, pp. 747–763, 2021.

[111] C. Gong, D. Goldman, and H. Choset, "Simplifying gait design via shape basis optimization.," in *Robotics: Science and Systems*, Michigan, USA, vol. 655, 2016.

[112] B. Chong *et al.*, "A hierarchical geometric framework to design locomotive gaits for highly articulated robots," in *Robotics: science and systems*, 2019.

[113] B. Chong *et al.*, "Moving sidewinding forward: Optimizing contact patterns for limbless robots via geometric mechanics.," in *Robotics: Science and Systems*, 2021.

[114] B. Chong *et al.*, "A general locomotion control framework for multi-legged locomotors," *Bioinspiration & Biomimetics*, vol. 17, no. 4, p. 046 015, 2022.

[115] R. Hatton, Y. Ding, H. Choset, and D. Goldman, "Geometric visualization of self-propulsion in a complex medium," *Physical review letters*, vol. 110, no. 7, p. 078 101, 2013.

[116] J. Dai, H. Faraji, C. Gong, R. Hatton, D. Goldman, and H. Choset, "Geometric swimming on a granular surface.," in *Robotics: Science and Systems*, 2016, pp. 1–7.

[117] T. Wang *et al.*, "The omega turn: A biologically-inspired turning strategy for elongated limbless robots," in *2020 IEEE/RSJ International Conference on Intelligent Robots and Systems (IROS)*, IEEE, 2020, pp. 7766–7771.

[118] E. Shammas, H. Choset, and A. Rizzi, "Geometric motion planning analysis for two classes of underactuated mechanical systems," *The International Journal of Robotics Research*, vol. 26, no. 10, pp. 1043–1073, 2007.

[119] R. Hatton and H. Choset, "Nonconservativity and noncommutativity in locomotion," *The European Physical Journal Special Topics*, vol. 224, no. 17, pp. 3141–3174, 2015.

[120] C. Gong, Z. Ren, J. Whitman, J. Grover, B. Chong, and H. Choset, "Geometric motion planning for systems with toroidal and cylindrical shape spaces," in *Dynamic Systems and Control Conference*, American Society of Mechanical Engineers, vol. 51913, 2018, V003T32A013.

[121] M. Travers, J. Whitman, P. Schiebel, D. Goldman, and H. Choset, "Shape-based compliance in locomotion.," in *Robotics: Science and Systems*, vol. 12, 2016.

[122] R. M. Alexander, *Principles of Animal Locomotion*, STU - Student edition. Princeton University Press, 2003, ISBN: 9780691126340.

[123] B. Chong *et al.*, "Coordination of back bending and leg movements for quadrupedal locomotion.," in *Robotics: Science and Systems*, vol. 20, 2018.

[124] R. Stocker and J. R. Seymour, "Ecology and Physics of Bacterial Chemotaxis in the Ocean," *Microbiology and Molecular Biology Reviews*, vol. 76, no. 4, pp. 792–812, Dec. 2012.

[125] U. Rüffer and W. Nultsch, "Flagellar coordination in chlamydomonas cells held on micropipettes," *Cell Motility*, vol. 41, no. 4, pp. 297–307, 1998. eprint: https://onlinelibrary.wiley.com/doi/pdf/10.1002/%28SICI%291097-0169%281998%2941%3A4%3C297%3A%3AAID-CM3%3E3.0.CO%3B2-Y.

[126] M. Theers and R. G. Winkler, "Effects of thermal fluctuations and fluid compressibility on hydrodynamic synchronization of microrotors at finite oscillatory Reynolds number: A multiparticle collision dynamics simulation study," *Soft Matter*, vol. 10, no. 32, pp. 5894–5904, Jun. 2014.

[127] M. Beeby, J. L. Ferreira, P. Tripp, S. V. Albers, and D. R. Mitchell, "Propulsive nanomachines: The convergent evolution of archaella, flagella and cilia," *Fems Microbiology Reviews*, vol. 44, no. 3, pp. 253–304, May 2020.

[128] E. Lauga, "Bacterial Hydrodynamics," *Annual Review of Fluid Mechanics*, vol. 48, no. 1, pp. 105–130, Jan. 2016.

[129] T. L. Jahn and J. J. Votta, "Locomotion of Protozoa," *Annual Review of Fluid Mechanics*, vol. 4, pp. 93–&, 1972.

[130] J. R. Blake and M. A. Sleigh, "Mechanics of ciliary locomotion," *Biological Reviews*, vol. 49, no. 1, pp. 85–125, Feb. 1974.

[131] J. R. Howse, R. A. L. Jones, A. J. Ryan, T. Gough, R. Vafabakhsh, and R. Golestanian, "Self-Motile Colloidal Particles: From Directed Propulsion to Random Walk," *Physical Review Letters*, vol. 99, no. 4, p. 048 102, Jul. 2007.

[132] E. Lauga and T. R. Powers, "The hydrodynamics of swimming microorganisms," *Reports On Progress In Physics*, vol. 72, no. 9, p. 096 601, Sep. 2009.

[133] J. J. Collins and I. N. Stewart, "Coupled nonlinear oscillators and the symmetries of animal gaits," *Journal of Nonlinear Science*, vol. 3, no. 1, pp. 349–392, Dec. 1993.

[134] H. Guo, Y. Man, K. Y. Wan, and E. Kanso, "Intracellular coupling modulates biflagellar synchrony," *Journal of The Royal Society Interface*, vol. 18, no. 174, p. 20 200 660, Jan. 2021.

[135] S. Sym and M. Kawachi, "Swimming behaviour in the genus pyramimonas," *Phycologia*, vol. 36, no. 4, pp. 110–110, Jul. 1997.

[136] H. Nozaki, O. Misumi, and T. Kuroiwa, "Phylogeny of the quadriflagellate Volvocales (Chlorophyceae) based on chloroplast multigene sequences," *Molecular Phylogenetics and Evolution*, vol. 29, no. 1, pp. 58–66, Oct. 2003.

[137] G. Gompper *et al.*, "The 2020 motile active matter roadmap," *Journal of Physics: Condensed Matter*, vol. 32, no. 19, p. 193 001, May 2020.

[138] M. A. R. Koehl, "Physical modelling in biomechanics," *Philosophical Transactions of the Royal Society B-biological Sciences*, vol. 358, no. 1437, pp. 1589–1596, Sep. 2003.

[139] B. J. H. Smith and J. R. Usherwood, "Minimalist analogue robot discovers animal-like walking gaits," *Bioinspiration & Biomimetics*, vol. 15, no. 2, p. 026 004, Feb. 2020.

[140] Y. Ozkan-Aydin, J. Rieser, C. Hubicki, S. W., and D. Goldman, "Physics approaches to natural locomotion: Every robot is an experiment," in *Robotic Systems and Autonomous Platforms*, ser. Woodhead Publishing in Materials, S. M. Walsh and M. S. Strano, Eds., Woodhead Publishing, 2019, pp. 109–127.

[141] S. Palagi *et al.*, "Structured light enables biomimetic swimming and versatile locomotion of photoresponsive soft microrobots," *Nature Materials*, vol. 15, no. 6, pp. 647–653, Jun. 2016.

[142] G. Z. Lum *et al.*, "Shape-programmable magnetic soft matter," *Proceedings of the National Academy of Sciences*, vol. 113, no. 41, E6007–E6015, Oct. 2016.

[143] H. Gu *et al.*, "Magnetic cilia carpets with programmable metachronal waves," *Nature Communications*, vol. 11, no. 1, p. 2637, Dec. 2020.

[144] K. Polotzek and B. M. Friedrich, "A three-sphere swimmer for flagellar synchronization," *New Journal of Physics*, vol. 15, no. 4, p. 045 005, Apr. 2013.

[145] A. Najafi and R. Golestanian, "Propulsion at low Reynolds number," *Journal of Physics: Condensed Matter*, vol. 17, no. 14, S1203–S1208, Apr. 2005.

[146] H.-W. Huang, F. E. Uslu, P. Katsamba, E. Lauga, M. S. Sakar, and B. J. Nelson, "Adaptive locomotion of artificial microswimmers," *Science Advances*, vol. 5, no. 1, eaau1532, Jan. 2019.

[147] T. Qiu *et al.*, "Swimming by reciprocal motion at low Reynolds number," *Nature Communications*, vol. 5, no. 1, p. 5119, Dec. 2014.

[148] Y. W. Kim and R. R. Netz, "Pumping Fluids with Periodically Beating Grafted Elastic Filaments," *Physical Review Letters*, p. 4, 2006.

[149] R. Vogel and H. Stark, "Motor-driven bacterial flagella and buckling instabilities," *The European Physical Journal E*, vol. 35, no. 2, p. 15, Feb. 2012.

[150] J. Elgeti and G. Gompper, "Emergence of metachronal waves in cilia arrays," *Proceedings of the National Academy of Sciences*, vol. 110, no. 12, pp. 4470–4475, Mar. 2013.

[151] K. M. Digumarti, A. T. Conn, and J. Rossiter, "EuMoBot: Replicating euglenoid movement in a soft robot," *Journal of The Royal Society Interface*, vol. 15, no. 148, p. 20 180 301, Nov. 2018.

[152] D. Owaki, T. Kano, K. Nagasawa, A. Tero, and A. Ishiguro, "Simple robot suggests physical interlimb communication is essential for quadruped walking," *Journal of The Royal Society Interface*, vol. 10, no. 78, p. 20 120 669, Jan. 2013.

[153] J. Tinevez *et al.*, "Trackmate: An open and extensible platform for single-particle tracking," *Methods*, vol. 115, pp. 80–90, 2017.

[154] W. Department of Agriculture and the Environment: Australian Antarctic Division, *Antarctic marine research aquarium*, [Online; accessed November 14, 2020], Oct. 2008.

[155] T. L. Hedrick, "Software techniques for two-and three-dimensional kinematic measurements of biological and biomimetic systems," *Bioinspiration & biomimetics*, vol. 3, no. 3, p. 034 001, 2008.

[156] C. A. Lembi, "Fine-structure of Flagellar Apparatus of Carteria," *Journal of Phycology*, vol. 11, no. 1, pp. 1–9, 1975.

[157] O. Moestrup and D. R. A. Hill, "Studies on the genus Pyramiinonas (Prasinophyceae) from Australian and European waters: P. propuisa sp. nov. and P. mitra sp. nov.," *Phycologia*, vol. 30, no. 6, p. 13, 1991.

[158] J. H. Belcher, "Further observations on the type species of Pyramimonas (P. tetrarhynchus Schmarda) (Prasinophyceae): An examination by light microscopy, together with

notes on its taxonomy," *Botanical Journal of the Linnean Society*, vol. 62, no. 2, pp. 241–253, Apr. 1969.

[159] B. R. Pearson and R. E. Norris, "Fine structure of cell division in Pyramimonas parkeae Norris and Pearson (Chlorophyta, Prasinophyceae)," *Journal of Phycology*, vol. 11, pp. 113–124, 1975.

[160] D. Cortese and K. Y. Wan, "Control of Helical Navigation by Three-Dimensional Flagellar Beating," *Physical Review Letters*, vol. 126, no. 8, p. 088 003, Feb. 2021.

[161] A. Shapere and F. Wilczek, "Geometry of self-propulsion at low Reynolds number," *Journal of Fluid Mechanics*, vol. 198, no. -1, p. 557, Jan. 1989.

[162] Y. Or, "Asymmetry and Stability of Shape Kinematics in Microswimmers' Motion," *Physical Review Letters*, vol. 108, no. 25, p. 258 101, Jun. 2012.

[163] R. L. Hatton, Y. Ding, H. Choset, and D. I. Goldman, "Geometric Visualization of Self-Propulsion in a Complex Medium," *Physical Review Letters*, vol. 110, no. 7, p. 078 101, Feb. 2013.

[164] H. J. Hoops, "Flagellar, cellular and organismal polarity in Volvox carteri," *Journal of Cell Science*, vol. 104, pp. 105–117, 1993.

[165] I. Spöring *et al.*, "Hook length of the bacterial flagellum is optimized for maximal stability of the flagellar bundle," *PLOS Biology*, vol. 16, no. 9, V. Sourjik, Ed., e2006989, Sep. 2018.

[166] G. Batchelor, *The life and legacy of G. I. Taylor*. Cambridge University Press, 1996.

[167] O. Croze and F. Peaudecerf, "G. I. Taylor and the physics of swimming," *Cavendish magazine*, 2016.

[168] R. M. Arco, J. R. Velez-Cordero, E. Lauga, and R. Zenit, "Viscous pumping inspired by flexible propulsion," *Bioinspiration & Biomimetics*, vol. 9, no. 3, p. 036 007, Sep. 2014.

[169] N. Gravish and G. V. Lauder, "Robotics-inspired biology," *Journal of Experimental Biology*, vol. 221, no. 7, 2018. eprint: https://jeb.biologists.org/content/221/7/jeb138438.full.pdf.

[170] A. Thawani and M. S. Tirumkudulu, "Trajectory of a model bacterium," *Journal of Fluid Mechanics*, vol. 835, pp. 252–270, Jan. 2018.

[171] M. J. Kim, M. M. J. Kim, J. C. Bird, J. Park, T. R. Powers, and K. S. Breuer, "Particle image velocimetry experiments on a macro-scale model for bacterial flagellar bundling," *Experiments In Fluids*, vol. 37, no. 6, pp. 782–788, Dec. 2004.

[172] T. S. Yu, E. Lauga, and A. E. Hosoi, "Experimental investigations of elastic tail propulsion at low Reynolds number," *Physics of Fluids*, vol. 18, no. 9, p. 091 701, Sep. 2006.

[173] R. Hayashi and D. Takagi, "Metachronal Swimming with Rigid Arms near Boundaries," *Fluids*, vol. 5, no. 1, p. 24, Feb. 2020.

[174] P. Holmes, R. J. Full, D. Koditschek, and J. Guckenheimer, "The dynamics of legged locomotion: Models, analyses, and challenges," *Siam Review*, vol. 48, no. 2, pp. 207–304, Jun. 2006.

[175] M. Hildebrand, "The Quadrupedal Gaits of Vertebrates," *Bioscience*, vol. 39, no. 11, pp. 766–775, Dec. 1989.

[176] N. J. Griffin and M. E. Aken, "Rhythmic Settling Behavior In Pyramimonas-parkeae (prasinophyceae)," *Journal of Phycology*, vol. 29, no. 1, pp. 9–15, Feb. 1993.

[177] S. Haroardottir, N. Lundholm, O. Moestrup, and T. G. Nielsen, "Description of Pyramimonas diskoicola sp. nov. and the importance of the flagellate Pyramimonas (Prasinophyceae) in Greenland sea ice during the winter-spring transition," *Polar Biology*, vol. 37, no. 10, pp. 1479–1494, Oct. 2014.

[178] F. Leliaert *et al.*, "Phylogeny and Molecular Evolution of the Green Algae," *Critical Reviews In Plant Sciences*, vol. 31, no. 1, pp. 1–46, 2012.

[179] G. I. Mcfadden, D. R. A. Hill, and R. Wetherbee, "A Study of the Genus Pyramimonas (prasinophyceae) From Southeastern Australia," *Nordic Journal of Botany*, vol. 6, no. 2, pp. 209–234, 1986.

[180] C. Brennen and H. Winet, "Fluid-mechanics of Propulsion By Cilia and Flagella," *Annual Review of Fluid Mechanics*, vol. 9, pp. 339–398, 1977.

[181] D. Tam and A. E. Hosoi, "Optimal feeding and swimming gaits of biflagellated organisms," *Proceedings of the National Academy of Sciences of the United States of America*, vol. 108, no. 3, pp. 1001–1006, Jan. 2011.

[182] C. Eloy and E. Lauga, "Kinematics of the Most Efficient Cilium," *Physical Review Letters*, vol. 109, no. 3, p. 038 101, Jul. 2012.

[183] K. Yasui, K. Sakai, D. Kano T.and Owaki, and A. Ishiguro, "Decentralized control scheme for myriapod robot inspired by adaptive and resilient centipede locomotion," *PloS one*, vol. 12, no. 2, e0171421, 2017.

[184] P. Holmes, R. Full, D. Koditschek, and J. Guckenheimer, "The dynamics of legged locomotion: Models, analyses, and challenges," *SIAM review*, vol. 48, no. 2, pp. 207–304, 2006.

[185] A. Biewener and S. Patek, *Animal locomotion*. Oxford University Press, 2018.

[186] J. Bush and D. Hu, "Walking on water: Biolocomotion at the interface," *Annual Review of Fluid Mechanics*, vol. 38, no. 1, pp. 339–369, 2006.

[187] D. Hu, J. Nirody, T. Scott, and M. Shelley, "The mechanics of slithering locomotion," *Proceedings of the National Academy of Sciences*, vol. 106, no. 25, pp. 10 081–10 085, 2009.

[188] K. Espenschied, H. Chiel, R. Quinn, and R. Beer, "Leg coordination mechanisms in the stick insect applied to hexapod robot locomotion," *Adaptive Behavior*, vol. 1, no. 4, pp. 455–468, 1993.

[189] P. Schiebel, M. Maisonneuve, K. Diaz, J. Rieser, and D. Goldman, "Robophysical modeling of bilaterally activated and soft limbless locomotors," in *Conference on Biomimetic and Biohybrid Systems*, Springer, 2020, pp. 300–311.

[190] A. Jusufi, D. Goldman, S. Revzen, and R. Full, "Active tails enhance arboreal acrobatics in geckos," *Proceedings of the National Academy of Sciences*, vol. 105, no. 11, pp. 4215–4219, 2008.

[191] T. L. Daniel and E. Meyhöfer, "Size limits in escape locomotion of carridean shrimp," *Journal of Experimental Biology*, vol. 143, no. 1, pp. 245–265, 1989.

[192] S. Sane, "The aerodynamics of insect flight," *Journal of experimental biology*, vol. 206, no. 23, pp. 4191–4208, 2003.

[193] E. Chang-Siu, T. Libby, and R. Tomizuka M.and Full, "A lizard-inspired active tail enables rapid maneuvers and dynamic stabilization in a terrestrial robot," in *2011 IEEE/RSJ International Conference on Intelligent Robots and Systems*, IEEE, 2011, pp. 1887–1894.

[194] E. Kim and Y. Youm, "Design and dynamic analysis of fish robot: Potuna," in *IEEE International Conference on Robotics and Automation, 2004. Proceedings. ICRA'04. 2004*, IEEE, vol. 5, 2004, pp. 4887–4892.

[195] K. Ma, P. Chirarattananon, S. Fuller, and R. Wood, "Controlled flight of a biologically inspired, insect-scale robot," *Science*, vol. 340, no. 6132, pp. 603–607, 2013.

[196] R. Full and M. Tu, "Mechanics of a rapid running insect: Two-, four-and six-legged locomotion," *Journal of Experimental Biology*, vol. 156, no. 1, pp. 215–231, 1991.

[197] C. Li, S. Hsieh, and D. Goldman, "Multi-functional foot use during running in the zebra-tailed lizard (callisaurus draconoides)," *Journal of Experimental Biology*, vol. 215, no. 18, pp. 3293–3308, 2012.

[198] S. Sponberg and R. Full, "Neuromechanical response of musculo-skeletal structures in cockroaches during rapid running on rough terrain," *Journal of Experimental Biology*, vol. 211, no. 3, pp. 433–446, 2008.

[199] B. Chong *et al.*, "Self propulsion via slipping: Frictional resistive force theory for multi-legged locomotors," *arXiv preprint arXiv:2207.10604*, 2022.

[200] S. Manton, "The evolution of arthropodan locomotory mechanisms. part 8. functional requirements and body design in chilopoda, together with a comparative account of their skeleto-muscular systems and an appendix on a comparison between burrowing forces of annelids and chilopods and its bearing upon the evolution of the arthropodan haemocoel," *Zoological Journal of the Linnean Society*, vol. 45, no. 306-07, pp. 251–484, 1965.

[201] G. Loeb, "Control implications of musculoskeletal mechanics," in *Proceedings of 17th international conference of the engineering in medicine and biology society*, IEEE, vol. 2, 1995, pp. 1393–1394.

[202] I. Brown and G. Loeb, "A reductionist approach to creating and using neuromusculoskeletal models," in *Biomechanics and neural control of posture and movement*, Springer, 2000, pp. 148–163.

[203] L. M. Roth and E. Willis, "Tarsal structure and climbing ability of cockroaches," *Journal of Experimental Zoology*, vol. 119, no. 3, pp. 483–517, 1952.

[204] W. Federle, E. Brainerd, T. McMahon, and B. Hölldobler, "Biomechanics of the movable pretarsal adhesive organ in ants and bees," *Proceedings of the National Academy of Sciences*, vol. 98, no. 11, pp. 6215–6220, 2001.

[205] W. Federle, M. Riehle, and R. Curtis A.S.G .and Full, "An integrative study of insect adhesion: Mechanics and wet adhesion of pretarsal pads in ants," *Integrative and Comparative Biology*, vol. 42, no. 6, pp. 1100–1106, 2002.

[206] S. Aoi, T. Tanaka, S. Fujiki, T. Funato, K. Senda, and K. Tsuchiya, "Advantage of straight walk instability in turning maneuver of multilegged locomotion: A robotics approach," *Scientific reports*, vol. 6, no. 1, pp. 1–10, 2016.

[207] K. Hoffman and R. Wood, "Turning gaits and optimal undulatory gaits for a modular centipede-inspired millirobot," in *2012 4th IEEE RAS & EMBS International Conference on Biomedical Robotics and Biomechatronics (BioRob)*, IEEE, 2012, pp. 1052–1059.

[208] Y. Ozkan-Aydin, B. Chong, E. Aydin, and D. Goldman, "A systematic approach to creating terrain-capable hybrid soft/hard myriapod robots," in *2020 3rd IEEE International Conference on Soft Robotics (RoboSoft)*, IEEE, 2020, pp. 156–163.

[209] D. Koh, J. Yang, and S. Kim, "Centipede robot for uneven terrain exploration: Design and experiment of the flexible biomimetic robot mechanism," in *2010 3rd IEEE RAS & EMBS International Conference on Biomedical Robotics and Biomechatronics*, IEEE, 2010, pp. 877–881.

[210] M. Masuda and K. Ito, "Semi-autonomous centipede-like robot with flexible legs," in *2014 IEEE International Symposium on Safety, Security, and Rescue Robotics (2014)*, IEEE, 2014, pp. 1–6.

[211] K. Hoffman and R. Wood, "Robustness of centipede-inspired millirobot locomotion to leg failures," in *2013 IEEE/RSJ International Conference on Intelligent Robots and Systems*, IEEE, 2013, pp. 1472–1479.

[212] S. Aoi, Y. Egi, and K. Tsuchiya, "Instability-based mechanism for body undulations in centipede locomotion," *Physical Review E*, vol. 87, no. 1, p. 012 717, 2013.

[213] K. Yasui *et al.*, "Decentralized control mechanism underlying interlimb coordination of centipedes," in *Proc. of the 8th International Symposium on Adaptive Motion of Animals and Machines (AMAM2017)*, 2017, pp. 83–84.

[214] B. Chong, J. He, D. Soto, T. Wang, D. Irvine, and D. Goldman, "A shannon-inspired framework for multi-legged matter transport," *In review*, 2022.

[215] D. Soto, K. Diaz, and D. Goldman, "Enhancing legged robot navigation of rough terrain via tail tapping," in *Climbing and Walking Robots Conference*, Springer, 2021, pp. 213–225.

[216] D. Soto, "Simplifying robotic locomotion by escaping traps via an active tail," Ph.D. dissertation, Georgia Institute of Technology, 2022.

[217] C. Sahley, "Behavior theory and invertebrate learning," in *The biology of learning*, Springer, 1984, pp. 181–196.

[218] F. Krasne and D. Glanzman, "What we can learn from invertebrate learning," *Annual review of psychology*, vol. 46, p. 585, 1995.

[219] R. Full and D. Koditschek, "Templates and anchors: Neuromechanical hypotheses of legged locomotion on land," *Journal of experimental biology*, vol. 202, no. 23, pp. 3325–3332, 1999.

[220] J. Mongeau, A. Demir, J. Lee, N. Cowan, and R. Full, "Locomotion-and mechanics-mediated tactile sensing: Antenna reconfiguration simplifies control during high-speed navigation in cockroaches," *Journal of Experimental Biology*, vol. 216, no. 24, pp. 4530–4541, 2013.

[221] D. Jindrich and R. Full, "Dynamic stabilization of rapid hexapedal locomotion," *Journal of Experimental Biology*, vol. 205, no. 18, pp. 2803–2823, 2002.

[222] A. Büschges, T. Akay, J. Gabriel, and J. Schmidt, "Organizing network action for locomotion: Insights from studying insect walking," *Brain research reviews*, vol. 57, no. 1, pp. 162–171, 2008.

[223] H. Cruse, V. Dürr, and J. Schmitz, "Insect walking is based on a decentralized architecture revealing a simple and robust controller," *Philosophical Transactions of the Royal Society A: Mathematical, Physical and Engineering Sciences*, vol. 365, no. 1850, pp. 221–250, 2007.

[224] R. Ritzmann and A. Büschges, "Adaptive motor behavior in insects," *Current opinion in neurobiology*, vol. 17, no. 6, pp. 629–636, 2007.

[225] T. Kubow and R. Full, "The role of the mechanical system in control: A hypothesis of self–stabilization in hexapedal runners," *Philosophical Transactions of the Royal Society of London. Series B: Biological Sciences*, vol. 354, no. 1385, pp. 849–861, 1999.

[226] D. Koditschek, R. Full, and M. Buehler, "Mechanical aspects of legged locomotion control," *Arthropod structure & development*, vol. 33, no. 3, pp. 251–272, 2004.

[227] H. Cruse, "What mechanisms coordinate leg movement in walking arthropods?" *Trends in neurosciences*, vol. 13, no. 1, pp. 15–21, 1990.

[228] M. Burrows, "Local circuits for the control of leg movements in an insect," *Trends in neurosciences*, vol. 15, no. 6, pp. 226–232, 1992.

[229] K. Yasui, T. Kano, E. Standen, H. Aonuma, A. Ijspeert, and A. Ishiguro, "Decoding the essential interplay between central and peripheral control in adaptive locomotion of amphibious centipedes," *Scientific reports*, vol. 9, no. 1, pp. 1–11, 2019.

[230] R. Pfeifer, M. Lungarella, and F. Iida, "Self-organization, embodiment, and biologically inspired robotics," *Science*, vol. 318, no. 5853, pp. 1088–1093, 2007.

[231] D. Hu, B. Chan, and J. Bush, "The hydrodynamics of water strider locomotion," *nature*, vol. 424, no. 6949, pp. 663–666, 2003.

[232] D. Hu and J. Bush, "Meniscus-climbing insects," *Nature*, vol. 437, no. 7059, pp. 733–736, 2005.

[233] R. Suter, O. Rosenberg, S. Loeb, H. Wildman, and J. Long, "Locomotion on the water surface: Propulsive mechanisms of the fisher spider," *The Journal of experimental biology*, vol. 200, no. 19, pp. 2523–2538, 1997.

[234] R. Suter, G. Stratton, and P. Miller, "Water surface locomotion by spiders: Distinct gaits in diverse families," *Journal of Arachnology*, pp. 428–432, 2003.

[235] R. Stratton G.E .and Suter and P. Miller, "Evolution of water surface locomotion by spiders: A comparative approach," *Biological Journal of the Linnean Society*, vol. 81, no. 1, pp. 63–78, 2004.

[236] C. Roh and M. Gharib, "Honeybees use their wings for water surface locomotion," *Proceedings of the National Academy of Sciences*, vol. 116, no. 49, pp. 24 446–24 451, 2019.

[237] J. Glasheen and T. McMahon, "A hydrodynamic model of locomotion in the basilisk lizard," *Nature*, vol. 380, no. 6572, pp. 340–342, 1996.

[238] S. Hsieh and G. Lauder, "Running on water: Three-dimensional force generation by basilisk lizards," *Proceedings of the National Academy of Sciences*, vol. 101, no. 48, pp. 16 784–16 788, 2004.

[239] X. Zhang, J. Yan, J. Zhao, G. Liu, H. Cai, and Q. Pan, "A miniature surface tension-driven robot mimicking the water-surface locomotion of water strider," in *2015 IEEE international conference on robotics and automation (ICRA)*, IEEE, 2015, pp. 3172–3177.

[240] Y. Chukewad, J. James, A. Singh, and S. Fuller, "Robofly: An insect-sized robot with simplified fabrication that is capable of flight, ground, and water surface locomotion," *IEEE Transactions on Robotics*, vol. 37, no. 6, pp. 2025–2040, 2021.

[241] M. Timm, S. Kang, J. Rothstein, and H. Masoud, "A remotely controlled marangoni surfer," *Bioinspiration & biomimetics*, vol. 16, no. 6, p. 066 014, 2021.

[242] J. Nirody *et al.*, "Geckos race across the water's surface using multiple mechanisms," *Current Biology*, vol. 28, no. 24, pp. 4046–4051, 2018.

[243] S. Asadzadeh, J. Walther, A. Andersen, and K.T., "Hydrodynamic interactions are key in thrust-generation of hairy flagella," *Physical Review Fluids*, vol. 7, no. 7, p. 073 101, 2022.

[244] F. Moisy, M. Rabaud, and K. Salsac, "A synthetic schlieren method for the measurement of the topography of a liquid interface," *Experiments in Fluids*, vol. 46, no. 6, pp. 1021–1036, 2009.

[245] B. Sutherland, S. Dalziel, G. Hughes, and P. Linden, "Visualization and measurement of internal waves by 'synthetic schlieren'. part 1. vertically oscillating cylinder," *Journal of fluid mechanics*, vol. 390, pp. 93–126, 1999.

[246] S. Wildeman, "Real-time quantitative schlieren imaging by fast fourier demodulation of a checkered backdrop," *Experiments in Fluids*, vol. 59, no. 6, pp. 1–13, 2018.

[247] D. Harris, "The pilot-wave dynamics of walking droplets in confinement," Ph.D. dissertation, Massachusetts Institute of Technology, 2015.

[248] A. Minelli and S. Golovatch, "Myriapods," in *Encyclopedia of Biodiversity: Second Edition*, 2013, pp. 421–432.

[249] B. Rodenborn, C. Chen, H. Swinney, B. Liu, and H. Zhang, "Propulsion of microorganisms by a helical flagellum," *Proceedings of the National Academy of Sciences*, vol. 110, no. 5, E338–E347, 2013.

[250] G. Whitham, *Linear and nonlinear waves*. John Wiley & Sons, 2011.

[251] K. Hinsch, "Three-dimensional particle velocimetry," *Measurement Science and Technology*, vol. 6, no. 6, p. 742, 1995.

VITA

Kelimar Diaz Cruz was born in April 26, 1995 in San Juan, Puerto Rico to Orlando Diaz Correa and Jackeline Cruz Baez. She grew up in Trujillo Alto, Puerto Rico, and obtained a Bachelor's of Science in Physics at the University of Puerto Rico-Rio Piedras Campus in 2017. She pursued graduate studies as a Quantitative Biosciences Ph.D. student at the Georgia Institute of Technology. She resides in Marietta, Georgia, and can often be found mentoring undergraduates, cuddling with her dog Tobi, or looking for something sweet.